A Two Element Interferometer Prototype for the Canadian Hydrogen Intensity Mapping Experiment

by

Gregory Davis

B.A.Sc. The University of British Columbia, 2009

A THESIS SUBMITTED IN PARTIAL FULFILLMENT OF
THE REQUIREMENTS FOR THE DEGREE OF

MASTER OF APPLIED SCIENCE

in

The Faculty of Graduate Studies

(Engineering Physics)

THE UNIVERSITY OF BRITISH COLUMBIA

(Vancouver)

May 2012

Abstract

The Canadian Hydrogen Intensity Mapping Experiment (CHIME) will measure the distribution of neutral hydrogen in the universe to constrain dark energy models. A two element radio interferometer operating between 425 and 850 MHz was built at the Dominion Radio Astrophysical Observatory as a CHIME technology prototype. The system temperature is approximately 80 K midband, of which almost 40 K is caused by feed loss and ground spill. A band defining filter used in the receiver allows the signal to be alias sampled at 850 MHz and unfolded to 425-850 MHz.

Delayed crosstalk between channels in the interferometer causes prominent spectral ripple with 3.8 MHz period in the cross correlations. Further baseline spectral ripple with 41 MHz period is caused by standing waves between the reflector and the feed ground plane.

Sky maps between declinations $52^\circ < \delta < 73^\circ$ over the full frequency band were made using a single dish. The accuracy of the maps is limited predominantly by gain fluctuation in the receiver caused by temperature, 1/f amplifier gain variation, and radio frequency interference. Principal component analysis is demonstrated as a foreground removal technique.

Table of Contents

List of Tables

List of Figures

Acknowledgements

I would like to thank Mark Halpern and Gary Hinshaw for their support, encouragement, sound advice, and excellent problem solving. I am very appreciative of the guiding influence Tom Landecker has provided throughout the project. I would also like to thank Mandana Amiri and Don Wiebe for their daily help and patience in the lab. I am grateful for all the support I have received from the whole CHIME team; in particular, Jeff Peterson, Kevin Bandura, Kris Sigurdson, and Ivan Padilla. I also want to thank the many people at DRAO without whom this thesis would not have been possible.

Chapter 1

Introduction

The Canadian Hydrogen Intensity Mapping Experiment (CHIME) is a proposed radio telescope intended to probe the nature of dark energy[1]. CHIME will measure the distribution of neutral hydrogen in the universe by observing the 21 cm hyperfine transition line in the redshift range $0.8 < z < 2.5$.

1.1 Dark Energy

Dark energy is the name given to the antigravity-like agent that accelerates the expansion of the universe [1, 2]. Recent measurements of the cosmic microwave background (CMB) suggest that the total mass-energy of the universe is comprised of 4.6% baryonic matter, 22.7% dark matter, and 72.8% dark energy [3]. Dark energy could be explained by a cosmological constant Λ, which prescribes a constant energy density everywhere, or by a scalar field that changes in time and space.

The dark energy equation of state is

$$w(a) = \frac{P_\Lambda}{\rho_\Lambda} = w_0 + (1 - a)w_a \tag{1.1}$$

[1] `http://phas.ubc.ca/chime`

where P_Λ is the pressure; ρ_Λ is the energy density; a is the scale factor, related to redshift by $a = 1/(1+z)$; and w_0 and w_a are the dark energy cosmological parameters. The cosmological constant model requires $w = -1$ everywhere; however, other models permit w to evolve as a function of redshift [4].

1.2 Baryon Acoustic Oscillations

In the early universe, protons and electrons existed in a hot, dense plasma. Quantum mechanical fluctuations in the primordial plasma caused the development of overdense regions consisting of baryons, dark matter, and photons. Compton scattering of photons colliding with the charged particles effectively coupled light and matter. The heat generated by scattering in high density regions created outward pressure on the baryonic matter, leading to spherical pressure waves, or cosmic sound; these waves are called baryon acoustic oscillations (BAO) [5].

As the universe expanded and cooled below 3000 K, protons and electrons recombined to form atoms. After recombination, photons were no longer coupled to matter by Compton scattering, and the escape of the photons relieved the outward pressure on the baryons around the high density regions. The escaping photons are the CMB, at redshift $z \approx 1100$.

At a single high density region immediately after recombination, a centre consisting of dark matter, which interacts only gravitationally, is surrounded by a spherical shell of baryonic matter, which propagated outward with the photons prior to recombination. The radial distance between the centre and

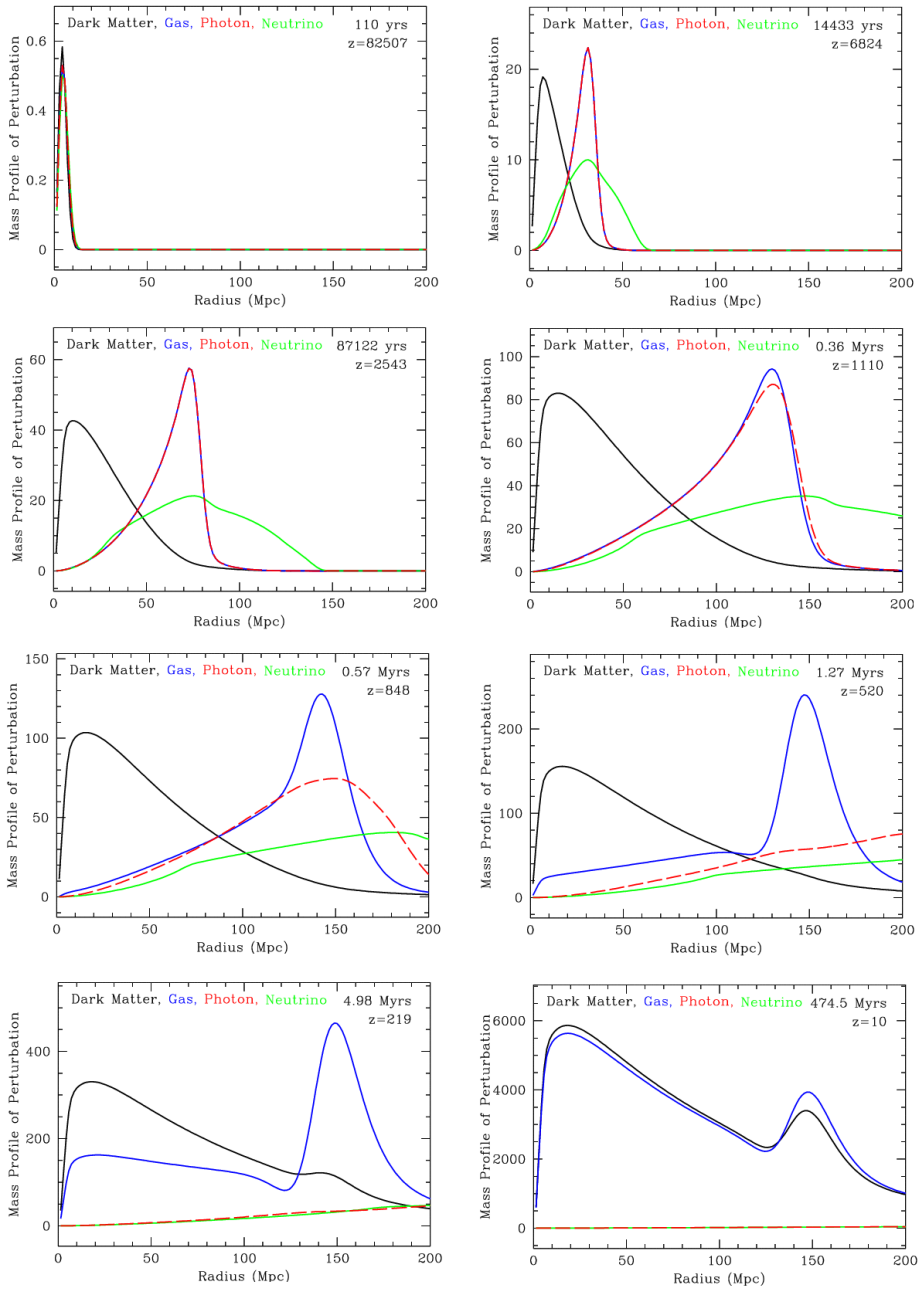

Figure 1.1: Immediately after inflation begins, the baryon gas and photons travel together away from the dark matter. At $z \approx 1100$, recombination occurs and the photons escape. At later times, the baryons and dark matter collapse toward each other gravitationally, but a density enhancement at the sound horizon remains. Plots by D. Eisenstein.

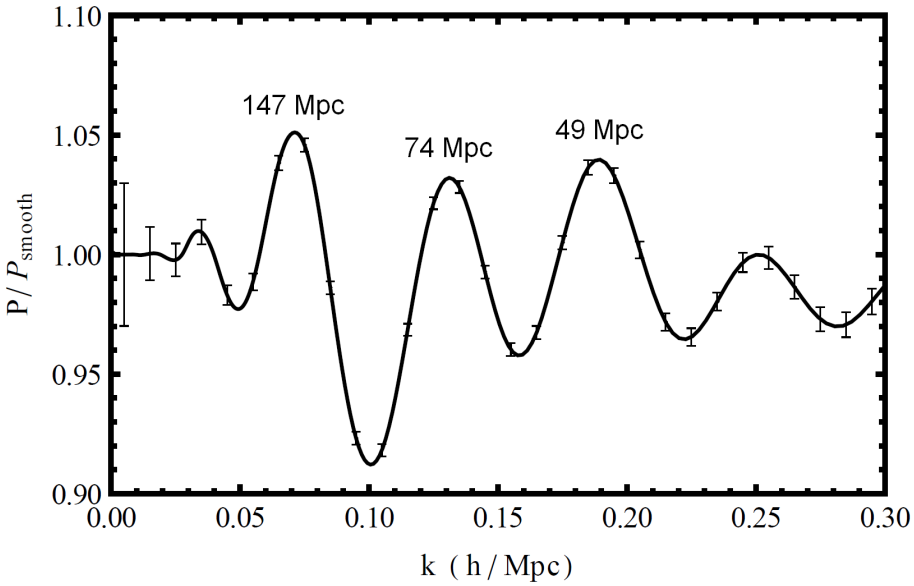

Figure 1.2: The ratio of the matter power spectrum with baryon acoustic oscillations to the power spectrum without baryon acoustic oscillations. The angular and frequency resolution of CHIME are set to detect the density enhancements at the 147 Mpc sound horizon and its second and third harmonics at 74 and 49 Mpc. Higher peaks are partially washed out by gravitational interactions. Error bars for a CHIME two year survey at a single effective redshift for a system temperature of 50 K are shown. Calculation and plot by Kris Sigurdson and Mike Sitwell.

the shell is the sound horizon. As cosmic sound waves propagated from high density origins, waves originating from different high density fluctuations interfered. The BAO remain statistically detectable by measuring the two point correlation function across the sky: matter is more likely to be found separated by the sound horizon and its harmonics than other lengths.

Precise measurements of the CMB have quantified the sound horizon as 147 Mpc [6]. This enables the use of the BAO as a standard ruler. Measuring the apparent angular size of the BAO at different redshifts provides a method

of tracking the expansion history of the universe. In particular, observing the evolution of the standard ruler between redshifts $0.8 < z < 2.5$ targets the time when dark energy became dominant and the expansion of the universe began to accelerate.

Mapping the distribution of neutral hydrogen through the use of the 21 cm hyperfine spin flip transition is a method of measuring the evolution of the BAO standard ruler. Previous charting of the late expansion history of the universe involved observation of many individual galaxies, and determination of the redshift of each. Neutral hydrogen intensity mapping can measure the collective emission of many galaxies simultaneously and provide similar information as individual galactic measurements with less required sensitivity and resolution [7–9]. Because 21 cm emission is the dominant spectral line below 1420 MHz, redshift corresponds directly to observed frequency [10]. Intensity mapping also enables the mapping of a much larger volume of the observable universe than optical galaxy surveys.

Together with knowledge of the early universe obtained through CMB measurements, and the recent universe obtained through optical galaxy surveys, CHIME will constrain the dark energy parameters w_0 and w_a [7, 11].

1.3 CHIME Instrument

CHIME will consist of an array of five 100 m $\times$ 20 m cylindrical parabolic reflectors instrumented with more than 2500 feeds. The telescope will be built at the Dominion Radio Astrophysical Observatory (DRAO) near Penticton, BC. CHIME will employ a drift scan strategy, surveying the northern

half of the sky each day as the earth rotates. Digital beam forming facilitates surveillance of the available sky with stationary reflectors.

In order to learn about the expansion history of the universe during the transition from matter dominated to dark energy dominated regimes, redshifts both above and below $z \approx 1$ ($f = 710$ MHz) are required. The upper edge of the operating frequency range of CHIME is practically limited by interference caused by the cell phone band beginning slightly above 800 MHz ($z \approx 0.8$). Observing at higher redshifts yields diminishing scientific impact as measured by the Dark Energy Task Force (DETF) Figure of Merit (FoM) [12]. The lower frequency is chosen to give an upper redshift limit of approximately $z = 2.5$, corresponding to $f = 406$ MHz. Figure 1.3 shows the relative improvement in the DETF FoM provided by CHIME for different redshift ranges over other near term experiments.

The angular resolution of the telescope sets the minimum detectable feature size. A 100 m^2 aperture allows objects roughly 10 Mpc across to be resolved at $z = 1$, which is more than sufficient for resolving the third peak of the BAO, as seen in Figure 1.2 [7]. The third dimension of hydrogen intensity mapping, distance, is obtained by observing different redshifts. To achieve spatial resolution matching the other dimensions, frequency resolution of 2 to 5 MHz is required for $0.8 < z < 2.5$. Table 1.1 shows the angular resolution of CHIME and the frequency resolution required to match it.

Room temperature receivers will populate each polarization of the dual linearly polarized feeds along the focal length of each reflector. A digital correlator will perform Fourier transform imaging, allowing a 90° north-south field of view while maintaining high angular resolution. The correlator is

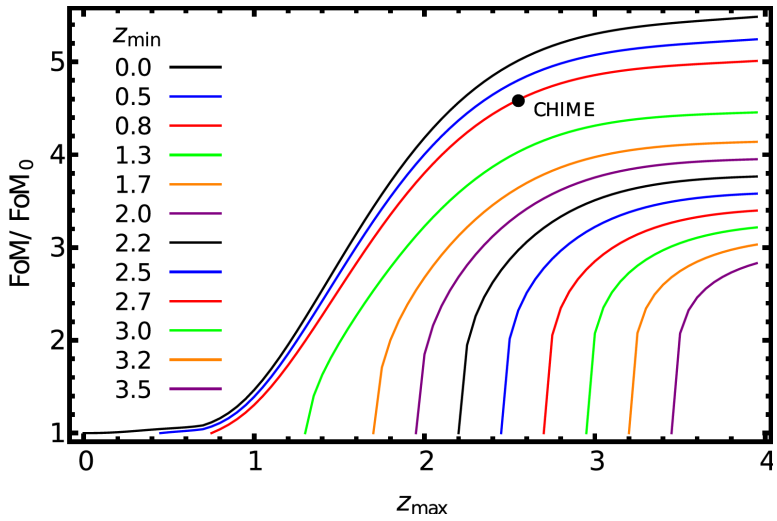

Figure 1.3: The relative improvement in the DETF FoM provided by CHIME over other near term experiments (Planck + DETF Stage II + BOSS) as a function of redshift range. Calculation and plot by Kris Sigurdson and Mike Sitwell.

z	fobs (MHz)	co-moving distance (Mpc)	Δz	Δf (MHz)
0.8	789	12.95	0.0046	2.02
1	710	17.10	0.0069	2.44
2	473	40.56	0.027	4.25
2.5	406	53.35	0.044	5.09

Table 1.1: CHIME spatial resolution.

made up of a digitizer and FPGA signal processing system to channelize the received signals by frequency and form the beams. Each beam formed frequency is routed to a computer to calculate correlations across the cylinders.

The CHIME experiment design parameters are shown in Table 1.2. A block diagram of the anticipated signal path is shown in Figure 1.4. One of the key parameters is the system temperature T_{sys} (Section 3.4). The 21 cm cosmological signal is only about 150 μK at the highest angular resolution of CHIME [7]. The noise per sky pixel due to the system temperature is given by:

$$\Delta T = \frac{T_{sys}}{\sqrt{\Delta f \; t_{int}}} \tag{1.2}$$

For a 1 MHz channel bandwidth Δf, and 50 K system temperature, the integration time t_{int} required at each pixel to reduce the noise to the level of the cosmic signal of 150 μK is about 31 hours. For a 0.26 square degree beam surveying the northern half of the sky, this corresponds to approximately 114 years of observing time per pixel for a single receiver. With 2580 single polarization feeds, this time reduces to approximately two years. The required observing time is proportional to the square of the system temperature, so T_{sys} is a critical parameter.

1.3.1 CHIME Prototype

To facilitate prototyping, characterize the site, and establish a working relationship between DRAO and the CHIME team, a prototype radio telescope was built at DRAO. The system is a two element interferometer made up of

Frequency Wavelength Redshift	800-400 MHz 0.37-0.75 m 0.8-2.5
System Temperature	$\leq$ 50 K
Beam Size N-S Field of View	0.26°-0.52° 90°
Cylinder Size Number of Cylinders Collecting Area f/d	100 m $\times$ 20 m 5 10,000 m^2 0.25
Dual-polarization antenna spacing Number of antennas per cylinder Channel Bandwidth	0.31 m 256 1 MHz

Table 1.2: CHIME experiment design parameters.

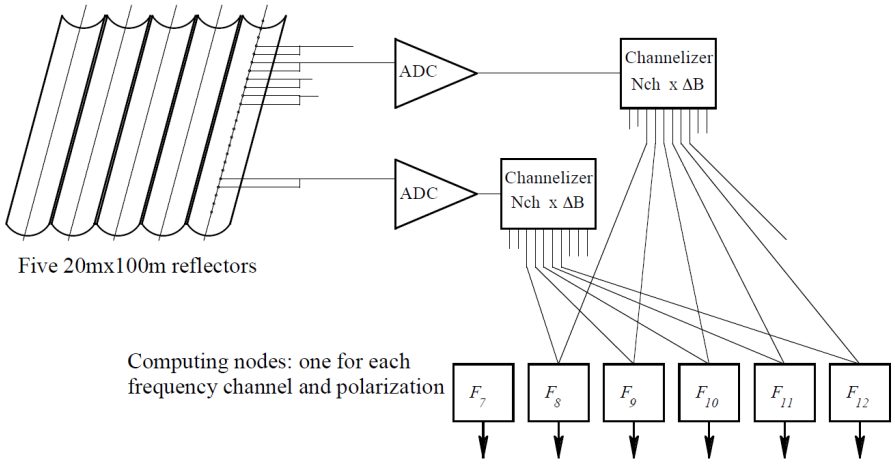

Figure 1.4: The CHIME signal path.

two circular 8.53 m parabolic dishes spaced 19 m apart on an east-west line, instrumented with a prototype receiver and correlator. This prototype telescope is an ideal technology test bed, and provides an excellent opportunity to begin work on CHIME.

The design, construction, characterization and data analysis of the two dish system constitute the work of this thesis.

Chapter 2

Two Dish System

A two element radio interferometer comprised of two circular parabolic reflectors was constructed as a CHIME prototype and technology testbed at DRAO. The two dish system is instrumented with amplifiers and feeds operating from 425 MHz to 850 MHz in orthogonal linear polarizations, and uses a Reconfigurable Open Architecture Computing Hardware (ROACH) correlator and analog to digital converters (ADC) developed by the Collaboration for Astronomy Signal Processing and Electronics Research[2] (CASPER).

An overview of the two dish system is presented in Section 2.1, followed by a background in microwave amplifier design in Section 2.2. The analog receiver, including the amplifiers and feed, are described in Sections 2.3, 2.4 and 2.5, and a brief outline of the back end ADC and correlator is provided in Section 2.6.

2.1 Overview

2.1.1 Site

DRAO is a national research facility about 25 km south of Penticton, BC, at coordinates 49.3° N, 119.6° W. The observatory is surrounded by mountains,

[2] `http://casper.berkeley.edu`

Figure 2.1: The Dominion Radio Astrophysical Observatory.

well protected from urban sources of radio frequency interference (RFI). Most of the surrounding area within sight is owned by the observatory, and the region is regulated by the federal government to ensure a clean RF environment. The observatory is home to other active radio telescopes and has a full staff of physicists, engineers and technicians specializing in radio astronomy. The facility is careful to properly shield all electronic equipment, and closely monitors on site interference.

2.1.2 Antennas

The interferometer is made up of two circular parabolic reflectors on an east-west line spaced 19 m apart. The reflectors are spares for the DRAO Synthesis Telescope, a seven element interferometer operating at 1420 MHz and 408 MHz. They have a diameter of 8.53 m, a focal length f=3.66 m ($f/d = 0.43$), and a fine mesh spacing which passes ground leakage of less

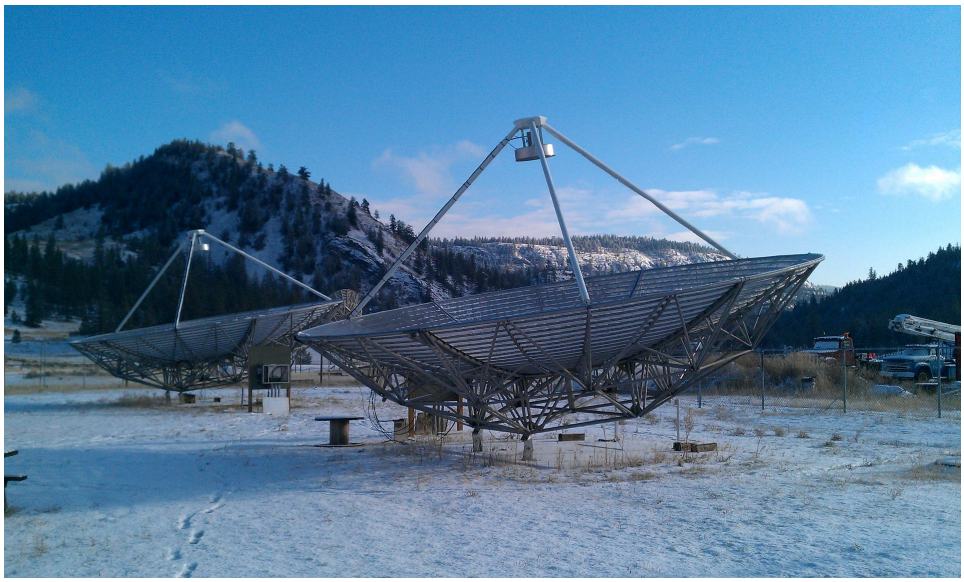

Figure 2.2: The two dish system.

than 6 K at 1.4 GHz [13]. The reflectors are mounted on hinges, allowing them to be tilted from zenith to approximately 25° north of zenith, or declination $49° \leq \delta \leq 74°$.

At the focus of each dish, the feed is connected below a ground plane. The ground plane hangs below a support structure held in place by three struts fixed to the rim of the dish. Initially, the ground plane was a simple circular disk of diameter 66 cm, as seen in Figure 2.3a. To reduce the beam spill over the edge of the dish (Section 3.4.3), the main lobe of the feed radiation pattern (without the reflector) was narrowed by adding a cylinder around the edge of the ground plane, as seen in Figure 2.3b. The cylinder extends 18 cm below the ground plane.

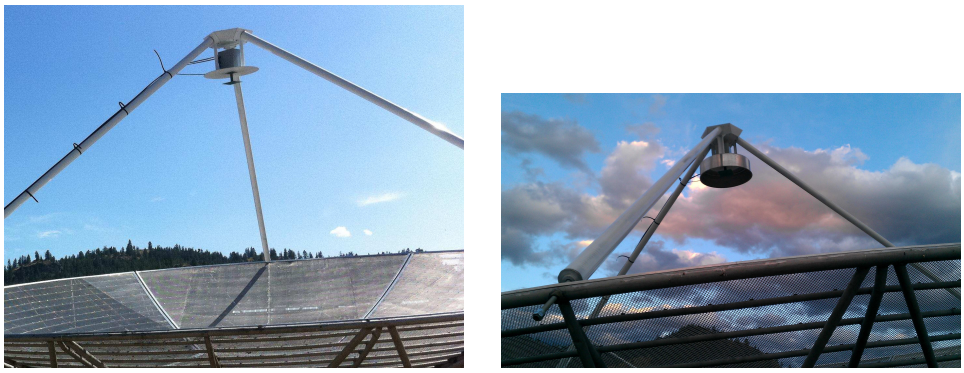

(a) Without isolating cylinder (b) With isolating cylinder

Figure 2.3: Ground plane configurations at the focus.

2.1.3 Electronics

Analog Receiver

Above the ground plane, each linear polarization of the feed connects directly to a low noise amplifier (LNA) through an SMA connector. Each LNA is electrically shielded in a dedicated aluminum box. The output of the LNA connects to a second stage combined amplifier and filter, electrically sealed in a separate aluminum shielding box. The output of the second amplifier connects to a coaxial 6 dB attenuator, which connects to a 50 m coaxial cable to transmit the signal from the focus to the digitizer. The cable is strapped to one of the three struts supporting the structure at the focus, and travels underground to a trailer containing the back end electronics.

Inside the trailer, the signal exits the 50 m cable and passes through a second coaxial 6 dB attenuator, and is amplified further by a second combined amplifier and filter box. The output of the last amplifier is connected to the input of a large shielding box containing the ROACH ADC and corre-

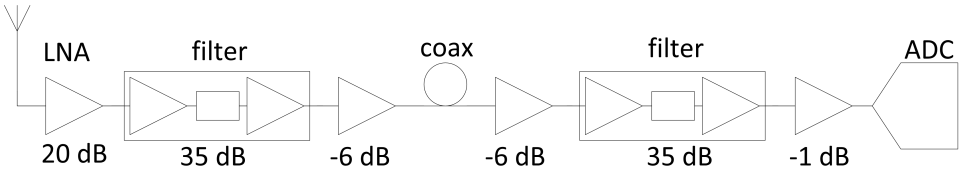

Figure 2.4: Two dish system receiver block diagram.

lator, and the data collection computer. Inside the shielding box, the signal is connected to the ADC board through a 1 dB attenuator. A block diagram of the overall system is shown in Figure 2.4.

The amplifiers inside the trailer are directly powered by a 5 V supply. The ground of the amplifiers in the trailer and the amplifiers at the focus is connected through the shielding of the 50 m coaxial cable. The power for the amplifiers at the focus is provided by supplies at the base of each dish. At the focus, linear regulators drop the voltage to 5 V. The ground of the amplifiers is connected directly to the ground plane of the feed, which is electrically connected to the dish structure.

Housekeeping Circuitry

The temperature and regulated voltage of the amplifiers at the focus and in the trailer are monitored by a data collection system separate from the correlator. At the focus of each dish and inside the trailer, a low speed purely analog voltage to current converter transmits a signal to the correlator shielding box. Inside the shielding box, a current to voltage converter conditions the signal for an ADC on board an Atmel XMEGA-128 development board. Approximately once per second, the readings are sent to the

data collection computer over a serial interface and saved.

ADC and Correlator

The ROACH correlator and ADC are clocked using a commercial signal generator. The frequency response of the analog receiver chain is shaped by a band defining filter that passes frequencies between approximately 400 and 800 MHz. This allows the signal to be directly sampled at 850 MHz, and unfolded from 0-425 MHz to 425-850 MHz spectrum with minimal contamination from out of band signals. This aliased sampling strategy permits the use of a relatively modest ADC clock rate of 850 MHz.

The CASPER based back end consists of two input ADC boards, each with a dual channel 8 bit AT84AD001B ADC that can collect up to 1 GS/s. The four independent digitized signals are processed by the ROACH correlator using an FX architecture: the incoming signals are Fourier transformed, then cross correlated. The correlator accumulates the correlation products it calculates, and the data collection computer reads the results and writes them to disk.

2.2 Microwave Amplifier Background

Designing a microwave amplifier involves selecting input and output matching networks specifically for a given transistor, input and output impedances, and desired performance. This amounts to selecting the source and load reflection coefficients Γ_s and Γ_L to achieve appropriate trade-offs between different performance parameters, and designing matching networks to pro-

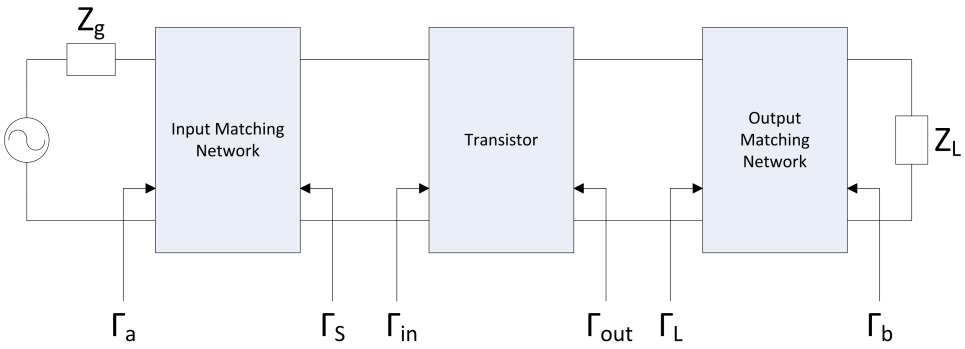

Figure 2.5: Block diagram of a basic microwave amplifier structure, showing the reflection coefficients Γ looking into different places in the circuit.

duce these reflection coefficients. A block diagram of a basic microwave amplifier is shown in Figure 2.5.

2.2.1 Noise

Noise Temperature and Noise Figure

A resistor R at temperature T generates thermal noise according to Planck's black body radiation law

$$v = \sqrt{\frac{4hfR\ \Delta f}{e^{\frac{hf}{kT}} - 1}} \tag{2.1}$$

where v represents the standard deviation of the voltage fluctuations in the resistor, h is Planck's constant, k is Boltzmann's constant, Δf is the bandwidth, and f is the centre frequency [14]. Equation 2.1 can be simplified at microwave frequencies where $hf \ll kT$ by Taylor expanding the exponential in the denominator to first order. Converting the resulting expression from

voltage to power leads to the Johnson-Nyquist equation for thermal noise:

$$P = kT\Delta f \tag{2.2}$$

The noise of any device can be represented by an equivalent noise temperature T_e, where T_e is the physical temperature of a resistor required to produce the same noise power as the noisy device in a specified bandwidth.

Another standard method of describing the noise of a two port device is noise factor. Noise factor, F, quantifies the signal to noise ratio degradation experienced by a signal with an input reference noise temperature of 290 K passing through a noisy device. Noise figure, NF, is the same quantity expressed in decibels [14]:

$$F = \frac{SNR_{in}}{SNR_{out}} = \frac{\text{total output noise power}}{\text{output noise power due to input noise}} \tag{2.3}$$

$$NF = 10\log_{10} F \tag{2.4}$$

When cascading noisy devices, the overall noise temperature T_{total} is

$$T_{total} = T_1 + \frac{T_2}{G_1} + \frac{T_3}{G_1 G_2} + \cdots \tag{2.5}$$

where T_1 is the noise temperature of the first device, G_1 is the gain of the first device, T_2 is the noise temperature of the second device, G_2 is the gain of the second device, etc [15]. In a typical receiver with substantial gain in the early stages, the first stage noise dominates the overall noise.

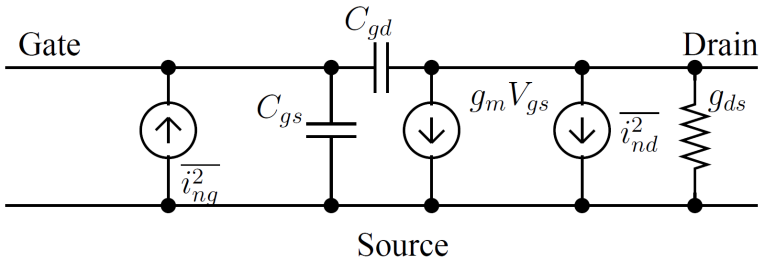

Figure 2.6: A FET model showing the small signal parameters and noise currents [19].

Noise in FETs

A simple noise model of a field effect transistor (FET) is shown in Figure 2.6. The drain current noise i_{nd} arises from thermal noise associated with the channel resistance of the transistor [16–18]. Because it is thermal in nature, the drain noise current is spectrally flat (white) with Gaussian amplitude; therefore, it can be characterized statistically by its variance

$$\overline{i_{nd}^2} = 4kT\gamma g_{d0}\Delta f \tag{2.6}$$

where k is the Boltzmann constant, T is the temperature of the transistor, Δf is the bandwidth, and g_{d0} is the channel transconductance with zero voltage across the drain source. For long channel transistors operating in the saturation region, the drain noise coefficient γ is approximately 2/3, while in the triode region γ is close to 1 [16, 17].

Fluctuating charges in the transistor channel create noise that capacitively couples to the gate, giving rise to gate current noise i_{ng}, also charac-

terized by its variance

$$\overline{i_{ng}^2} = 4kT\delta g_g \Delta f \tag{2.7}$$

where g_g is the gate conductance

$$g_g = \frac{\omega^2 C_{gs}^2}{5 g_{d0}} \tag{2.8}$$

The gate noise coefficient δ is approximately 4/3 in long channel devices [17]. The gate current noise increases with frequency due to the frequency dependence of the gate conductance. Both γ and δ are higher for short channel devices; this is not yet well understood, but often attributed to hot carrier effects or substrate noise [16, 20].

In addition to thermal noise in the transistor channel, FETs exhibit 1/f noise and shot noise. 1/f drain noise current in FETs is characterized by

$$\overline{i_n^2} = \frac{K}{f} \frac{g_m^2}{WLC_{ox}^2} \Delta f \tag{2.9}$$

where W and L are the transistor width and length, g_m is the transconductance, C_{ox} is the gate capacitance per unit area, and K is a transistor dependent parameter on the order of 10^{-25} V^2F [21]. At microwave frequencies, 1/f noise can be ignored.

Shot noise occurs any time discrete charge carriers must jump over a potential barrier. Shot noise current is characterized by

$$\overline{i_n^2} = 2qI_{DC}\Delta f \tag{2.10}$$

where q is the elementary charge 1.6×10^{-19} C and I_{DC} is the DC current in Amperes [22]. The DC gate leakage current is a source of shot noise, but this current is normally small enough that its associated shot noise can be neglected [16].

Noise in Two Port Networks

The gate and drain noise currents in a FET are partially correlated due to their common underlying physical cause; ie, thermal fluctuations in the transistor channel. Because of this correlation, an optimal source impedance can be chosen which minimizes the overall degradation of signal to noise ratio caused by the transistor. A brief review of the classical two port noise model which leads to this result is presented [16, 23, 24].

All noise sources in a transistor (gate current noise, drain current noise, thermal noise in resistive lead materials, etc) can be reflected to the input of a two port network representing the noiseless transistor, and converted to a series voltage noise e_n and a shunt current noise i_n [25]. The network is connected to a source that has noise i_s and admittance Y_s, as shown in Figure 2.7.

To account for correlation between e_n and i_n, the noise source i_n is broken into two components: an uncorrelated part i_u and a correlated part i_c. The correlated part i_c is related to the voltage noise e_n by a proportionality constant: the correlation admittance Y_c. The total noise can be expressed as

$$\overline{i_{n,total}^2} \;=\; \overline{|i_u + (Y_c + Y_s)e_n|^2} \;=\; \overline{i_u^2} + |Y_c + Y_s|^2\,\overline{e_n^2} \qquad (2.11)$$

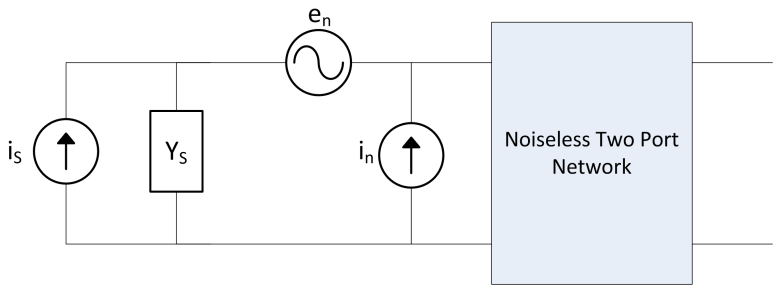

Figure 2.7: A two port noise model connected to a source i_s of admittance Y_s. All internal noise sources have been grouped into e_n and i_n.

Expressed in terms of noise factor, the two port noise of the network in Figure 2.7 is given by

$$F = \frac{\overline{i_s^2} + \overline{i_{n,total}^2}}{\overline{i_s^2}} \tag{2.12}$$

The noise sources e_n, i_u and i_s are rewritten as thermal noise sources arising from a resistance R_n and conductances G_u and G_s, and the source and correlated admittances are split into their real (G) and imaginary (B) parts. The noise factor F using this notation is:

$$F = 1 + \frac{G_u + [(G_c + G_s)^2 + (B_c + B_s)^2]R_n}{G_s} \tag{2.13}$$

The optimum source admittance Y_{opt} that yields the best noise performance is found by minimizing Equation 2.13 with respect to the source admittance:

$$Y_{opt} = G_{opt} + jB_{opt} \tag{2.14a}$$

$$B_{opt} = -B_c \tag{2.14b}$$

$$G_{opt} = \sqrt{\frac{G_u}{R_n} + G_c^2} \tag{2.14c}$$

The minimum noise factor F_{min} is found by substituting Y_{opt} into Equation 2.13, yielding

$$F_{min} = 1 + 2R_n(G_{opt} + G_c) \tag{2.15}$$

The final noise factor of the two port network can be expressed in terms of the optimal source admittance and the minimum noise figure:

$$F = F_{min} + \frac{R_n}{G_s} |Y_s - Y_{opt}|^2 \tag{2.16a}$$

$$F = F_{min} + \frac{R_n}{G_s}[(G_s - G_{opt})^2 + (B_s - B_{opt})^2] \tag{2.16b}$$

The relationship between source admittance and reflection coefficient is:

$$Y_s = \frac{1 - \Gamma_{opt}}{1 + \Gamma_{opt}} \tag{2.17}$$

Equation 2.16 shows that contours of constant noise figure are circles in the source admittance plane with radius inversely proportional to $\sqrt{R_n}$. Practically, this means that the noise of transistors with larger R_n are more sensitive to changes in source admittance away from the optimal value.

Numerous works in the literature present detailed modelling techniques intended to calculate the value of the gate and drain noise and the correlation

coefficient between them. This ultimately leads to the extraction of the noise parameters R_n, G_c, B_c and G_u in terms of transistor geometry and technology parameters. For example, [25–28].

2.2.2 Stability

Stability is crucial for any amplifier. The circuit in Figure 2.5 is stable if [24]:

$$|\Gamma_s| < 1 \tag{2.18a}$$

$$|\Gamma_L| < 1 \tag{2.18b}$$

$$|\Gamma_{in}| = \left| S_{11} + \frac{S_{12}S_{21}\Gamma_L}{1 - S_{22}\Gamma_L} \right| < 1 \tag{2.18c}$$

$$|\Gamma_{out}| = \left| S_{22} + \frac{S_{12}S_{21}\Gamma_s}{1 - S_{11}\Gamma_s} \right| < 1 \tag{2.18d}$$

The reflection coefficients Γ_{in}, Γ_{out}, Γ_s and Γ_L are calculated using the same characteristic impedance Z_0, and they depend on frequency, DC bias, and the source and load terminations Z_g and Z_L. If an amplifier is stable for any passive termination impedances Z_g and Z_L, it is unconditionally stable. Conversely, if it is stable only for a particular range of source and load impedances, it is conditionally stable, or potentially unstable.

For an amplifier to perform as intended, it should be stable at all frequencies, not only in the band of interest. Out of band oscillations can severely alter the in band performance of an amplifier.

The stability of a network can be predicted using its S parameters. One test for unconditional stability uses the Rollett stability factor K [29] and

an additional parameter Δ. An amplifier is unconditionally stable at a given frequency if it satisfies the criteria [14]:

$$K > 1 \tag{2.19a}$$

$$|\Delta| < 1 \tag{2.19b}$$

where

$$\Delta = S_{11}S_{22} - S_{12}S_{21} \tag{2.20}$$

and

$$K = \frac{1 - |S_{11}|^2 - |S_{22}|^2 + |\Delta|^2}{2|S_{12}S_{21}|} \tag{2.21}$$

Another test for unconditional stability uses only a single parameter, μ [30]:

$$\mu = \frac{1 - |S_{11}|^2}{|S_{22} - \Delta S_{11}^*| + |S_{12}S_{21}|} > 1 \tag{2.22}$$

A single stability figure of merit is useful because it allows a direct comparison between designs.

If oscillations appear in a design, there are three basic solutions. The first is the addition of series feedback, as described in Section 2.2.5. Inductive series feedback can improve in band stability, although it may have negative out of band effects [31].

The second is resistive loading. Four kinds of resistive loading can be added: series at the input, shunt at the input, series at the output, and shunt at the output. Adding resistance on the input side causes loss to the signal, reducing the gain and increasing the noise figure; thus, output loading is

preferred for low noise designs. Resistive loading also alters the matching.

The third way to improve stability is to add negative feedback by adding resistance between the gate and drain. This tends to improve the input and output matching, and broadens the frequency response of the amplifier. Like resistive loading, the addition of drain gate negative feedback comes at the expense of some noise figure and gain.

2.2.3 Gain

The overall power gain of a microwave amplifier depends on the source and load termination impedances Z_g and Z_L. To allow gain measurements partially independent of the source and load, three gains are defined: transducer gain G_T (includes input and output matching), operating gain G_p (includes output matching), and available gain G_A (includes input matching). They are defined as [14]:

$$G_T = \frac{\text{power delivered to load}}{\text{power available from source}} \tag{2.23a}$$

$$G_T = \frac{1-|\Gamma_s|^2}{1-\Gamma_{in}\Gamma_s}\,|S_{21}|^2\,\frac{1-|\Gamma_L|^2}{|1-S_{22}\Gamma_L|^2} \tag{2.23b}$$

$$G_T = \frac{1-|\Gamma_s|^2}{1-S_{11}\Gamma_s}\,|S_{21}|^2\,\frac{1-|\Gamma_L|^2}{|1-\Gamma_{out}\Gamma_L|^2} \tag{2.23c}$$

$$G_p = \frac{\text{power delivered to load}}{\text{power delivered to network}} \tag{2.24a}$$

$$G_p = \frac{1}{1-|\Gamma_{in}|^2}\,|S_{21}|^2\,\frac{1-|\Gamma_L|^2}{|1-\Gamma_{out}\Gamma_L|^2} \tag{2.24b}$$

$$G_A = \frac{\text{power available from network}}{\text{power available from source}} \tag{2.25a}$$

$$G_A = \frac{1-|\Gamma_s|^2}{|1-S_{11}\Gamma_s|^2}\ |S_{21}|^2\ \frac{1}{1-|\Gamma_{out}|^2} \tag{2.25b}$$

The transducer gain is the most useful, but when designing amplifiers the available and operating gains can be helpful.

2.2.4 Return Loss

The amount of power delivered from the source to the amplifier and from the amplifier to the load can be characterized using return loss or voltage standing wave ratio. Referring to Figure 2.5, the input and output return loss IRL and ORL in dB are [14]:

$$IRL = -20\log_{10}|\Gamma_a| \tag{2.26a}$$

$$ORL = -20\log_{10}|\Gamma_b| \tag{2.26b}$$

The input and output voltage standing wave ratio is given by

$$VSWR_{in} = \frac{1+|\Gamma_a|}{1-|\Gamma_a|} \tag{2.27a}$$

$$VSWR_{out} = \frac{1+|\Gamma_b|}{1-|\Gamma_b|} \tag{2.27b}$$

where Γ_a and Γ_b are [24]:

$$\Gamma_a = \left|\frac{\Gamma_{in}-\Gamma_s^*}{1-\Gamma_{in}\Gamma_s}\right| \tag{2.28}$$

$$\Gamma_b = \left| \frac{\Gamma_{out} - \Gamma_L^*}{1 - \Gamma_{out}\Gamma_L} \right| \tag{2.29}$$

For maximum power transfer, conjugate matching is required:

$$\Gamma_s = \Gamma_{in}^* \tag{2.30}$$

$$\Gamma_L = \Gamma_{out}^* \tag{2.31}$$

These conditions yield $\Gamma_a = 0$ and $\Gamma_b = 0$, and therefore $VSWR = 0$, $RL = -\infty$ [24].

2.2.5 Source Degeneration

Matching a microwave transistor for the best noise performance does not, in general, result in an optimum power match [16]. Inductive series feedback can help to achieve simultaneous noise and power matching. The addition of an inductor in series with the source of a transistor modifies the input impedance of the transistor, and if tuned correctly can allow simultaneous power and noise match. A small signal model of a transistor with inductive source degeneration is shown in Figure 2.8.

Before the addition of the inductor L_s, the input impedance of the transistor is:

$$Z_{in} = R_g - \frac{j}{\omega C_{gs}} \tag{2.32}$$

After adding L_s, the input impedance looking into the gate is [32]:

$$Z'_{in} = R_g + g_m \frac{L_s}{C_{gs}} + j\left(\omega L_s - \frac{1}{\omega C_{gs}}\right) \tag{2.33}$$

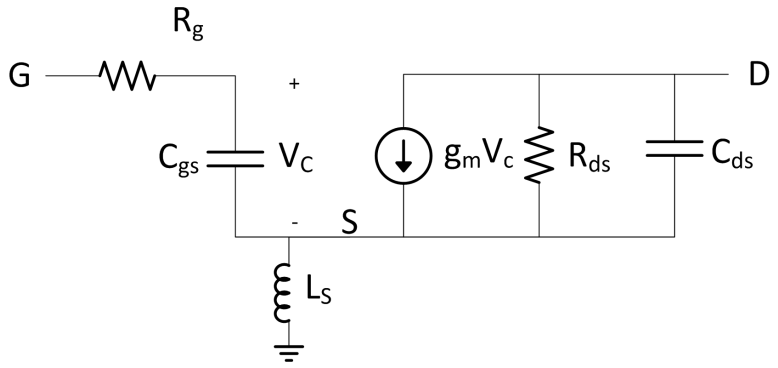

Figure 2.8: A simple small signal model of a transistor with inductive source degeneration.

The new input impedance Z'_{in} has an additional real component in series with R_g. This apparent real impedance does not add any noise of its own since it is a result of pure reactances [16, 33]. The addition of L_s partially cancels the negative reactance associated with C_{gs}. The result is that Z'^{*}_{in}, the impedance required for a conjugate input match to maximize power transfer, is closer to Γ_{opt}. Source degeneration has only a small effect on the optimal source impedance Γ_{opt} [31].

Inductive degeneration is an inherently narrow band technique. Because the effect of L_s on the imaginary part of the input reactance is frequency dependent, full cancellation occurs at only one frequency. Despite this limitation, it remains a useful tool for some broadband applications. L_s can also improve in band stability, although it may cause out of band gain peaking and hence instability [31, 34]. Selecting an appropriate amount of source inductance involves trading off these effects.

2.3 Low Noise Amplifier

The low noise amplifier (LNA) is a critical piece of the CHIME receiver. It is the first component that the signal encounters after being collected by the feed, so it has the largest impact on the overall noise performance, as shown by Equation 2.5. The performance metrics most important to the LNA are noise temperature, stability, transducer power gain, bandwidth, input return loss, output return loss, and linearity.

Choosing an appropriate transistor is an important step in designing an amplifier. GaAs high electron mobility transistors (HEMT) have been widely used in radio astronomy applications with success [24]. The Avagotech ATF-54143 is an enhancement mode pseudomorphic HEMT with a low noise figure and reasonably high gain in the CHIME frequency band. A design based on a common source amplifier using the ATF-54143 is presented here.

The ATF-54143 was chosen after simulating and testing prototype designs with several other Avagotech HEMTs, including the VMMK-1218, ATF-33143, ATF-35143, ATF-36077, ATF-38143, ATF-531P8, ATF-55143, and ATF-58143. The relatively large 800 μm gate width allows the ATF-54143 to accommodate more source inductance than smaller gate devices without becoming unstable [34]. To achieve the lowest possible noise figure, the ATF-54143 is biased with a DC drain current $I_D = 60$ mA and a drain source voltage of $V_{DS} = 3$ V.

After choosing a transistor and DC bias conditions, the input and output matching networks were designed iteratively. Hand calculations were used

to reach an approximate solution for 50 Ω source and load impedances. This design was simulated using Agilent's Advanced Design System, and adjusted accordingly. Prototype amplifiers were built and tweaked on the bench, and tested using 50 Ω measurement instruments.

All Smith charts in this section use are normalized with a characteristic impedance $Z_0 = 50\ \Omega$.

2.3.1 Matching Network Design

Designing the matching network consists of selecting Γ_s and Γ_L (Figure 2.5) to appropriately trade off the different performance parameters to best meet the design goals. As a first iteration, the reflection coefficients were selected using hand calculations and graphical techniques on the Smith chart for a 500 MHz amplifier using the ATF-54143.

Stability Circles

To test the stability of the transistor, the K-$|\Delta|$ criteria described in Equation 2.19 are used with the S parameters of the device provided by the manufacturer. At 500 MHz and $V_{DS} = 3$ V $I_D = 60$ mA, the result is

$$K = 0.293 \qquad |\Delta| = 0.410$$

The transistor is potentially unstable because $K < 1$.

Unconditional stability at all frequencies is desirable, but since the LNA will be connected to a known source and load, namely the feed and second stage amplifier, conditional stability may be sufficient. Plotting the values of

Γ_s and Γ_L that produce contours bounding stable operation aids in choosing Γ_s and Γ_L to produce a stable amplifier. The contours are found by setting Equation 2.18c and Equation 2.18d equal to 1. The result is circles in the Γ_s and Γ_L plane, called stability circles. The centre C and radius r are given by [24]:

Γ_L where $|\Gamma_{out}| = 1$:

$$r_L = \left| \frac{S_{12}S_{21}}{|S_{22}|^2 - |\Delta|^2} \right| \tag{2.34a}$$

$$C_L = \frac{(S_{22} - \Delta S_{11}^*)^*}{|S_{22}|^2 - |\Delta|^2} \tag{2.34b}$$

Γ_s where $|\Gamma_{in}| = 1$:

$$r_s = \left| \frac{S_{12}S_{21}}{|S_{11}|^2 - |\Delta|^2} \right| \tag{2.35a}$$

$$C_s = \frac{(S_{11} - \Delta S_{22}^*)^*}{|S_{11}|^2 - |\Delta|^2} \tag{2.35b}$$

The stability circles for the ATF-54143 at the chosen frequency and bias conditions are shown on the Smith chart in Figure 2.9. For stable operation with a 50 Ω source and load, Γ_s and Γ_L must be chosen in their respective stable regions. The further from the stability circles the reflection coefficients are, the more stable the amplifier is.

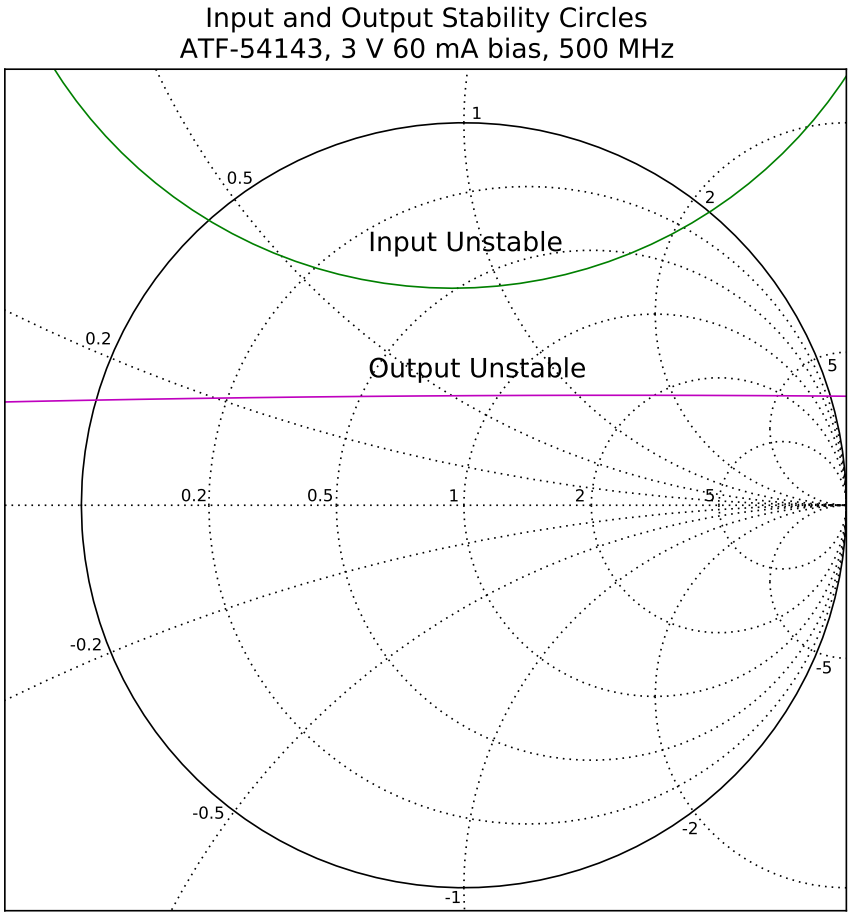

Figure 2.9: ATF-54143 stability circles at 500 MHz and $V_{DS} = 3$ V $I_D = 60$ mA in the Γ_s (input, green) and Γ_L (output, magenta) planes. $Z_0 = 50\ \Omega$.

Constant Noise Circles

The values of Γ_s which produce a constant noise figure lie on a circle in the Γ_s plane (Equation 2.16). The centre and radius of the circles are given by

$$r_{F_i} = \frac{1}{1+N_i}\sqrt{N_i^2 + N_i(1-|\Gamma_{opt}|^2)} \tag{2.36a}$$

$$C_{F_i} = \frac{\Gamma_{opt}}{1+N_i} \tag{2.36b}$$

where the parameter N_i is

$$N_i = \frac{NF_i - NF_{min}}{4r_n}|1+\Gamma_{opt}|^2 \tag{2.37}$$

for a given noise figure NF_i [24]. A few constant noise circles for the ATF-54143 are plotted in Figure 2.10 using the transistor noise parameters r_n and Γ_{opt} provided by the manufacturer.

Constant Available Gain Circles

To help determine a satisfactory trade-off between noise and gain, constant available gain G_A circles can be plotted in the Γ_s plane on the Smith chart. The radius and centre of the circles are given by [24]

$$r_a = \frac{\sqrt{1-2K|S_{12}S_{21}|g_a + |S_{12}S_{21}|^2 g_a^2}}{|1+g_a(|S_{11}^2 - |\Delta|^2)|} \tag{2.38a}$$

$$C_a = \frac{g_a(S_{11}-\Delta S_{22}^*)^*}{1+g_a(|S_{11}|^2-|\Delta|^2)} \tag{2.38b}$$

where K and Δ are given by Equations 2.21 and 2.20, and

$$g_a = \frac{G_A}{|S_{21}|^2} \tag{2.39}$$

Since the transistor is potentially unstable, available gain less than the maximum stable gain G_{MSG} must be chosen. The maximum stable gain is defined as the maximum transducer gain when $K = 1$, leading to [14]:

$$G_{MSG} = \frac{S_{21}}{S_{12}} \tag{2.40}$$

For the ATF-54143 at 500 MHz and $V_{DS} = 3$ V $I_D = 60$ mA, the maximum stable gain is 28.2 dB. Choosing available gain less than the maximum stable gain does not guarantee stability; Γ_s must still be selected in the stable region of the Smith chart. A few available gain circles are plotted in Figure 2.10 along with constant noise circles and the input stability circle.

Voltage Standing Wave Ratio Circles

The last considerations in selecting Γ_s and Γ_L are the input and output return loss, or voltage standing wave ratios (VSWR). To aid in selecting the load reflection coefficient Γ_L, contours of constant output VSWR can be plotted in the Γ_L plane. Like the noise and available gain, the contours of constant output VSWR are circles. The radius and centre of the constant

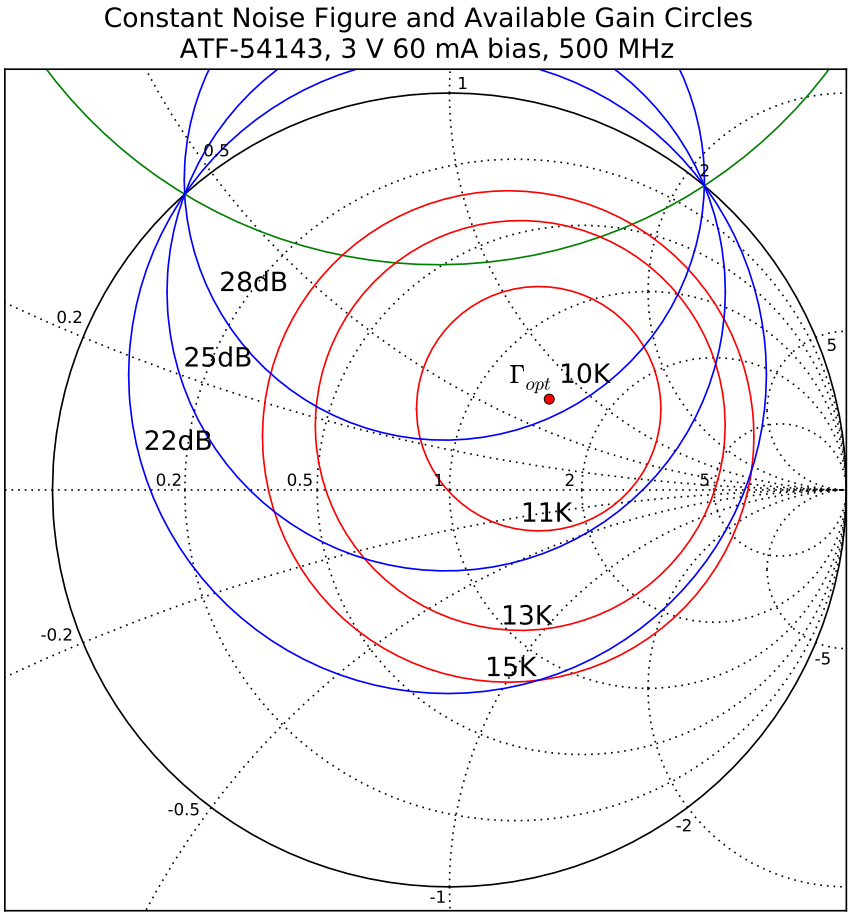

Figure 2.10: ATF-54143 noise (red), available gain (blue), and input stability (green) circles at 500 MHz and $V_{DS} = 3$ V $I_D = 60$ mA in the Γ_s plane. $Z_0 = 50\ \Omega$.

output VSWR circles are given by

$$r_{V_O} = \frac{|\Gamma_b|(1-|\Gamma_{out}|^2)}{1-|\Gamma_b\Gamma_{out}|^2} \tag{2.41a}$$

$$C_{V_O} = \frac{\Gamma^*_{out}(1-|\Gamma_b|^2)}{1-|\Gamma_b\Gamma_{out}|^2} \tag{2.41b}$$

where Γ_b is calculated for a chosen VSWR using Equation 2.27b. Constant output VSWR circles in the Γ_L plane corresponding to various choices for Γ_s are shown in Figure 2.11.

Γ_s and Γ_L Selection

Choosing appropriate values for Γ_s and Γ_L requires making trade-offs between noise, gain, input VSWR, and output VSWR, and stability must be ensured. First, several candidate selections are made for Γ_s based on the noise, available gain, and input stability circles. Second, using these selections for Γ_s, candidate selections for Γ_L are made using constant output VSWR and stability circles. Third, armed with this array of selections for Γ_s and Γ_L, the transducer gain, noise temperature, input VSWR, and output VSWR are calculated for each combination. Finally, selections that best suit the design goals are made. This process is summarized by Figure 2.11.

Since the noise temperature is the most important design criteria, the candidates for Γ_s lie on a constant noise circle ($T_n = 11$ K). For optimal stability, and to facilitate the use of a series C shunt L matching network (see Section 2.3.2), all choices for Γ_s lie on the lower right half of the 11 K constant noise circle (see Figure 2.10). For each of these values of Γ_s, there is a corresponding $\Gamma_L = \Gamma_{ML}$ that yields a conjugate match at the output

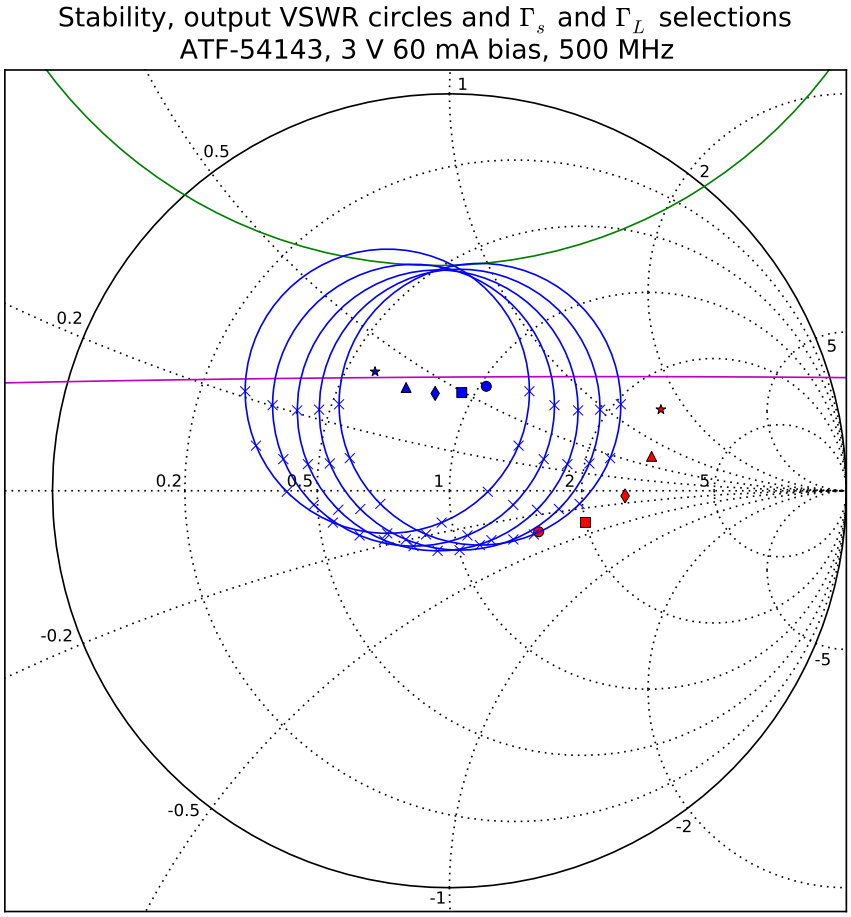

Figure 2.11: Candidate selections for Γ_s (red markers, Γ_s plane), the corresponding conjugate matched Γ_L points (blue markers, Γ_L plane), $VSWR_{out} = 2.5$ circles (blue, Γ_L plane) centred around the conjugate matched Γ_L points, several stable choices for Γ_L (blue x's, Γ_L plane), and the input (green, Γ_s plane) and output (magenta, Γ_L plane) stability circles. ATF-54143 at 500 MHz, $V_{DS} = 3$ V $I_D = 60$ mA. $Z_0 = 50\ \Omega$.

given by

$$\Gamma_{ML} = \Gamma_{out}^* = \left(S_{22} + \frac{S_{12}S_{21}\Gamma_s}{1 - S_{11}\Gamma_s} \right)^* \tag{2.42}$$

For each Γ_{out}^*, a constant $VSWR_{out} = 2.5$ circle is calculated using Equation 2.41. Candidate values for Γ_L are selected on the constant output VSWR circles below the output stability circle.

There are now several options for Γ_s, each with several corresponding options for Γ_L. For all combinations, the noise temperature is 11 K because the initial Γ_s choices lie on a noise circle, and the output VSWR is 2.5 because the Γ_L choices lie on an output VSWR circle. The input VSWR and transducer gain are calculated, and a suitable tradeoff is made, taking input and output stability into account. The final selections for Γ_s and Γ_L are

$$\Gamma_s = 0.25\angle{-25^\circ}; \quad Z = 77 - j17\ \Omega \tag{2.43a}$$

$$\Gamma_L = 0.16\angle{-61^\circ}; \quad Z = 56 - j16\ \Omega \tag{2.43b}$$

which yield specifications

$$T_n = 11 \text{ K}$$

$$G_T = 24.8 \text{ dB}$$

$$VSWR_{in} = 8.1; \quad IRL = -2.2 \text{ dB}$$

$$VSWR_{out} = 2.5; \quad ORL = -7.4 \text{ dB}$$

The input matching is very poor, but for an LNA attached directly to

an antenna, this may not be a significant problem; the high transducer gain and low noise performance are more important. The main concerns with this first iteration design are the broadband stability and performance, since the amplifier was designed only for 500 MHz. These concerns are addressed by optimizing the design through simulation, and testing and tweaking it on the bench.

2.3.2 Implementation

After choosing the input and output matching networks, an implementation must be designed to achieve the selected Γ_s and Γ_L and allow for DC biasing. Lumped components are used in the matching networks rather than transmission line stub matching because of the low maximum frequency. To reduce radiative leakage from the LNA coupling back into the feed, potentially creating a positive feedback loop and instability, the LNA circuit is sealed in an aluminum shielding box with SMA connectors at the input and output. A threaded 10,000 pF feed through capacitor (Tusonix 2425-601-X5W0-103Z) with 35 dB attenuation at 100 MHz and 70 dB attenuation at 1 GHz is used to bring the power supply voltage inside the box.

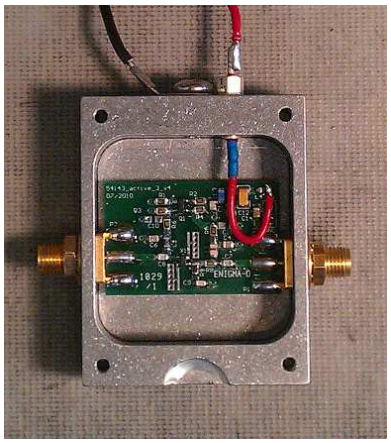

Figure 2.12: Low noise amplifier.

Matching Network

Series C shunt L networks at the input and output are used to reach the selected reflection coefficients on the Smith chart. This topology conveniently allows DC biasing of the transistor through the shunt inductance on the gate and drain, and AC couples the RF signal at the input and ouput of the amplifier through the series capacitance.

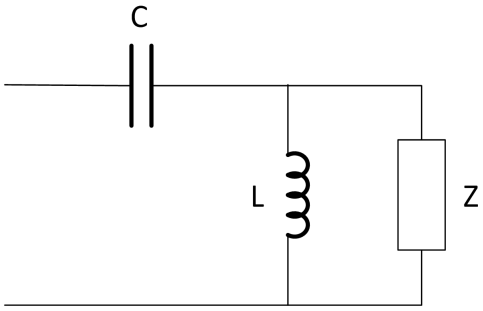

Figure 2.13: Series C shunt L matching network.

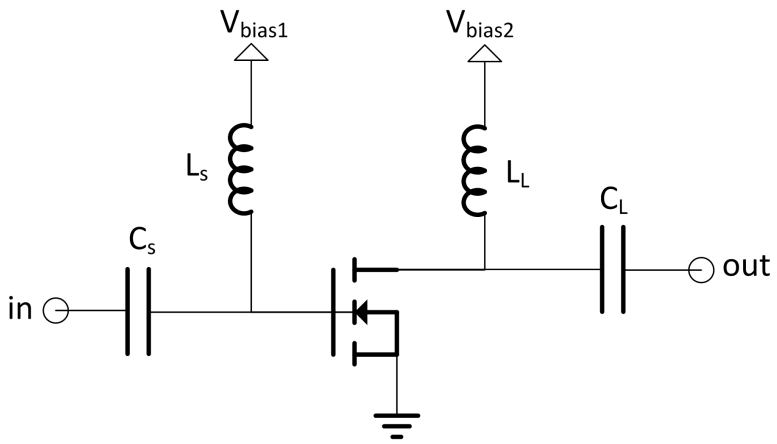

Figure 2.14: A basic schematic of the amplifier. The inductors L_s and L_L are used both as a part of the matching network and as a method of providing DC bias to the gate and drain of the transistor.

The admittance of the shunt inductor Y_L and impedance of the series capacitor Z_C required to transform Γ_s and Γ_L to 1 are calculated for $Z_0 = 50\ \Omega$ as

$$Y_{L,s} = 31j\ \Omega; \quad Z_{C,s} = -39j\ \Omega$$
$$Y_{L,L} = 30j\ \Omega; \quad Z_{C,L} = -23j\ \Omega$$

These admittances and impedances are converted to inductor and capacitor values at 500 MHz, yielding

$$L_s = 9.9\text{ nH}; \quad C_s = 8.2\text{ pF}$$
$$L_L = 9.5\text{ nH}; \quad C_L = 13.8\text{ pF}$$

The basic schematic of the amplifier is shown in Figure 2.14.

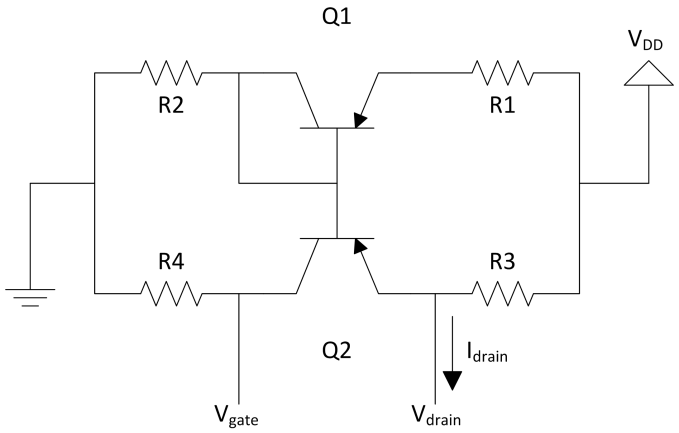

Figure 2.15: Schematic of the bias circuit using matched PNP transistors in a current mirror configuration.

DC Bias Circuit

There are many biasing schemes available for microwave amplifiers [24]. Active biasing is preferable to passive biasing because it is less sensitive to variations in passive component values. This helps the repeatability of amplifier characteristics and improves the temperature stability compared to passive biasing.

Since the ATF-54143 is an enhancement mode device, it requires a positive voltage to be applied to both its drain and gate in order to turn on. The biasing scheme used here employs a matched pair of bipolar transistors in a structure similar to a current mirror [35]. A schematic of the bias circuit is shown in Figure 2.15.

A reference current I_{ref} is chosen to be the collector current of both Q1 and Q2. Ignoring the difference in collector and emitter currents in the BJTs, the resistors R1-4 can be calculated as follows. R4 sets the gate

voltage V_{gate} on the amplifier transistor:

$$R4 = \frac{V_{gate}}{I_{ref}} \tag{2.44}$$

Choosing the desired drain current and drain voltage leads to the value of R3:

$$R3 = \frac{V_{DD} - V_{drain}}{I_{drain} + I_{C2}} \tag{2.45}$$

In order for both Q1 and Q2 to be in the active region, the emitter voltage of each transistor should be nearly the same (V_{drain}) since their base voltages are tied together. Since Q1 carries only the reference current, R1 will be approximately:

$$R1 \approx \frac{V_{DD} - V_{drain}}{I_{ref}} \tag{2.46}$$

Resistor R2 sets the reference current, and can be calculated as

$$R2 = \frac{V_{drain} - V_{be1}}{I_{ref}} \tag{2.47}$$

2.3.3 Simulation and Optimization

After reaching a first iteration solution for a narrowband amplifier at approximately the right frequency, the design must be upgraded to ensure it covers the full frequency band of interest, is stable at all frequencies, and practically realizable. This is done through a combination of simulation with Agilent's Advanced Design System (ADS), and prototyping and testing on the bench.

The final schematic of the full LNA reached through this procedure is

shown in Figure 2.16. Inductors L3 and L4, along with capacitors C12, C13, C14, and C1, are used for filtering the power supply voltage VCC=5 V after a feed through capacitor brings it inside the shielding box. Dual PNP transistor package Q1 and resistors R1-4 are used to generate the DC bias for the ATF-54143, X1, as described in Section 2.3.2. The input and output matching is accomplished using L2 and C8, and L1 and C7. High Q inductors and capacitors are used to minimize losses.

Capacitors C2 and C4 bypass the DC bias, and also affect the matching and in band stability. Resistors R5 and R6 and capacitors C10 and C11 provide low frequency terminations to improve low frequency stability.

Resistor R8 provides series loading at the output to improve broadband stability. The bias resistors R1-4 should be adjusted to account for the voltage drop across R5 and R8 to properly set the drain voltage. Resistor R9 provides shunt loading to improve stability, and C9 is added to shape the frequency response of the network to optimally trade off stabilization with gain reduction, in particular to target the high frequency gain peaking caused by the source degeneration inductance LS. To acheive the very small desired source inductance, LS is implemented as a piece of microstrip connecting the source of X1 to ground. The inductance is about 0.7 nH.

Resistor R10 and capacitor C15 provide drain to gate negative feedback. The feedback improves stability, input and ouput matching, and broadens the frequency response of the amplifier at the expense of some gain and noise figure.

ADS simulation results for the final design are shown in Figure 2.17. The simulations use S parameters and noise parameters provided by the

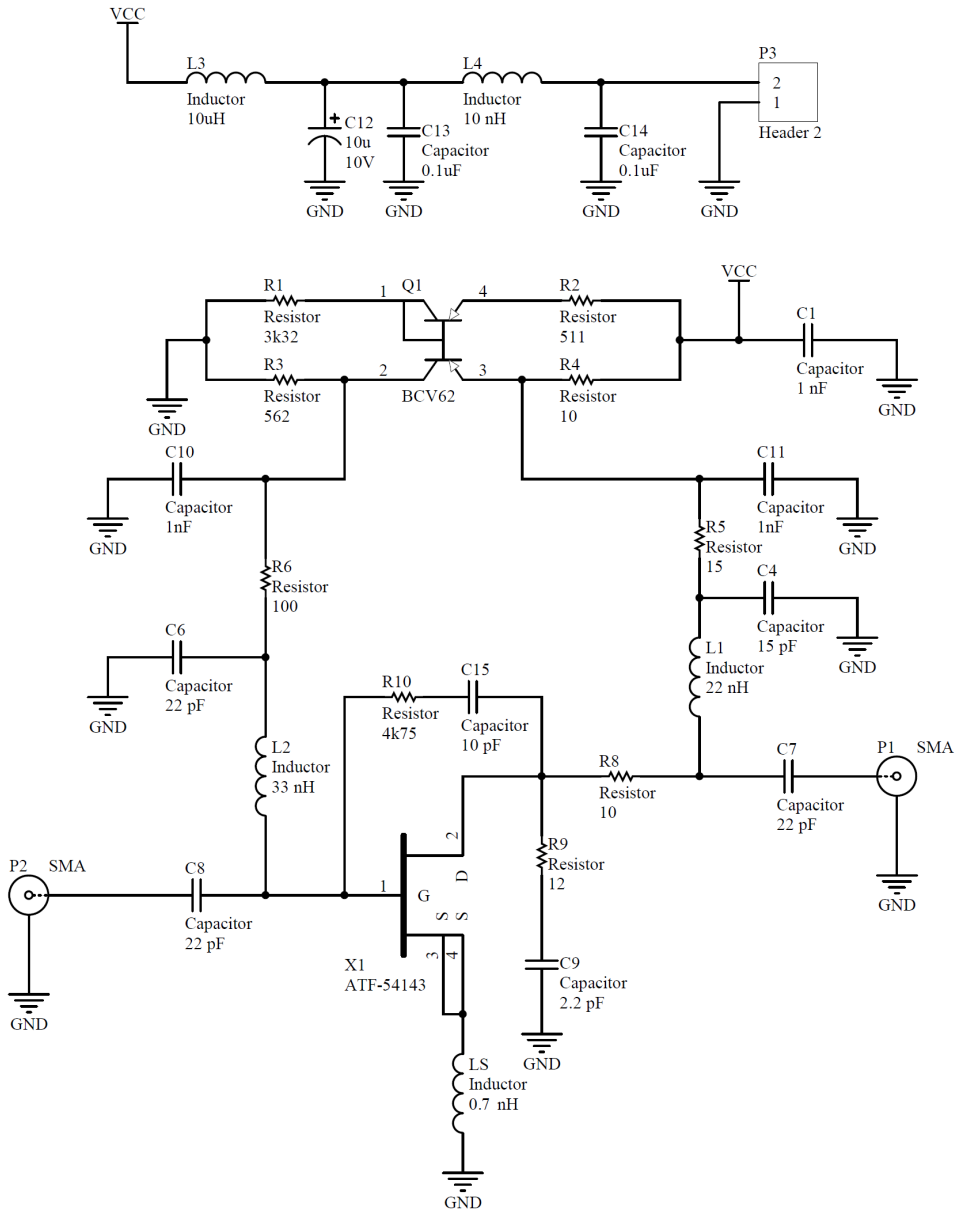

Figure 2.16: The final schematic of the LNA.

manufacturer over a range of frequencies from 0.1-18 GHz. The gain, noise temperature and matching are predicted to be quite good, but the amplifier is not predicted to achieve unconditional stability. The stability factor μ (Equation 2.22) drops below 1 between about 7 and 11 GHz, indicating potential instability in this region. This is a direct result of the source inductance causing out of band gain peaking near 8 GHz, as seen in Figure 2.17e. The potential instability at high frequency predicted by simulation is not observed in practice.

2.3.4 Lab Results

The LNA was tested using 50 Ω test equipment in the lab. The noise figure and transducer gain were measured with an HP8970B noise figure analyzer (NFA) and HP346B noise source. The S parameters were measured with an HP8753E vector network analyzer (VNA).

Noise and Gain

The noise and gain results are shown in Figure 2.18. The LNA has a noise temperature below 50 K above 400 MHz, and settles between 30 and 35 K above 500 MHz. The gain decreases smoothly from about 22 dB at 400 MHz to about 18 dB at 800 MHz. These results agree reasonably well with the simulation, although both the gain and noise are slightly worse than predicted. This is due in part to ohmic and dielectric losses in the connectors, FR-4 printed circuit board, and the input matching network C8 and L2. Comparing Figure 2.18b to Figure 2.17c shows that the overall shape from 0-1.6 GHz is very consistent with the simulation.

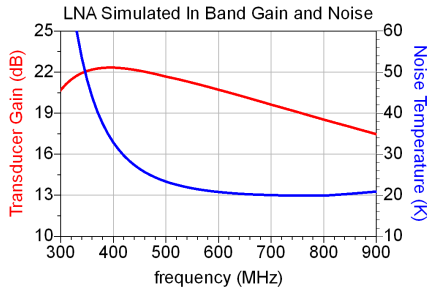

(a) In band gain and noise temperature

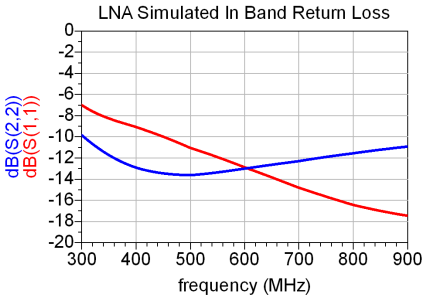

(b) In band return loss

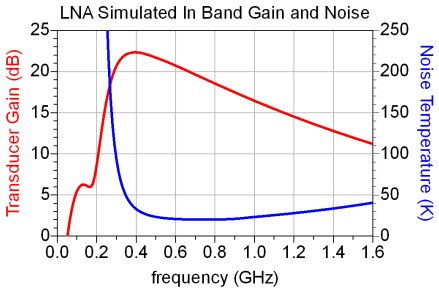

(c) Broadband gain and noise temperature

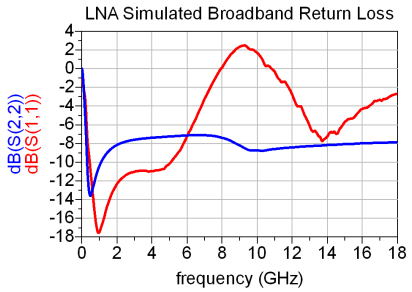

(d) Broadband return loss

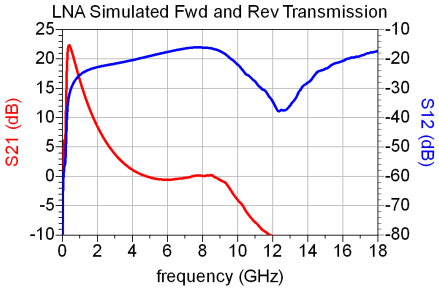

(e) Forward and reverse transmission

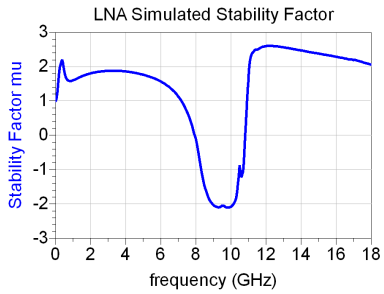

(f) Stability

Figure 2.17: LNA simulation results using Agilent's Advanced Design System.

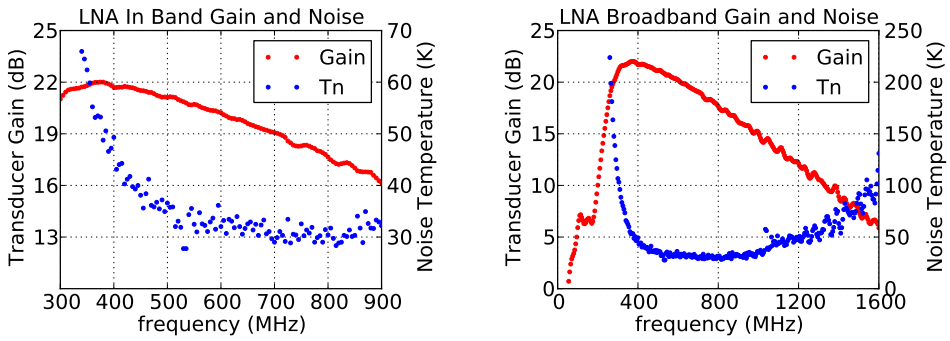

(a) In band (b) Broadband

Figure 2.18: LNA gain and noise measurements.

Noise Figure Measurement

The noise figure measurements were performed with an HP8970B NFA and an HP346B avalanche diode based noise source. The noise figure analyzer uses the Y-factor method. In this method, the noise source is switched between two states: a hot state, when the output noise temperature is high; and a cold state, when the output noise temperature is low. The two point measurement is linearly extrapolated to yield a slope and offset, from which the transducer gain and noise temperature of the device under test (DUT) are inferred.

The output power of the noise source in the cold state is the thermal noise of the 50 Ω source at the ambient temperature. The high noise power of the hot state is generated by biasing the avalanche diode inside the noise source into its breakdown region, where it produces a white output noise power proportional to the diode current [36]. The noise source internally includes an impedance matching circuit to ensure 50 Ω output impedance

across the frequency range of the device, and a regulator circuit to provide a constant current through the diode while in the hot state [37]. The hot noise power of the noise source is specified by its excess noise ratio (ENR) in dB

$$ENR = 10\log_{10}\left(\frac{T_{NS}^{hot} - T_{NS}^{cold}}{T_0}\right) \tag{2.48}$$

where T_{NS}^{cold} is assumed to be equal to T_0=290 K [38]. A table specifying the calibrated ENR values at different frequencies is provided with the device. If the physical temperature of the noise source T_{NS} is different from 290 K, a correction must be applied to the ENR [39]:

$$ENR_{corrected} = 10\log_{10}\left(10^{\frac{ENR}{10}} + \frac{T_0 - T_{NS}}{T_0}\right) \tag{2.49}$$

The Y-factor is defined as

$$Y = \frac{T_{hot}}{T_{cold}} \tag{2.50}$$

where T_{hot} and T_{cold} are the noise powers measured by the NFA while the noise source is in its hot and cold states. To properly measure the noise figure of the DUT only, a calibration step must be performed. The calibration measures the noise temperature of the instrument itself T_{instr} by measuring noise powers T_{instr}^{hot} and T_{instr}^{cold}. After calibration, the DUT is inserted between the noise source and NFA, and the Y-factor of the DUT and instrument combined is measured:

$$Y_{comb} = \frac{T_{comb}^{hot}}{T_{comb}^{cold}} \tag{2.51}$$

The combined noise temperature T_{comb} is

$$T_{comb} = \frac{T_{NS}^{hot} - Y_{comb} T_{NS}^{cold}}{Y_{comb} - 1} \tag{2.52}$$

The transducer gain G_{DUT} and noise temperature T_{DUT} are [39]:

$$G_{DUT} = \frac{T_{comb}^{hot} - T_{comb}^{cold}}{T_{instr}^{hot} - T_{instr}^{cold}} \tag{2.53}$$

$$T_{DUT} = T_{comb} - \frac{T_{instr}}{G_{DUT}} \tag{2.54}$$

There are various sources of uncertainty in a noise figure measurement. These include unavoidable sources such as uncertainty in the ENR of the noise source, changes in the output impedance of the noise source between its hot and cold states, mismatch between the components, and uncertainty in the noise figure and gain linearity of the instrument itself. Avoidable or correctable sources of error include external RFI, non-linearity in the DUT or instrument, temperature effects, loss in the system, and measurement jitter.

The HP346B noise source has a nominal ENR of 15 dB. Adding 10 dB of attenuation at the output reduces the ENR to about 5 dB, improves the mismatch uncertainty, and drastically reduces the difference in output impedance between the hot and cold state, as shown in Figure 2.19. It is better to use a low ENR noise source when possible because the lower power levels reduce the chance of non-linearity, the internal noise figure of the instrument may be decreased due to less required internal attenuation, and the difference in impedance between the hot and cold states is smaller

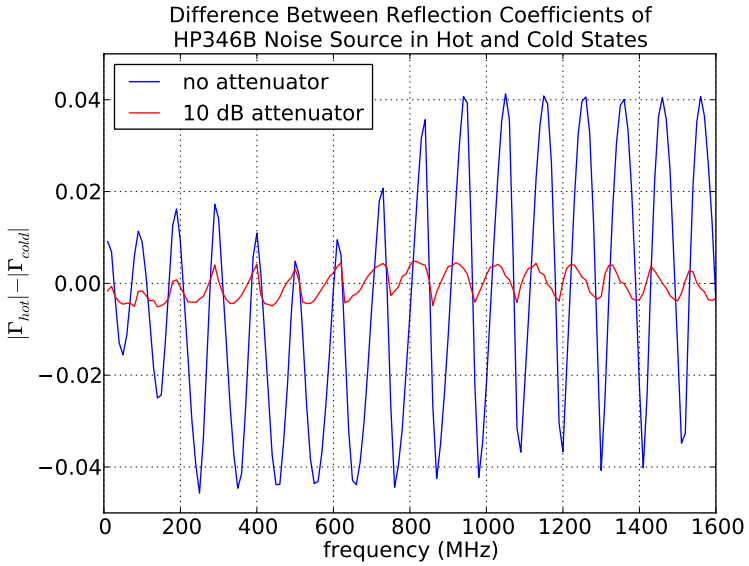

Figure 2.19: HP346B noise source reflection coefficient differences in hot and cold state with and without 10 dB attenuator at the output.

[39].

A full uncertainty calculation for the LNA noise figure measurement was performed following [39, 40]. The resulting systematic uncertainty δT_n in the noise temperature varies from about 8-13 K in band. The largest contributions to the uncertainty are the ENR of the noise source, the inherent HP8970B instrument uncertainty, and the mismatch between the noise source and the DUT. The mismatch error at both ports includes the use of transducer gain G_{DUT} in the correction for the instrument internal noise (Equation 2.54) instead of the available gain. The in band noise temperature including bounding uncertainty curves is shown in Figure 2.20.

It should be noted that the precise meaning of the uncertainties reported in the technical documentation of the instruments is unclear. This includes

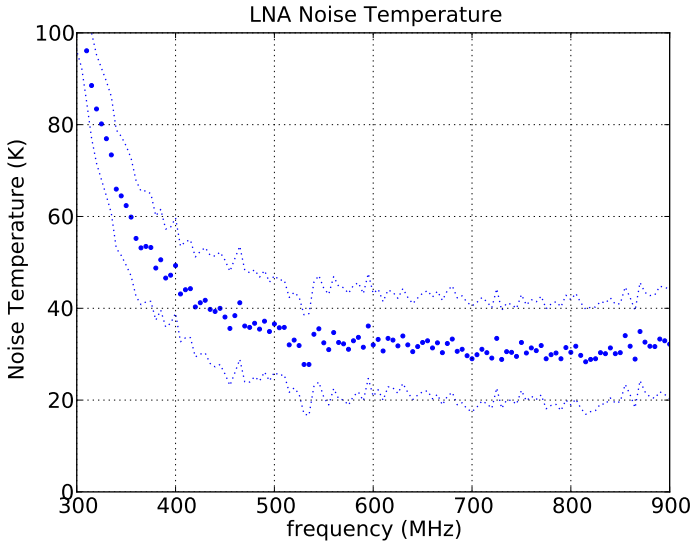

Figure 2.20: LNA measured noise temperature with bounding uncertainty curves.

two of the most important contributions to the measurement uncertainty: the HP8970B noise figure uncertainty and the HP346B ENR uncertainty. The reported values are treated here as 1σ errors.

The measured noise figure does not correct for the difference in impedance between the hot and cold states of the noise source. This correction would require full knowledge of the dependence of the DUT gain and noise on the source impedance, which is a difficult and expensive measurement. Instead, the error resulting from this effect is minimized through the use of the 10 dB attenuator at the output of the noise source as described above.

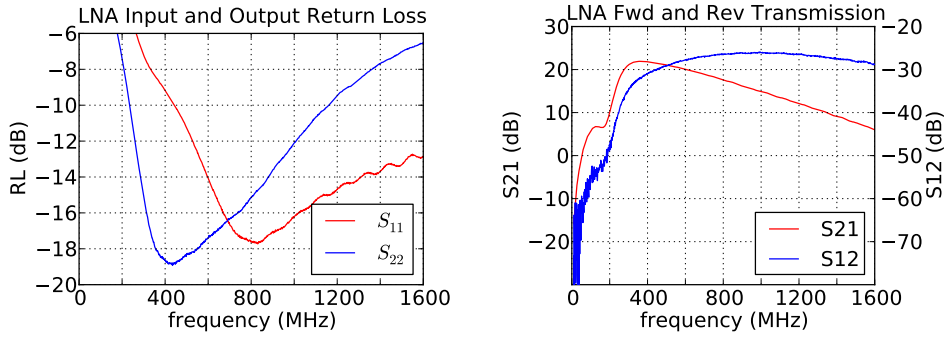

(a) Return loss

(b) Forward and reverse transmission

Figure 2.21: LNA S parameter measurementss

S Parameters

The measured S parameters are shown in Figure 2.21. The forward transmission $|S_{21}|$ is equivalent to the transducer gain measured by the noise figure analyzer. The complex input and output impedance is shown in Figure 2.22.

Linearity

The linearity of the LNA is quantified using the 1 dB compression point. The output 1 dB compression point at 600 MHz is $P_{O1dB} = 24.3$ dBm. The measurement is shown in Figure 2.23.

Stability

The stability of the amplifier is difficult to quantify. To gain some insight to the amplifier's resistance to oscillation, the LNA was connected to a spectrum analyzer, and the power spectrum thoroughly examined for signs of instability. This process was repeated for various input loads: a 50 Ω ter-

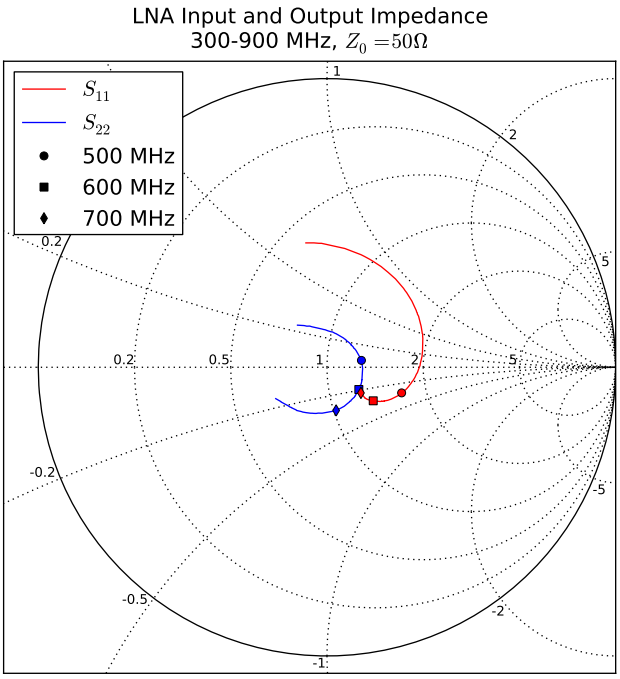

Figure 2.22: Measurement of the LNA complex input and output impedance.

mination, an open circuit, a short circuit, and a feed inside a small isolating chamber filled with absorber. This setup is a crude approximation of a termination with the impedance of the antenna. To raise the output power level of the amplifier above the noise floor of the spectrum analyzer, a second LNA was connected after the first LNA.

The results of all four input loads are shown in Figure 2.24. None of the spectra contain signs of oscillation. The spectra are also useful for comparing the LNA operation under different input loads; specifically, the comparison between operation with a 50 Ω termination at the input — as the amplifier

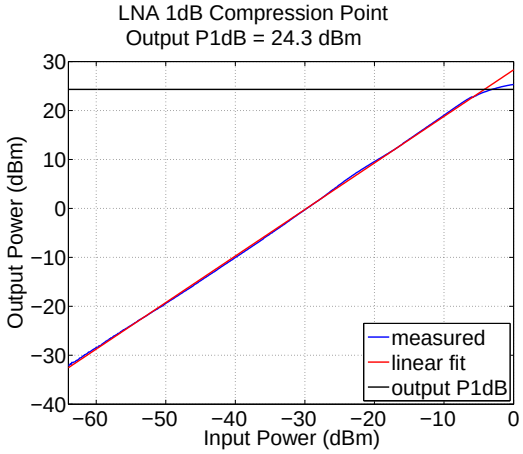

Figure 2.23: Measurement of the LNA output 1 dB compression point at 600 MHz.

was designed for and tested with — and operation with a feed at the input could reveal potential problems with the LNA on the final instrument. In band, the terminated input and the feed look similar (Figure 2.25).

2.4 Later Amplification and Filtration

After the LNA, further amplification is required to boost the power to a level sufficient for digitization, and allow the signal to be transported over some distance without cable loss seriously compromising the signal integrity. Also, a band defining filter is required to avoid intermodulation distortion products resulting from out of band RFI mixing into the band of interest, facilitate aliased sampling, and remove out of band noise power. These goals are achieved through the use of a combined second stage amplifier and filter that immediately succeeds the LNA in the signal path.

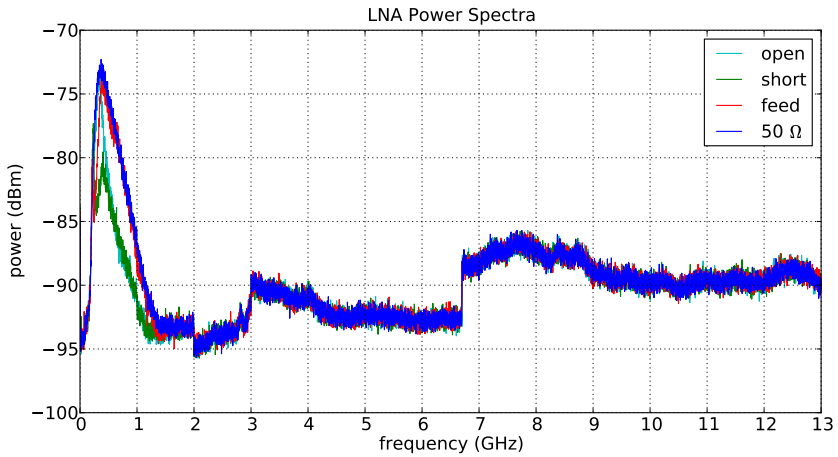

Figure 2.24: LNA power spectra collected with four different loads at the input. There are no signs of instability. The jumps at 2, 3, and 6.7 GHz are artifacts of the spectrum analzyer baseline.

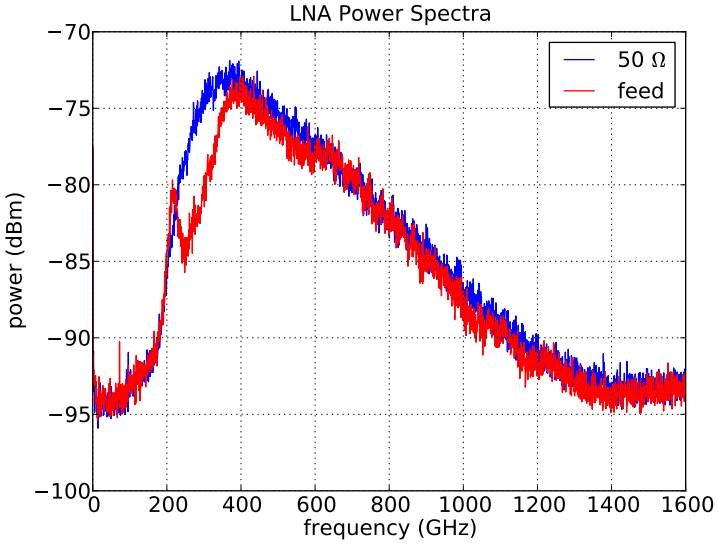

Figure 2.25: Power spectra collected with the LNA input connected to a 50 Ω termination, and a feed inside an isolating chamber lined with absorber.

To get a rough idea of the total gain required for the full analog receiver chain, the typical input power to each channel of the receiver can be estimated as 100 K in a 425 MHz bandwidth, or about -92 dBm. To boost the power to about -20 dBm, which is an appropriate level for the digitizer (see Section 2.6), about 70 dB of gain is required. The LNA accounts for approximately 20 dB, leaving 50 dB to be added by the later amplification stages. The signals originating at the focus are carried by 50 m long LMR-400 low loss 50 Ω coaxial cables to the digitizer and back end. The cable attenuation is less than 6.4 dB below 900 MHz. Amplification of greater than 60 dB is necessary to sufficiently boost the power level and leave some margin to allow for impedance matching attenuation pads. Gains measured in the lab using 50 Ω test equipment should be higher still to allow margin for mismatch between amplifier stages.

Since the receiver does not use any mixing or down sampling, it is difficult to have all of the gain at the focus without leakage coupling from the output to the input, inducing oscillations. To avoid this, the remaining gain after the LNA is divided between each end of the 50 m coaxial cable connecting the focus and the digitizer. The circuits are also independently shielded with aluminum boxes including SMA inputs and outputs, and use Π-type LC threaded feed through filters (Tusonix 4251-004LF) with more than 75 dB of attenuation above 100 MHz to bring the supply voltage inside the box. The circuit inside the box at each end of the cable is identical, consisting of an amplifier, followed by a filter, followed by a second amplifier identical to the first. A block diagram of the circuit is shown in Figure 2.26, and the circuit in the shielding box is shown in Figure 2.27.

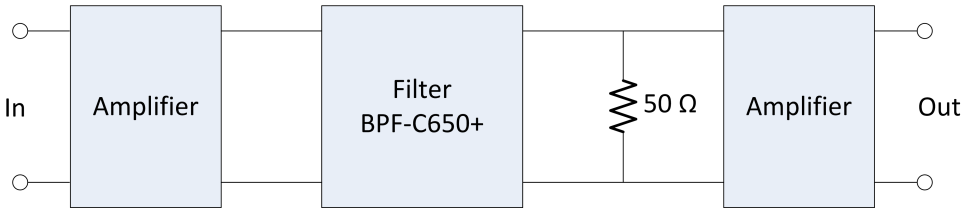

Figure 2.26: Block diagram of the circuit to provide gain and define the frequency band.

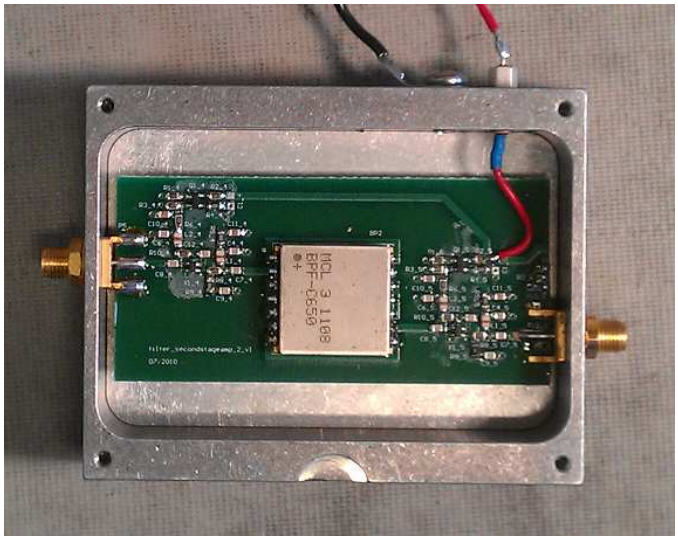

Figure 2.27: The second stage amplifier and filter box.

The filter is an off the shelf component supplied by Mini-Circuits: the BPF-C650+. The amplifiers on either side of the filter are similar to the LNA, but include no added source inductance, more drain to gate feedback, and more ouptut resistive loading. The ATF-54143 is again used at the same bias point, V_D=3 V I_D=60 mA, with the same DC bias circuitry (Section 2.3.2). A schematic of the amplifier is shown in Figure 2.28. In order to improve the matching between the filter and the input of the second amplifier in the circuit, a 50 Ω shunt resistor is added at the output of the filter (see Figure 2.26). The shunt resistor adds loss and thermal noise to the system, but occurs after enough gain that the overall contribution to the noise temperature of the system is small. Since there are two stages of amplification inside a sealed box, radiative coupling from the output to input can occur. To suppress this effect, RF absorbing foam is placed inside the box.

The measured noise figure and gain are shown in Figure 2.29, and the S parameters in Figure 2.30. The linearity of the full receiver chain, including the LNA followed by two second stage filters, is characterized using the output 1 dB compression point at 600 MHz. The result, plotted in Figure 2.31, is $P_{O1dB} = 22.8$ dBm.

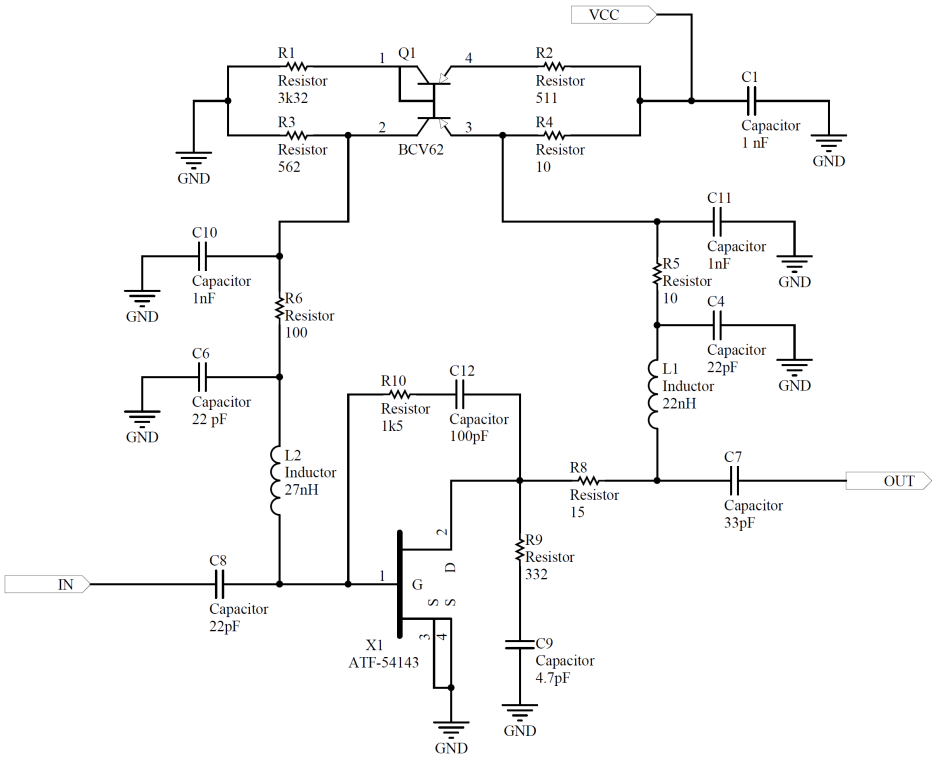

Figure 2.28: Schematic of the amplifier on either side of the filter in the second stage amplifier and filter circuit.

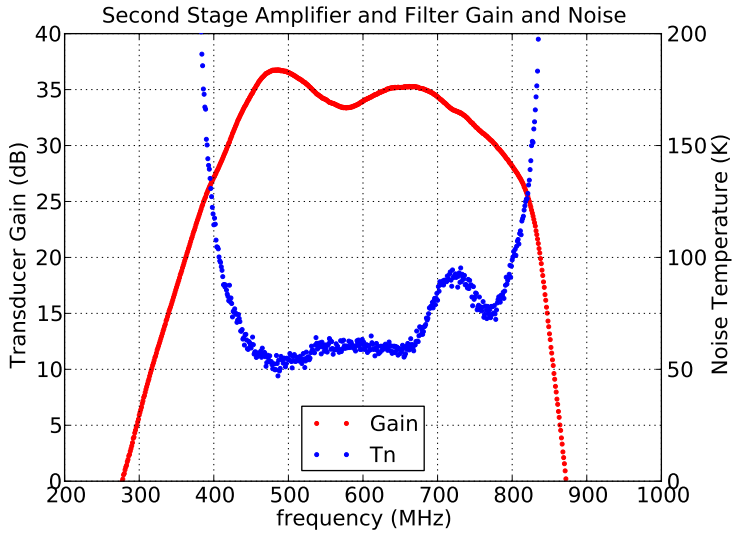

Figure 2.29: The transducer gain and noise temperature of the second stage amplifier and filter circuit.

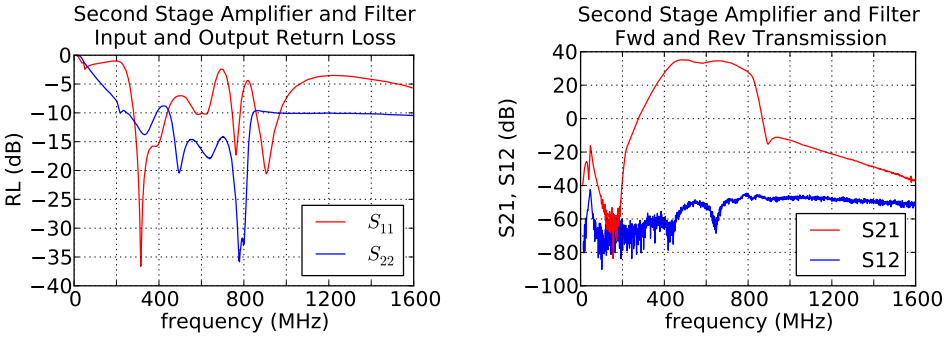

(a) Return loss

(b) Forward and reverse transmission

Figure 2.30: Second stage amplifier S parameter measurements.

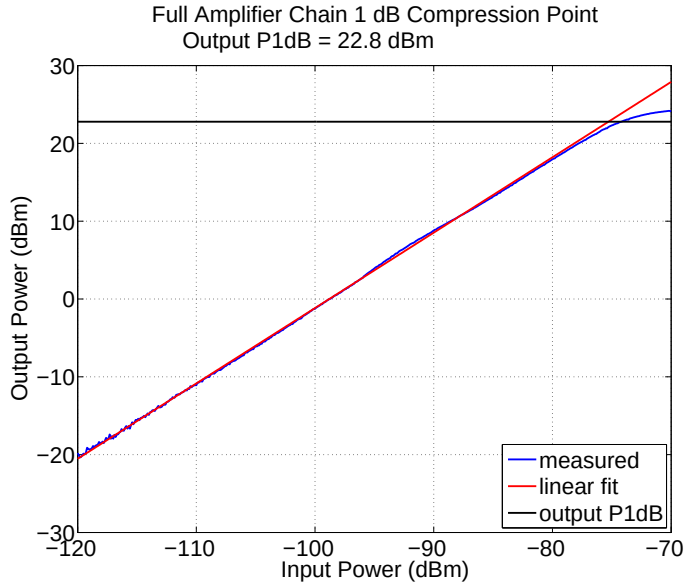

Figure 2.31: Output 1 dB compression point at 600 MHz of the analog receiver, including an LNA and two second stage amplifier and filter boxes.

2.5 Feed

The CHIME feed is based on a dual linear polarization wideband four square dipole design, originally intended for use in a line array on the cylindrical reflectors at the Molonglo Observatory Synthesis Telescope (MOST) and Square Kilometre Array Molonglo Prototype (SKAMP) [41]. MOST is a cylindrical reflector radio telescope operating at 843 MHz, and SKAMP is an upgrade to MOST with a wide bandwidth intended to demonstrate technologies for the Square Kilometre Array[3] (SKA) [42]. The feed used here scales the design from the original bandwidth of 700-1100 MHz to a

[3] `http://www.skatelescope.org`

centre frequency of 650 MHz for use with CHIME.

2.5.1 Design

The feed geometry is shown in Figure 2.32. The four square wideband dipole is made up of double sided copper plated 1.57 mm printed circuit board (PCB) located $\lambda/4$ below a ground plane. The two layers of copper are connected using vias to approximate a single piece of metal. Each pair of adjacent squares on the arm board forms a linear wideband dipole; the A-B and C-D pairs excite one polarization, and the A-C and B-D pairs excite the orthogonal polarization. The outputs of the common polarizations are fed in pairs to invididual single ended outputs on the baseboard. To achieve this, microstrip lines designed to act simultaneously as baluns and provide impedance matching are implemented on four PCBs. These boards also mechanically support the feed hanging below the ground plane. The microstrip lines continue from the four support boards to a base board, where the signals are summed into two SMA connectors, each of which corresponds to one of the linear polarizations.

The impedance of each polarization dipole element at the feeding point connecting to the microstrip baluns is $Z_{ant} = 23.0 + j0.8\ \Omega$ at the centre frequency, according to simulations [41]. This impedance should be transformed to 50 Ω to match it to the LNA input. The phase of the signals from each polarization should be preserved so that they can be directly summed at the SMA connector on the baseboard; thus, the microstrip baluns for each signal should be identical. The antenna is built out of FR-4 substrate PCB using 1 oz copper. The properties of FR-4 used to fabricate the feed

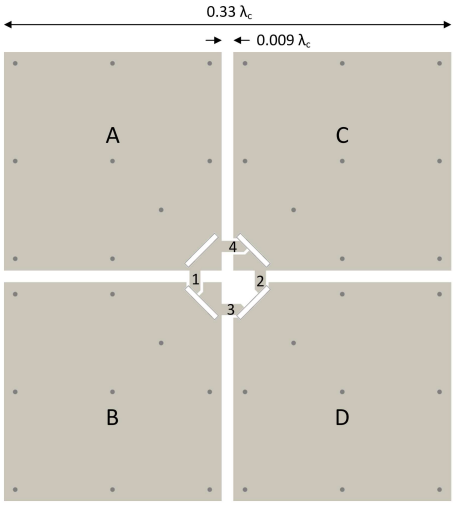

(a) Four square broadband dipoles (arm board top view). The AB and CD pairs form wideband dipoles in one linear polarization, and the AC and BD pairs form wideband dioples in the orthogonal linear polarization.

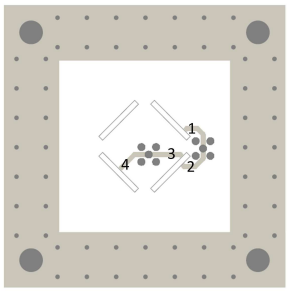

(b) Base board(bottom view). The two linear polarizations are summed in phase at the SMA connectors.

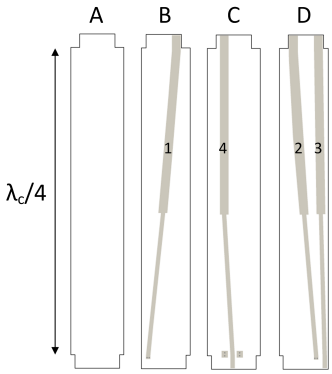

(c) Support boards, microstrip track side. The opposite side is a metallized layer acting as a ground plane.

(d) Full assembled feed

Figure 2.32: Layout and final geometry of the feed.

Dielectric constant (1 GHz)	4.35 ± 0.2
Loss tangent (1 GHz)	0.022 ± 0.002
Substrate thickness	1.57 mm
Copper thickness	35 um (1 oz)

Table 2.1: Technical specifications of the FR-4 substrate used to fabricate the feed.

boards are shown in Table 2.1.

Two quarter wave transformers are used to transform the real part of the antenna impedance Z_{ant} to the reference impedance $Z_0 = 50\ \Omega$. The impedance is transformed from Z_{ant} to an arbitrary impedance $Z_B = 92\ \Omega$ at the boundary between the two quarter wave transformers, and Z_B is transformed to Z_0. At the centre frequency f=650 MHz, the wavelength λ=221 mm in FR-4 is calculated using

$$\lambda = \frac{c}{f\sqrt{\epsilon_r \mu}} \tag{2.55}$$

where c is the speed of light in a vacuum, and μ=1 and ϵ_r=4.35 are the permeability and permittivity of FR-4. A schematic is shown in Figure 2.33. The quarter wave stripline impedances Z_{QW} are calculated using

$$Z_{QW} = \sqrt{Z_L Z_S} \tag{2.56}$$

where Z_L is the load impedance and Z_S is the source impedance [14]. The small reactive portion of Z_{ant} is capacitive, and will be partially mitigated by the inductance of the series transmission lines.

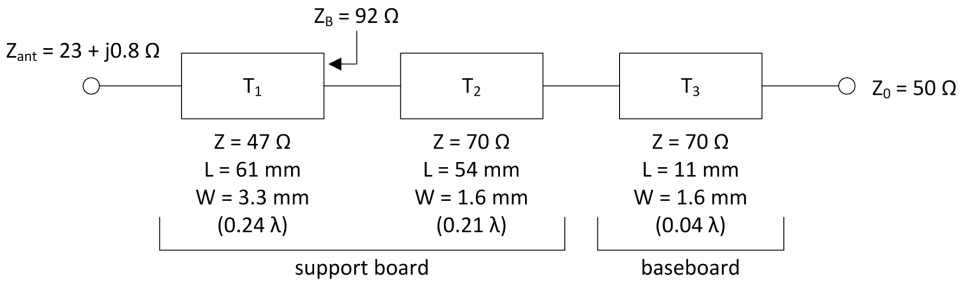

Figure 2.33: The transmission lines used to match the antenna impedance to the LNA impedance.

2.5.2 Loss

The electromagnetic signal coupled into the feed must propagate in an imperfect environment, resulting in some loss. This loss contributes directly to the system noise.

There is loss in the dipole elements due to the dielectric. According to simulation in CST Microwave Studio, this loss is about 4 K at 860 MHz [41]. The microstrip baluns connecting the dipole to the LNA also introduce loss, which was calculated in AWR TX-LINE. Each section of transmission line in the balun, T_1, T_2 and T_3, contribute some loss. The breakdown of feed loss at 600 MHz is shown in Table 2.2. The FR-4 substrate parameters for 1 GHz were applied directly to the calculation at 600 MHz. Over the frequency range of interest, the loss tangent of FR-4 is nearly constant. The dielectric constant increases with decreasing frequency, increasing loss; however, the decrease between 400 and 800 MHz is expected to be less than 5% [43], so the overall uncertainty in the loss calculation is dominated by the uncertainty in the 1 GHz substrate parameters.

Element	Dielectric Loss	Conductor Loss	Total Loss
Dipole	3 K		3 K
T_1	8.1 K	1.5 K	9.6 K
T_2	6.7 K dB	1.6 K	8.3 K
T_3	1.4 K dB	0.3 K	1.7 K
total	19.2 K	3.4 K	**23 K ± 3 K**

Table 2.2: Feed loss at 600 MHz

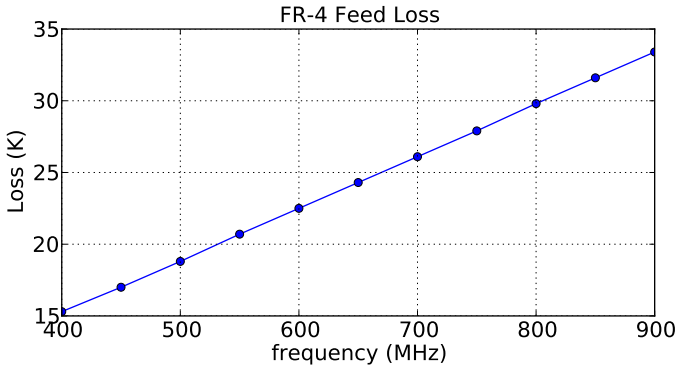

Figure 2.34: The total (dielectric plus conductor) loss in the feed assuming spectrally constant 1 GHz FR-4 substrate loss tangent and dielectric constant.

The total feed loss across the frequency band is shown in Figure 2.34 assuming a constant loss tangent and dielectric constant given by Table 2.1.

The transmission line baluns may be partially radiative. This contribution of the feed to the overall system temperature is measured in the antenna pattern and included indirectly in the antenna spillover (see Section 3.4.3).

2.5.3 Measured Results

The feed impedance was measured in the lab using an HP8753E vector network analyzer. The complex impedance of one polarization of the feed over a ground plane is shown in Figure 2.35. The in band impedance is matched closer to 25 Ω than 50 Ω. The return loss of both polarizations of the feed over a ground plane both with and without the isolating cylinder (Figure 2.3) is shown in Figure 2.36. The -10 dB impedance bandwidth extends from approximately 580 to 850 MHz. Adding the isolating cylinder to the ground plane improves the optimal match, but slightly reduces the bandwidth.

The co-polar far field radiation pattern was measured with and without an isolating cylinder at 600 MHz. The results are shown in Figure 2.37. The cylinder narrows the main lobe of the beam as expected, but also increases the side lobe levels.

2.5.4 Low Loss Feed

The feed loss can be significantly reduced by building the feeds out of higher quality substrate. A new feed was manufactured using Rogers RT/Duroid 5880, a speciality low loss laminate designed for high frequency stripline applications[4]. The substrate parameters are shown in Table 2.3.

The design also used the measured performance of the original feed to improve the matching at the centre frequency. Specifically, the lengths and widths of the quarter wavelength transformers used as baluns were adjusted

[4] `http://www.rogerscorp.com`

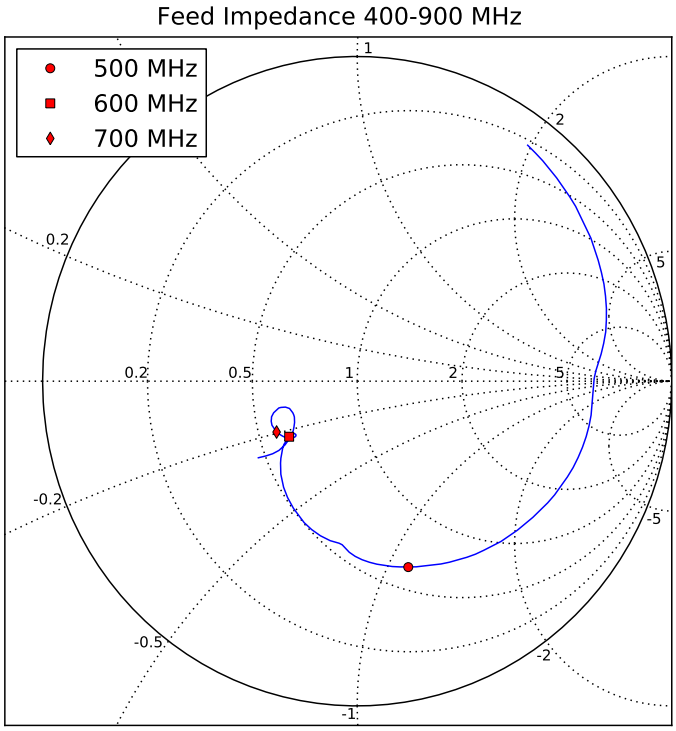

Figure 2.35: The complex impedance of the feed without an isolating cylinder on the ground plane.

Dielectric constant (up to 40 GHz)	2.2 ± 0.02
Loss tangent (10 GHz)	0.0009
Substrate thickness	1.57 mm
Copper thickness	35 um (1 oz)

Table 2.3: Technical specifications of the Rogers RT/Duroid 5880 substrate used to fabricate the low loss feed.

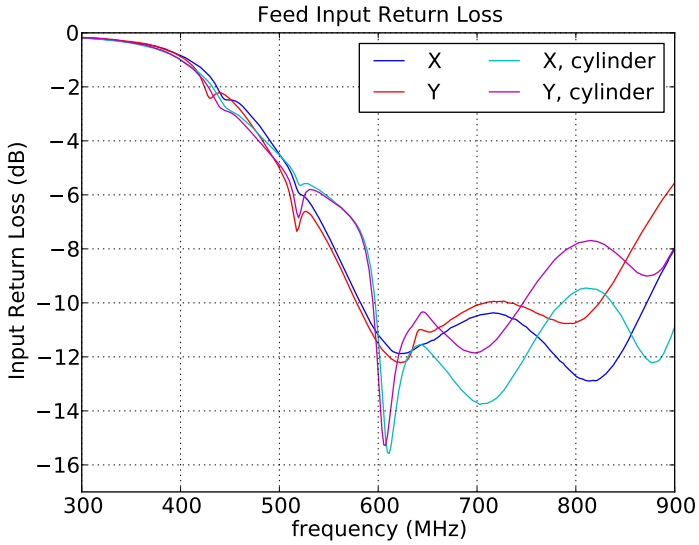

Figure 2.36: The input return loss of the feed with and without an isolating cylinder on the ground plane.

to increase the real part of the feed impedance closer to 50 Ω.

The measured impedance of the new feed is shown in Figure 2.38. The resistive part of the impedance has indeed moved closer to 50 Ω in the middle of the band, but the reactance has increased so that the overall reflection coefficient is similar to the original feed. The return loss for both polarizations both with and without an isolating cylinder on the ground plane is shown in Figure 2.39. The bandwidth is similar to the original feed.

The total loss at 600 MHz for the feed using the low loss substrate is approximately 5 K.

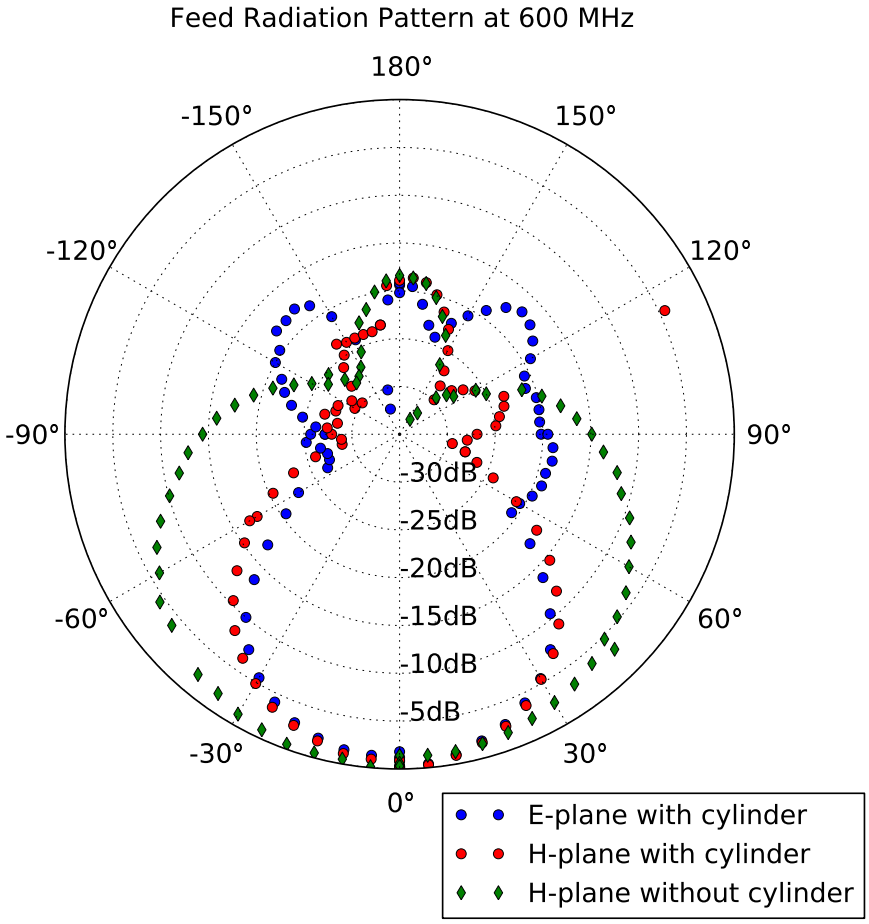

Figure 2.37: The 600 MHz co-polar far field feed radiation pattern.

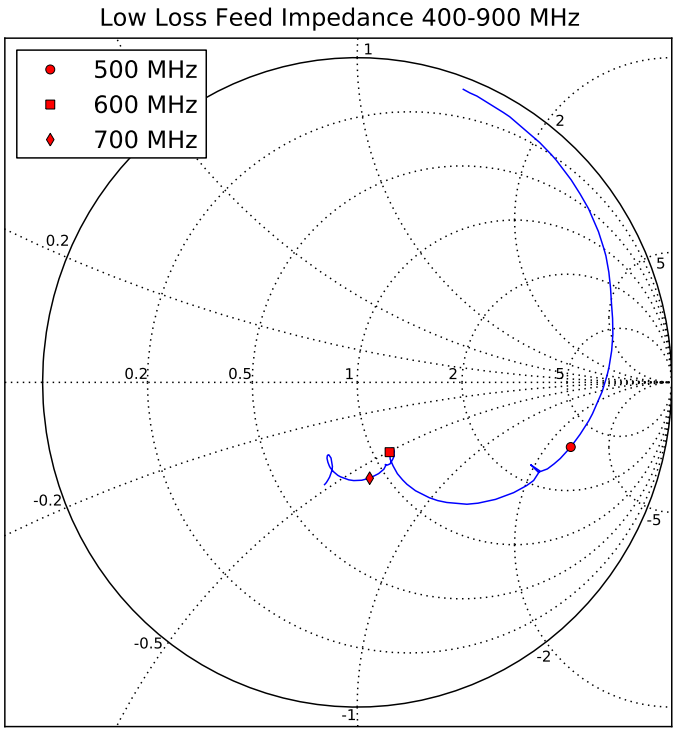

Figure 2.38: The complex input impedance of the low loss feed without an isolating cylinder on the ground plane.

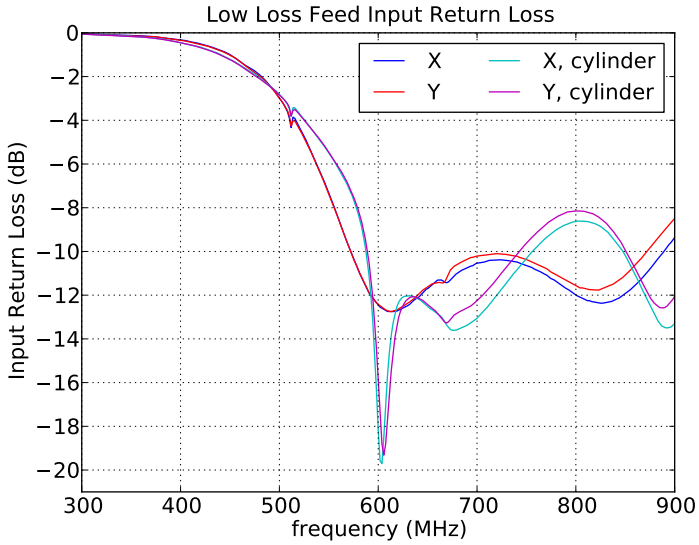

Figure 2.39: The input return loss of the low loss feed with and without an isolating cylinder on the ground plane.

2.6 Back End

The back end electronics consist of two input ADC boards and a ROACH board correlator developed by CASPER. The input ADC board uses an Atmel AT84AD001B dual channel 8 bit 1 GS/s ADC. The AT84AD001B is also capable of interlacing samples from the two channels to emulate a single channel 8 bit 2 GS/s ADC. The ROACH processing board is built around a Xilinx Virtex5 FPGA, and has a 10G ethernet interface.

The ADC is clocked at 850 MHz, and this clock is divided by four to clock the FPGA at 212.5 MHz. The FPGA reads the ADC samples, and each digitized channel is processed with a polyphase filter bank, including a four tap finite impulse response (FIR) filter and a 2048 point Hamming

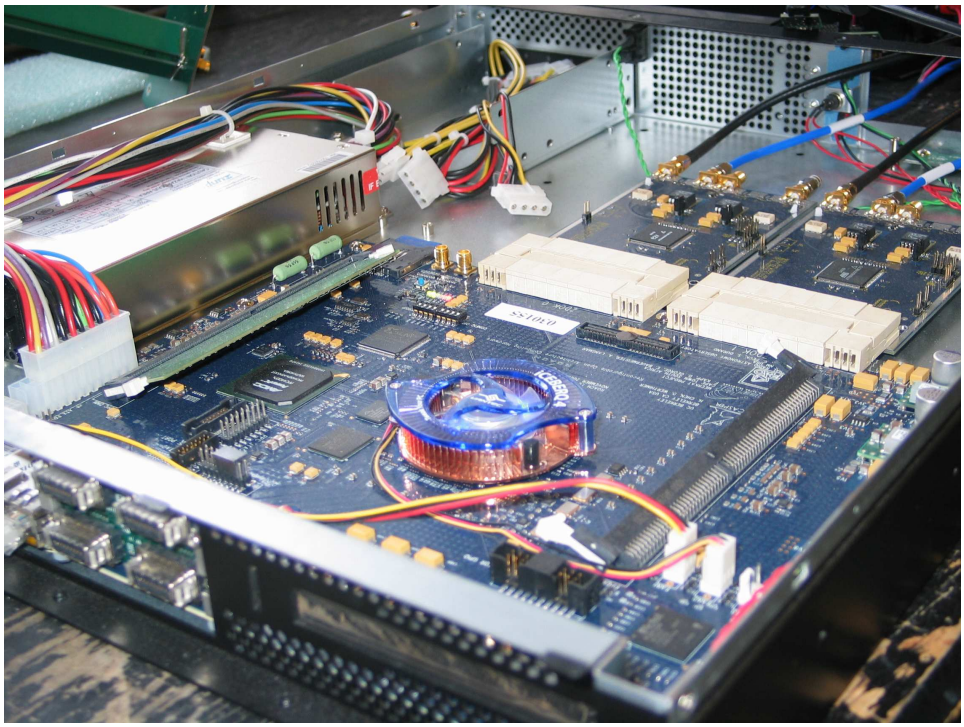

Figure 2.40: The ADCs and ROACH correlator.

window.

Each 2048 point window is Fourier transformed with 36 bit precision (18b real and 18b imaginary). The result is quantized to 8 bits (4b real and 4b imaginary) after applying a complex gain to each frequency to ensure all of the 8 available bits are exercised appropriately. The 8 bit quantized Fourier tranform results of each of the four channels are cross correlated and autocorrelated to form all ten possible correlation products in the frequency domain (four autocorrelations and six cross correlations). The ten correlation products are averaged over 2^{19} samples to 32 bit precision and written to RAM. A power PC running Linux reads the RAM and sends the data over

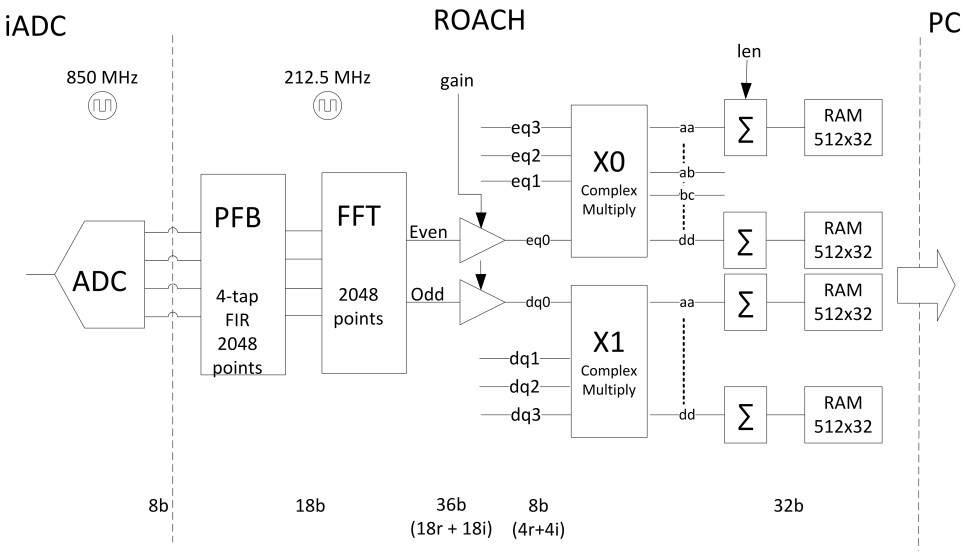

Figure 2.41: Block diagram of the ROACH ADC and correlator system.

the ethernet interface to the data collection computer, where they are saved to disk. A block diagram of the digital back end is shown in Figure 2.41.

2.6.1 ADC Performance

The AT84AD001B ADC is specified to have an effective number of bits (ENOB) of 6.8 at 500 MHz, and 6.2 at 1 GHz. The gain of the analog receiver is set to achieve an input voltage standard deviation of about 3.5 bits, which causes a negligible noise penalty due to quantization plus ADC noise, while allowing headroom for receiver linearity and ADC saturation caused by external radio frequency interference. This corresponds to an input power of approximately -20 dBm for a voltage reference of 0.5 V in a 50 Ω system. The added noise caused by quantization of a Gaussian distributed input signal is calculated in detail in [44].

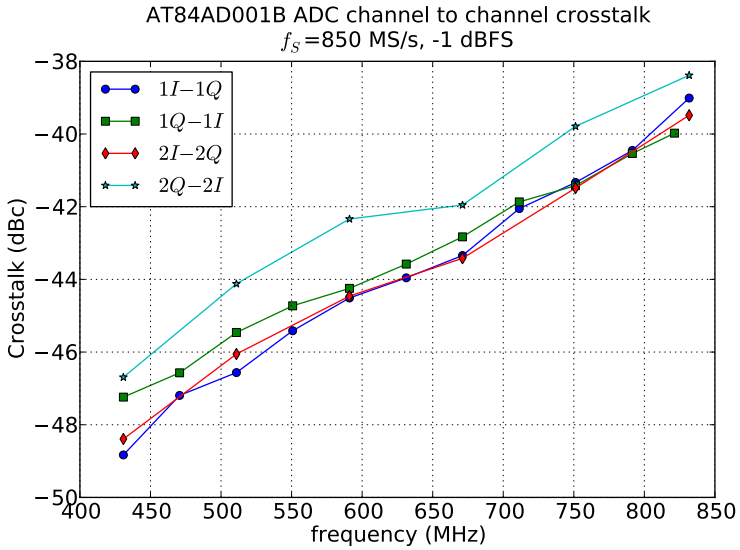

Figure 2.42: AT84AD001B ADC channel to channel crosstalk.

The crosstalk between channels on the same ADC chip, linearity, and input impedance were measured for the ADC on the input board with a 1 dB coaxial attenuator at the input, as it is used in the two dish system.

The crosstalk was measured by supplying a sinusoidal carrier input at 1 dB below full scale of the ADC reference (1 dBFS) to one ADC channel, collecting samples in both ADC channels I and Q, and comparing the power spectra. The crosstalk is specified in decibels to carrier (dBc). The results for each of the two ADC boards are shown in Figure 2.42.

The linearity of the ADC is characterized in three ways: total harmonic distortion (THD), spur free dynamic range (SFDR), and intermoduation distortion (IMD). THD measures the ratio of the power in a single tone of amplitude 1 dBFS to the sum of the power in the first nine harmon-

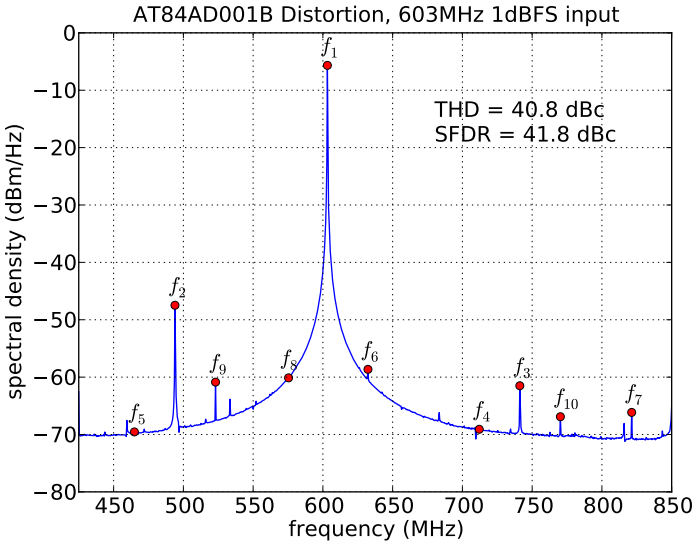

Figure 2.43: AT84AD001B ADC total harmonic distortion and spur free dynamic range. The fundamental (f_1) and the first nine harmonics (f_2-f_{10}) are labelled.

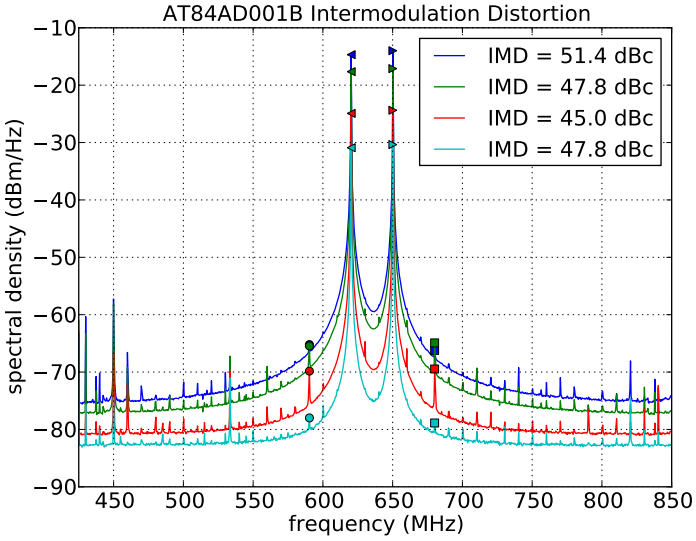

Figure 2.44: AT84AD001B ADC third order intermodulation distortion.

ics. SFDR is the ratio of the power in the fundamental to the power in the highest spur. IMD is measured by supplying the input with two single frequency equal amplitude sinusoidal tones, and measuring the ratio of the power in the main tones to the power in the highest third order intermodulation product. The results of the one and two tone tests are shown in Figure 2.43 and Figure 2.44. The spectra are folded into the 425-850 MHz band (f_s=850 MHz).

The second order distortion (second harmonic in the single tone test) dominates the overall non-linearity since the ADC does not have a well defined high frequency roll off. The non-linearity in the IMD test is dominated by harmonics of the main input tones rather than the third order intermodulation products, despite the intermodulations products being much nearer in frequency to the main tones. The third order IMD does not increase with increasing power in the main tones, suggesting that the non-linearity is primarily a result of the digitisation.

The input impedance of the two input channels I and Q on the ADC board were measured using the HP8753E VNA. The return loss is shown in Figure 2.45.

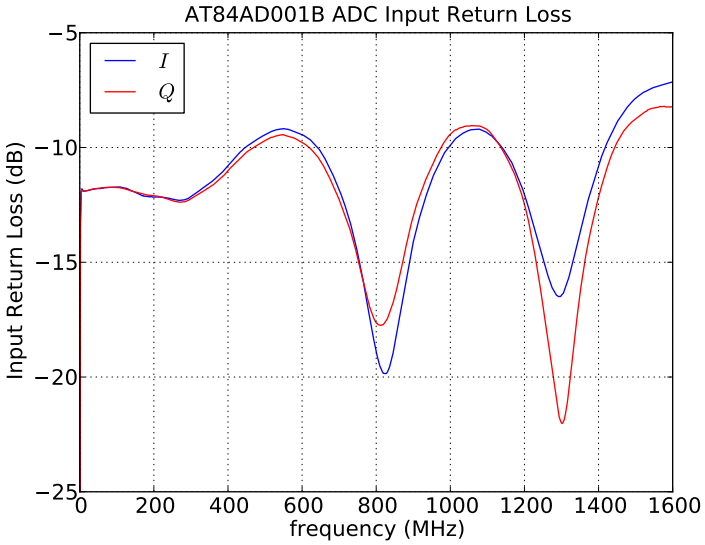

Figure 2.45: AT84AD001B ADC board input return loss with a 1 dB coaxial attenuator at the input.

Chapter 3

Characterization

The two dish system was fully constructed and instrumented in May 2011. The dishes were initially tilted to declination $\delta = 59°$, near to the brightest radio source in the sky, the supernova remnant Cassiopeia A (Cas A). Cas A is a useful calibration source because it is a well studied and characterized point source. The Cas A flux densities used here are calculated from the model provided in [45].

The two dish system collects data from all four channels (two dishes, two polarizations) simultaneously, facilitating analysis of the instrument both as an interferometer and as independent single dish classical radio telescopes. The interferometric results and associated crosstalk problems are presented in Section 3.1. The remaining sections in the chapter are devoted to instrument characterization using primarily single dish measurements; these results include receiver gain, frequency dependent beam on the sky, and system temperature.

3.1 Interferometry

3.1.1 Cassiopeia A Results

The two dishes lie on an east-west line, spaced 19 m apart. As the sky rotates, the wavefronts received at each dish move in and out of phase, so their cross correlation yields interference fringes. The fringe period T_{fringe} can be calculated as

$$T_{fringe} = \frac{1}{\omega_{\oplus} \cos \delta} \arctan \frac{c}{lf} \tag{3.1}$$

where $\omega_{\oplus}$ is the angular rotation speed of the earth, δ is the declination, c is the speed of light, l is the baseline spacing of the two dishes, and f is the frequency of the received signal. At 650 MHz and $\delta = 59°$, T_{fringe} is slightly more than ten minutes. A plot of the real and imaginary parts of the frequency domain cross correlation of a single polarization at 650 MHz while Cas A crosses through the beam is shown in Figure 3.1. The cross correlation is computed in the correlator in the frequency domain, as described in Section 2.6. The cross correlation should be centred around zero at all frequencies; in Figure 3.1 there is a positive offset.

Plots showing the fringes caused by Cas A in the full frequency band are shown in Figure 3.2. Figure 3.2 also yields some insight into the beam size as a function of frequency; the shrinking width of the fringes with increasing frequency indicates that the beam is narrowing. Detailed beam measurements are presented in Section 3.2.

The approximately 3.8 MHz striping in frequency present in Figure 3.2

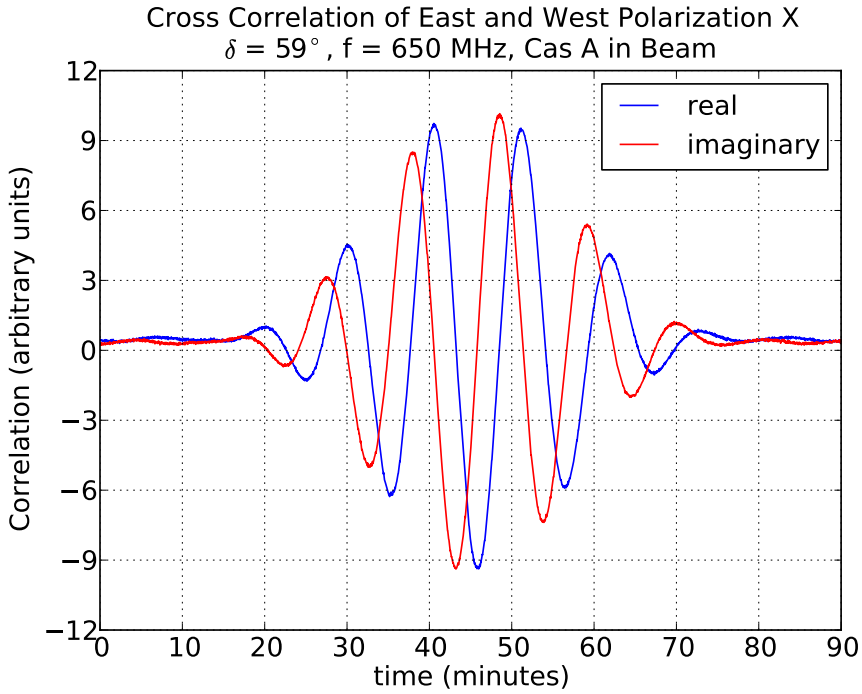

Figure 3.1: Cas A interference fringes at 650 MHz.

and the average offset in Figure 3.1 are further investigated using the spectra of cross correlations. A typical spectrum of the average cross correlation coefficient over several hours is shown in Figure 3.3. Averaging over a timescale much longer than the transit time of any source through the beam should result in correlation coefficients of zero in both the real and imaginary parts.

The correlation coefficient normalizes the power in the cross correlation of two signals to the power in the autocorrelation of each signal. At each frequency, the complex average correlation coefficient r_f is given by

$$\langle r_f \rangle_t = \frac{\langle A_f B_f^* \rangle_t}{\sqrt{\langle AA^* \rangle_t \ \langle B^* B \rangle_t}} \tag{3.2}$$

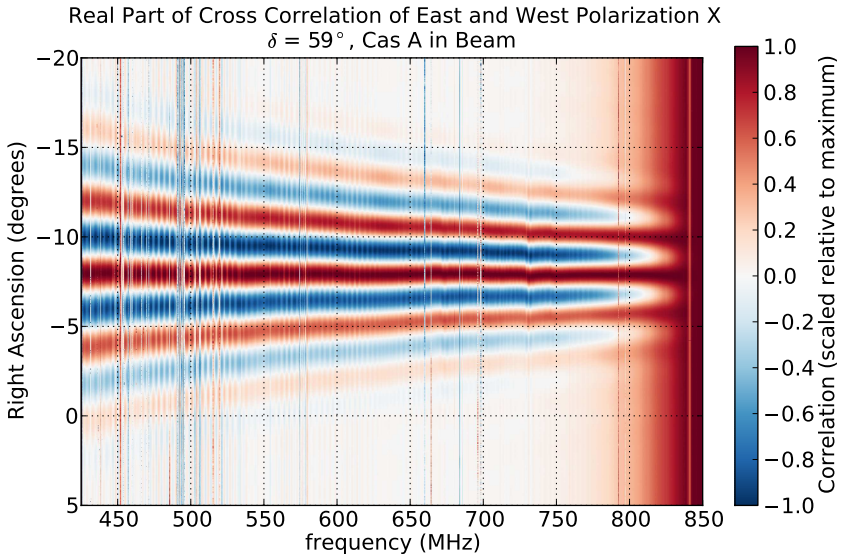

(a) Real part

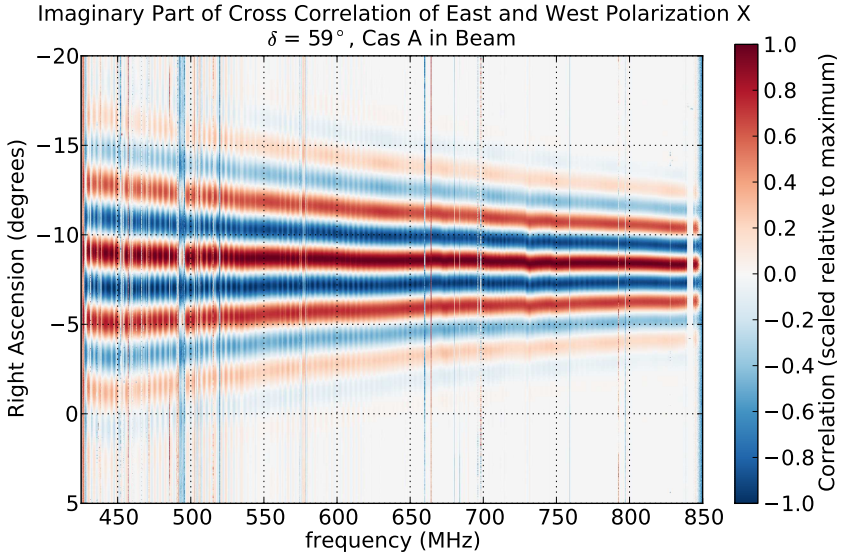

(b) Imaginary part

Figure 3.2: Cas A interference fringes.

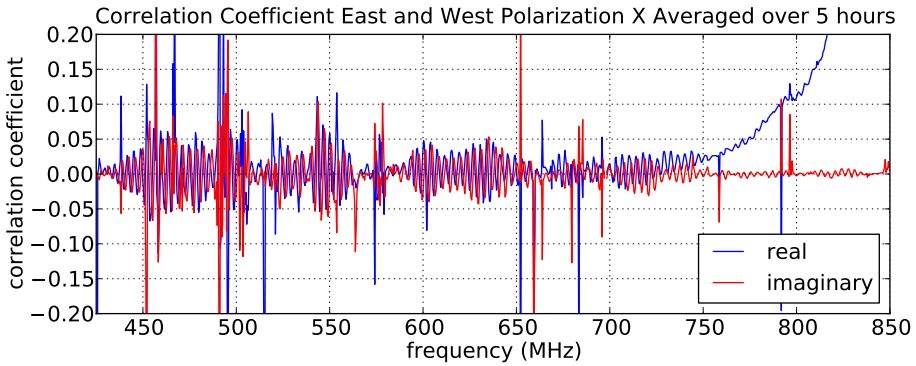

Figure 3.3: Cross correlation coefficients averaged over five hours.

where $\langle \cdots \rangle_t$ denotes the time average, the subscript f denotes frequency, and A, A^*, B, and B^* are frequency domain signals and their complex conjugates.

The approximately 3.8 MHz ripple apparent in Figure 3.3 demonstrates that both the striping in Figure 3.2 and the baseline offset in Figure 3.1 are symptoms of the same problem: a constant in time, periodic in frequency baseline shape. The large sharp spikes in frequency are a result of RFI.

In the real part of the cross correlations, the correlation coefficient rises to nearly 1 at high frequencies. This phenomenon occurs in all six cross correlations, at all times. It is a so far unexplained effect of the digital correlator. Short snapshots of raw ADC samples from all four channels were collected synchronously with the normal ROACH correlator data output and stored directly to disk. The raw ADC samples were later analysed using full precision operations on a PC. By breaking the ADC samples into 2048 point windows, taking the Fourier transform of each window, and computing the cross correlation in the frequency domain, the results can be directly

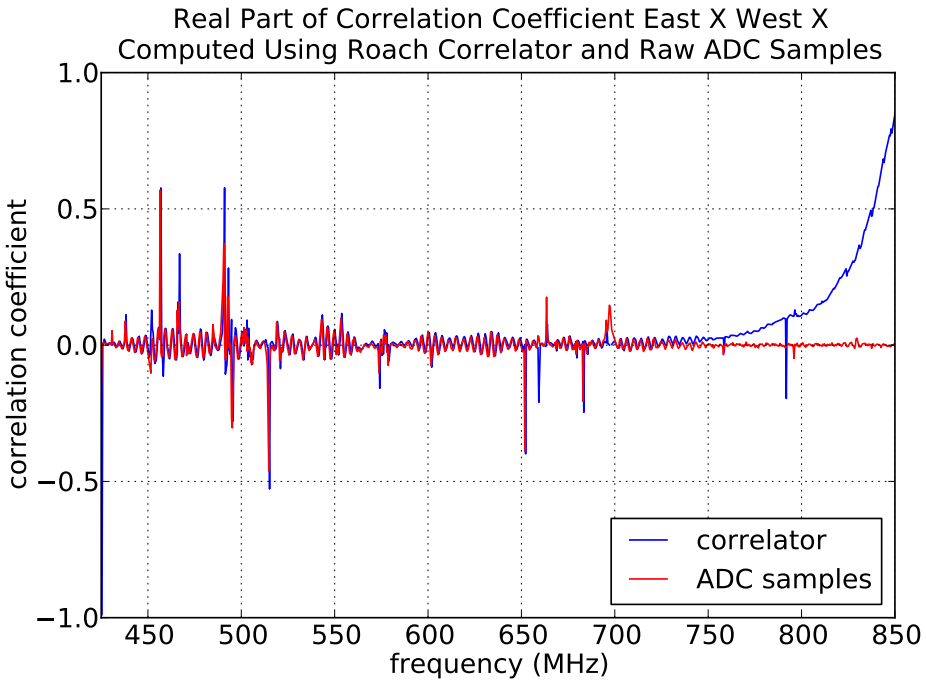

Figure 3.4: The real part of cross correlation coefficients using the ROACH correlator and snapshots of raw ADC samples processed with full precision on a PC.

compared to the equivalent quantities computed in real time by the ROACH correlator. The comparison is shown in Figure 3.4.

3.1.2 Crosstalk

Periodic ripple in the frequency domain of correlation products corresponds directly to a spike in the time domain correlation function. The inverse Fourier transform of the frequency domain cross correlation yields the time domain correlation function, shown in Figure 3.5 for the east and west X polarized product. There is a spike at an approximate delay time of

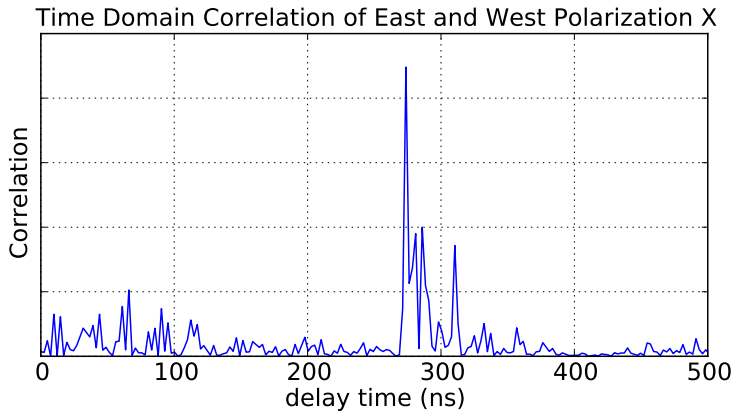

Figure 3.5: Time domain cross correlation function of the X polarized signals from the east and west dishes.

280 ns. Since the two signals should be on average uncorrelated, this suggests crosstalk between channels with a delay time of 280 ns.

The output of a given channel is made up of the signal from that channel combined with a delayed version of the signal from another channel. Calling the two channels A and B, the measured outputs A' and B' can be written as

$$A'(t) = A(t) + \alpha A(t + dt_\alpha) + \beta B(t + dt_\beta) \tag{3.3a}$$

$$B'(t) = B(t) + \gamma B(t + dt_\gamma) + \delta A(t + dt_\delta) \tag{3.3b}$$

where α, β, γ and δ are unitless crosstalk coefficients, and $dt_{\alpha\ldots\gamma}$ are the corresponding crosstalk delay times. Keeping only the terms with first order crosstalk coefficients and setting all delay times equal to dt, the calculated

cross correlation AB^* is given by

$$A'B'^* = AB^* + \gamma AB^*_{dt} + \delta AA^*_{dt} + \alpha A_{dt}B^* + \beta B_{dt}B^* \tag{3.4}$$

Converting to the frequency (k) domain using Fourier series representations of A and B given by

$$\tilde{A} = \sum_t a_t e^{-ikt} \tag{3.5a}$$

$$\tilde{B} = \sum_t b_t e^{-ikt} \tag{3.5b}$$

$$\tilde{A}_{dt} = \sum_t a_t e^{-ikt} e^{ikdt} \tag{3.5c}$$

$$\tilde{B}_{dt} = \sum_t b_t e^{-ikt} e^{ikdt} \tag{3.5d}$$

leads to the frequency domain cross correlation

$$\tilde{A}'\tilde{B}'^* = \sum_{t,t'} \left[a_t b_t^* (1 + \gamma e^{-ikdt} + \alpha e^{ikdt}) + \delta |a_t|^2 e^{-ikdt} + \beta |b_t|^2 e^{ikdt} \right] e^{ik(t-t')} \tag{3.6}$$

The coefficients a_t and b_t are uncorrelated, so $a_t b_t^*$ is zero, leaving

$$\tilde{A}'\tilde{B}'^* = \sum_{t,t'} \left[\delta |a_t|^2 e^{-ikdt} + \beta |b_t|^2 e^{ikdt} \right] e^{-ik(t-t')} \tag{3.7}$$

Assuming $\delta |a_t|^2$ is approximately equal to $\beta |b_t|^2$, the term in the sum is proportional to $\cos(k\ dt)$, reproducing the sinusoidal oscillation in the frequency domain seen in the data.

A second manifestation of this crosstalk should be visible in the autocor-

relations. Assuming the crosstalk coefficients α and β are equal, and taking only the terms that are first order in crosstalk coefficient, the measured autocorrelation for channel A can be written approximately as

$$A'A'^{*} = AA^{*} + 2\alpha AB^{*}_{dt} + 2\alpha AA^{*}_{dt} \tag{3.8}$$

The measured autocorrelation contains the cross correlation of A with a delayed version of B superimposed on the true autocorrelation. This effect is observed in the autocorrelations of many frequencies when Cas A crosses the beam. An example is shown in Figure 3.6.

The delay in the crosstalk term can also be extracted from the autocorrelations. At different frequencies, a fixed delay time corresponds to a different phase. Thus, the time at which the cross correlation AB^{*}_{dt} peaks is a linear function of frequency; that is, the crosstalk fringes in the measured autocorrelation change phase with frequency. Since the delayed cross correlation term is directly superimposed on the measured autocorrelation, the time at which Cas A appears the brightest is modulated by the fringe phase, as seen in Figure 3.7. A plot of the time at which Cas A appears brightest across the frequency band is shown in Figure 3.8. The period of the sawtooth wave matches the period of the sinusoidal ripple in the cross correlations: about 3.8 MHz. This implies that in the crosstalk model of Equation 3.3, the cross channel delay times dt_β and dt_δ are the same as the in channel delay times dt_α and dt_γ: about 280 ns.

The crosstalk signal originates at the end of the receiver after full amplification, and radiates back to the antennas. Signals propagate from the

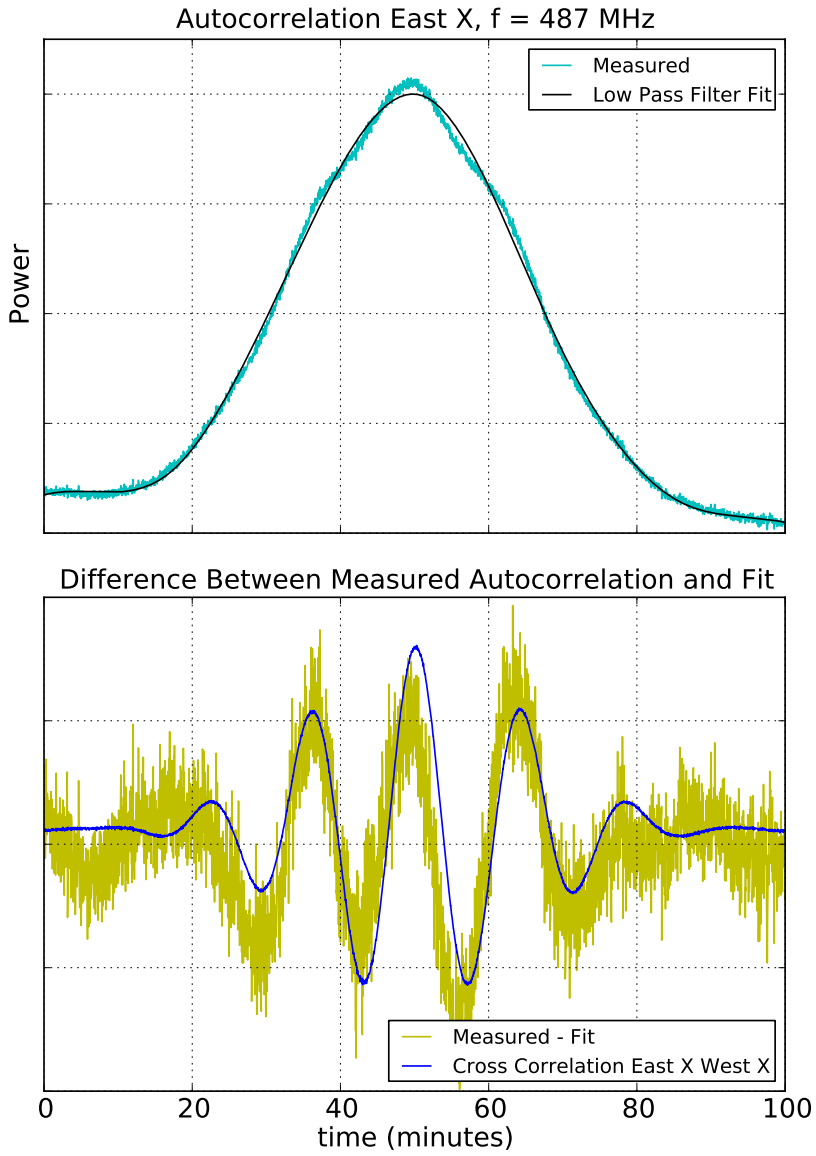

Figure 3.6: Top: The measured autocorrelation of the X polarized signal from the east dish at 487 MHz along with a low pass filtered fit to the data while Cas A crosses through the beam. Bottom: The difference between the fit and the data. The cross correlation of the east and west X polarized signals is scaled and superimposed on top of the difference.

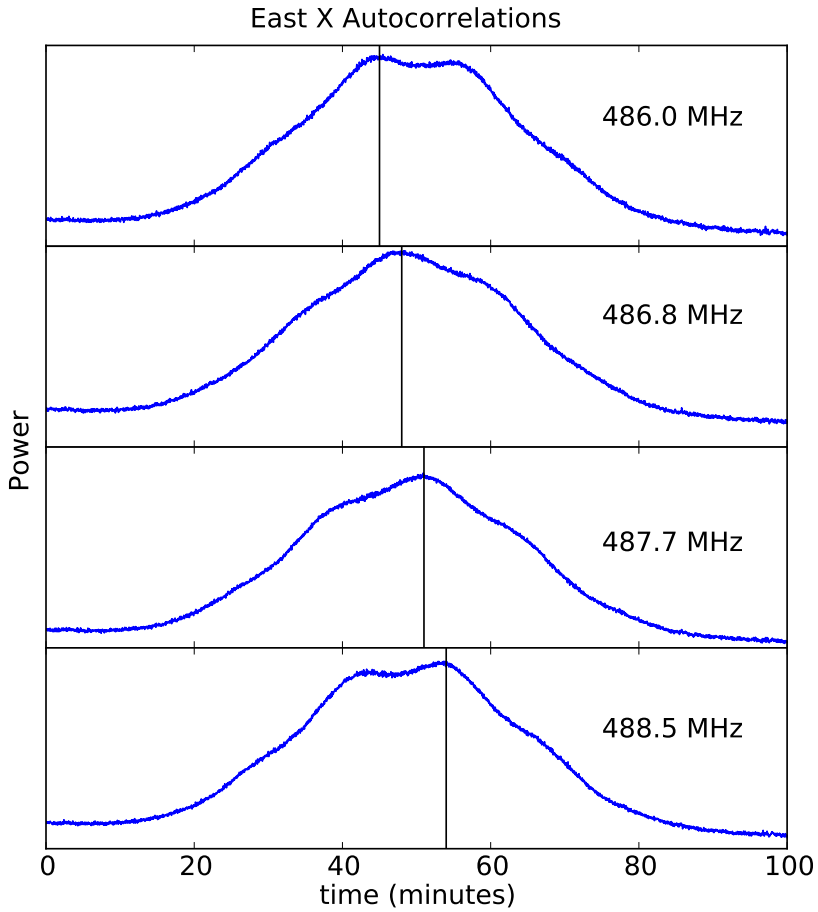

Figure 3.7: Measured autocorrelations from the east dish X polarization at different frequencies while Cas A passes through the beam. The east X west X cross correlation fringes present in the autocorrelation change phase with frequency because of the delayed nature of the crosstalk.

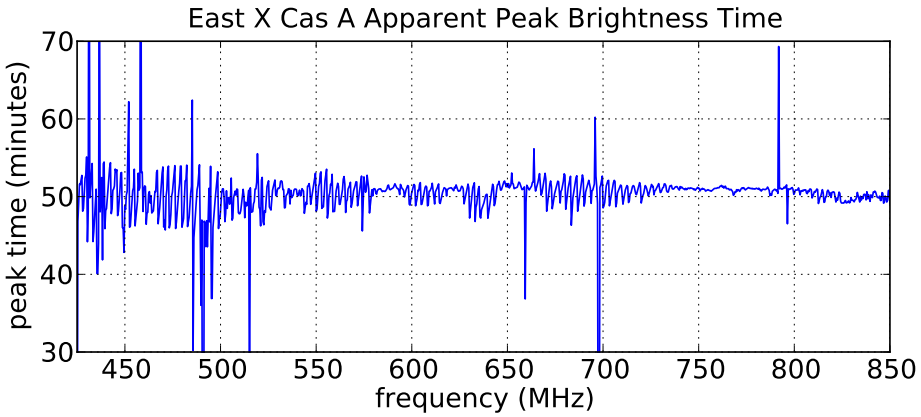

Figure 3.8: Peak brightness time vs. frequency in the autocorrelation of the X polarized signal from the east dish while Cas A crosses the beam.

antenna through the amplifiers at the focus and the 50 m underground cables to the trailer containing the correlator, where they are amplified further and digitized. The LMR-400 coaxial cables have a propagation velocity 85% of the speed of light in a vacuum, which corresponds to a transit time of roughly 200 ns over 50 m. The remaining 80 ns of the 280 ns total delay time arises from the roughly 25 m free space path from the correlator back to the antennas.

The signals radiate from the power supply leads of the last stage amplifiers, the type N connectors that bring the signals inside the shielding box containing the correlator electronics, and the 120 V AC power entry and fibre waveguide on the correlator shielding box. The RF power leaking from the amplifier power supply lines can be reduced by the addition of high attenuation feed through filters to seal the RF power inside the ampli-

fier boxes. A full shielded room to house the correlator and final amplifiers would improve overall isolation of the amplified signals from the antennas. Both solutions are part of the near term plans for improving the two dish system.

In order to continue characterizing the two dish system without the complications arising from crosstalk between signals, data are collected using each dish individually. The remainder of this chapter is dedicated to the analysis of single dish results obtained with data collected while the second dish is either powered off, or the LNA disconnected from the feed and terminated with 50 ohms.

3.2 Beam

The beam pattern of each dish was measured using Cassiopeia A.

3.2.1 One Dimensional Full Width Half Maximum

The full width half maximum (FWHM) of the beam in the east-west dimension is measured for each polarization by pointing the dish to declination $\delta = 59°$ and observing Cas A transit overhead. This is done for both the east and west dishes independently by fitting a smooth curve to the autocorrelation of each channel, finding a baseline value on either side of Cas A in the galactic plane, and measuring the full width half maximum in time referenced to the baseline. An example fit is shown in Figure 3.9. The FWHM time is converted to angle using the rotation speed of the sky.

The FWHM of both polarizations and both dishes with the isolating

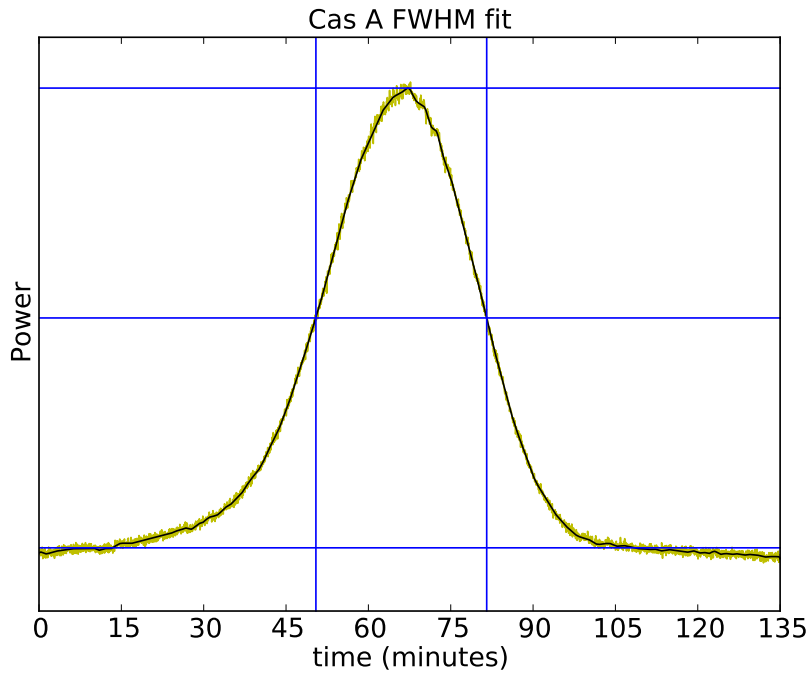

Figure 3.9: An example of the measurement of the east west beam FWHM using Cas A.

cylinders fixed to the ground plane (see Figure 2.3) are shown in Figure 3.10.

A comparison of the results with and without the isolating cylinders on the ground plane is shown in Figure 3.11 for the east dish. The cylinders partially symmetrize and slightly widen the beam on the sky. The wider beam confirms the expected effect — the cylinders narrow the illumination pattern of the feed itself, resulting in a reduction in effective area of the full antenna, and a wider beam on the sky.

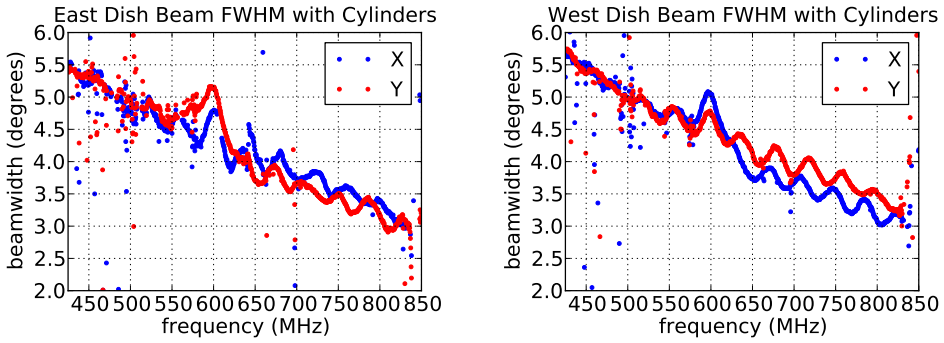

(a) East dish

(b) West dish

Figure 3.10: Beam FWHM with isolation cylinders on the ground plane.

3.2.2 Baseline Ripple

Both with and without the isolation cylinders on the ground plane, there is a periodic ripple across the frequency band in the beam FWHM. The period of the ripple is approximately 41 MHz. This baseline spectral ripple is a result of standing waves between the reflector and the ground plane. The distance from the ground plane to the centre of the reflector is 3.67 m on each dish, so a reflected wave travels 7.34 m there and back before arriving at the feed again. A wave travelling at the speed of light requires 24.5 ns to cover 7.34 m, corresponding to a frequency of 40.9 MHz.

The phenomenon of baseline ripple is well established in the literature [46–49]. One method of minimizing baseline ripple is to add a scatterer at the centre of the reflector in the shadow of the ground plane.

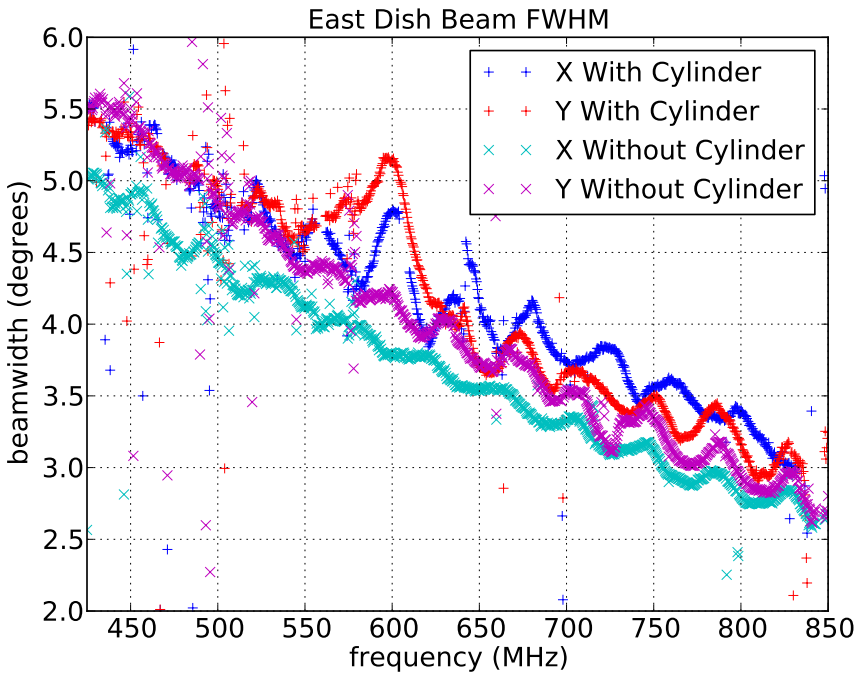

Figure 3.11: The beam FWHM for each polarization on the east dish with and without the isolation cylinders on the ground plane.

3.2.3 Two Dimensional Gaussian

A second measurement of the beam was made using data collected at several declinations around Cas A. Each day, the dish was tilted approximately 1°, from 3° north of zenith ($\delta = 52°$) to 24° north of zenith ($\delta = 73°$). These data were filtered and thermally adjusted (see Section 3.3.1), binned into equal area pixels of right ascension and declination, and transformed to a rectangular coordinate system using the Gnomonic projection.

The Gnomonic projection converts right ascension α and declination δ into Cartesian coordinates x and y by projecting each point on the surface

of the sphere on to a plane tangent to the projection point, in this case the location of Cas A. The transformation from α, δ to x, y around the point α_0, δ_0 is given by:

$$x = \frac{\cos\delta \sin(\alpha - \alpha_0)}{\sin\delta \sin\delta_0 + \cos\delta \cos\delta_0 \cos(\alpha - \alpha_0)} \tag{3.9a}$$

$$y = \frac{\cos\delta \sin\delta_0 - \cos\delta \sin\delta_0 \cos(\alpha - \alpha_0)}{\sin\delta \sin\delta_0 + \cos\delta \cos\delta_0 \cos(\alpha - \alpha_0)} \tag{3.9b}$$

A section of data approximately 25° wide in right ascension and 15° wide in declination was projected into the plane tangent to the location of Cas A. The resulting data in rectangular coordinates were fit to a two dimensional Gaussian to approximate the beam shape. The fit yields the Gaussian amplitude, offset, centre coordinates x_c and y_c, semi-major and semi-minor 1σ widths, and orientation. An example of one such fit is shown in Figure 3.12.

The two dimensional Gaussian parameters of the east dish beam for the full frequency band are shown in Figure 3.13. The measured right ascension and declination of Cas A can be compared to the actual values to estimate the pointing error of the dish. The high noise level in the beam orientation angle plot is not surprising since the beam is nearly circular.

Using the beam parameters, the effective area A_e of the antenna can be calculated as [14]

$$A_e = \frac{G(\theta, \phi)\lambda^2}{4\pi} \tag{3.10}$$

where $G(\theta, \phi)$ is the antenna gain as a function of the altitude θ and azimuth ϕ, and λ is the wavelength. The gain of the antenna at boresight for a two

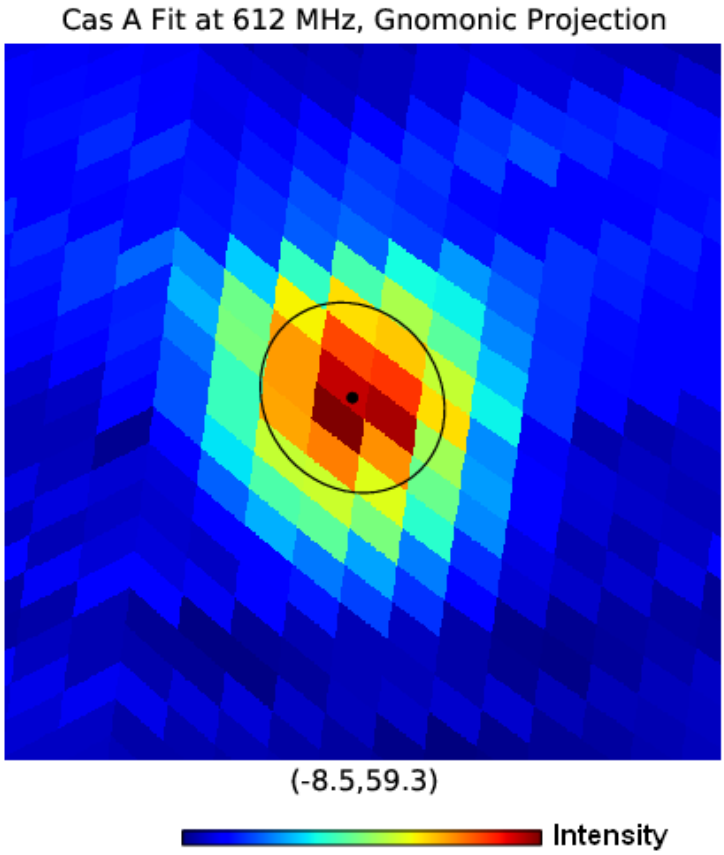

Figure 3.12: An example of a 2D Gaussian fit to Cas A using the Gnomonic projection around $\alpha = 8.5°$, $\delta = 59.3°$, the apparent location of Cas A for the telescope. The black dot indicates the centroid of the fit, and the ellipse shows a cross section of the 2D Gaussian fit to the data at 1.5σ width. The colour scale indicates the received power at each pixel corresponding to a different location in the tangent plane.

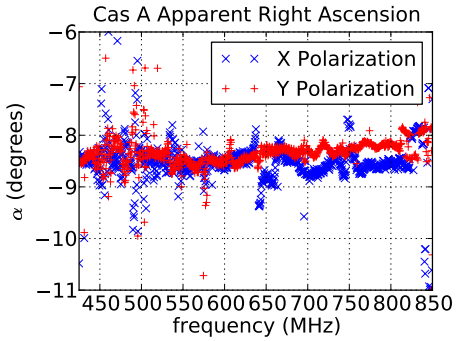

(a) Cas A apparent right ascension

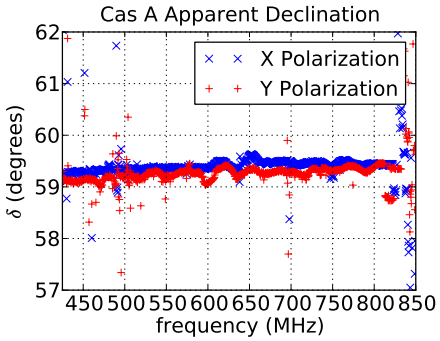

(b) Cas A apparent declination

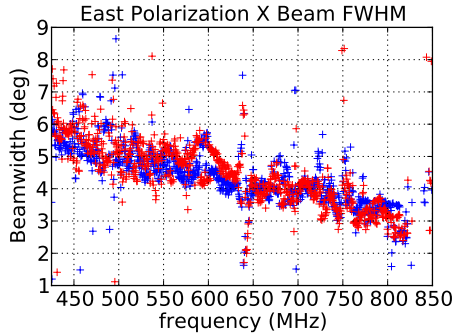

(c) X polarization full width half maxima, semi-major and semi-minor axes

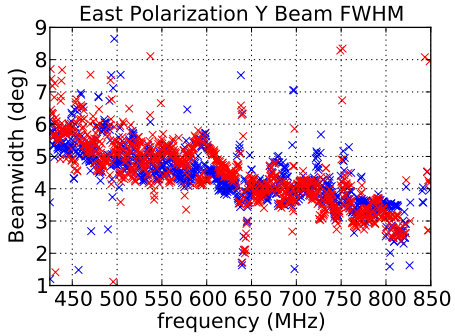

(d) Y polarization full width half maxima, semi-major and semi-minor axes

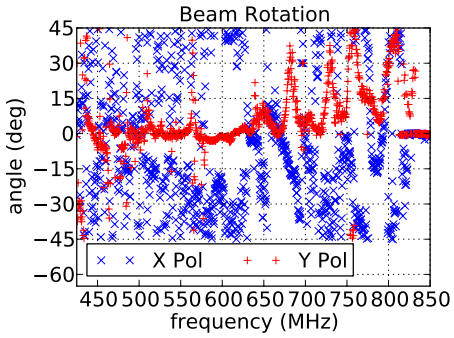

(e) Beam orientation angle

Figure 3.13: Two dimensional Gaussian beam fit parameters.

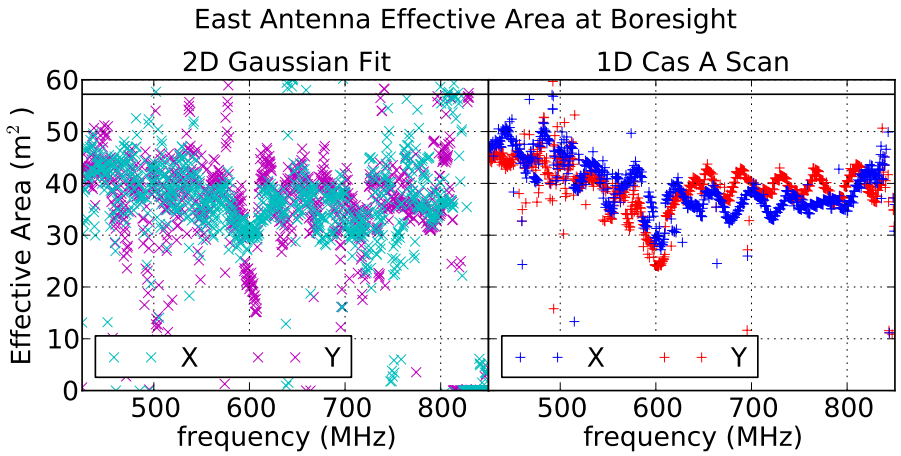

Figure 3.14: The effective area of the antenna at boresight, measured using the full two dimensional Gaussian beam parameters and using single declination scans of Cas A assuming a circular beam. The physical area of the reflector is 57.2 m^2, shown as a solid black line.

dimensional Gaussian beam is given by

$$G(\theta = 0, \phi = 0) = \frac{2 \text{ sr}}{\sigma_x \sigma_y} \tag{3.11}$$

where σ_x and σ_y are the semi-major and semi-minor standard deviations of the Gaussian beam. A plot of the effective area at boresight is shown in Figure 3.14 using the full two dimensional beam map, and using the Cas A east-west FWHM measured at a single declination assuming a circular beam.

3.3 Gain Calibration

The overall gain of the system converts an input power at the antenna to a measured output power in correlator units. This gain depends on

several elements: the coupling of the feed to the free space waves arriving at the focus; the coupling of the LNA to the feed; the gain and matching of the analog receiver chain, including the LNA, second stage amplifiers and filter, cable loss, and in line attenuators; the ADC response; and the digital correlator Fourier transform gain.

The total gain, quantified in output correlator units per input Kelvin, varies with time, frequency, temperature, and channel. Complete gain calibration requires full understanding of the variations to properly remove their effects from the data. The gain variation is modelled using a thermal model for each frequency of each channel. After removing temperature fluctuations, the gain is converted to an absolute value using the flux density of Cas A and the measured beam from Section 3.2.

3.3.1 Thermal Gain Model

The receiver properties change with temperature due to the passive components in the matching and bias circuitry, as well as the temperature dependence of the GaAs FET. The transistor temperature dependence includes changes in threshold voltage, energy barriers, and electron velocity and mobility [50].

The overall temperature dependence of the system is modelled as purely gain variation resulting from temperature fluctuations in two places: at the focus, and inside the trailer containing the last stage amplifiers, ADC and correlator. With the input to the LNA resistively terminated, the input

power P_{in} in a given bandwidth Δf is described by

$$P_{in} = k\Delta f \ (T_f + n(T_f)) \tag{3.12}$$

where k is Boltzmann's constant, T_f is the physical temperature at the focus of the dish, and therefore the temperature of the termination at the LNA input, and n is the noise temperature of the LNA, which may be a function of the physical temperature T_f. The output power P_{out} at the ADC is

$$P_{out} = G_f(T_f)\ G_t(T_t)\ P_{in} = G_f\ G_t\ k\Delta f\ (T_f + n) \tag{3.13}$$

where G_f is the gain of the amplifiers at the focus and G_t is the gain of the amplifiers inside the trailer. For the amplifiers at the focus and in the trailer, the thermal dependence of the gain G can be Taylor expanded around T_0:

$$G(T) = G(T_0) \ + \ \left.\frac{\partial G}{\partial T}\right|_{T_0} (T - T_0) \ + \ \frac{1}{2}\left.\frac{\partial^2 G}{\partial T^2}\right|_{T_0} (T - T_0)^2 \ + \ \cdots \tag{3.14}$$

Taking only the first order terms, this can be simplified to

$$G(T) \approx G(T_0) + G'\Delta T \tag{3.15}$$

where

$$G' = \left.\frac{\partial G}{\partial T}\right|_{T_0} \quad \text{and} \quad \Delta T = T - T_0$$

Ignoring the temperature dependence of the noise and setting $n = n_0$, the

output power can be written as

$$P_{out} \approx kB\ (G_{0f} + G'_f\ \Delta T_f)\ (G_{0t} + G'_t\ \Delta T_t)\ (T_f + n_0)$$
$$= g_0\ (1 + g'_f\ \Delta T_f)\ (1 + g'_t\ \Delta T_t)\ (T_f + n_0) \quad (3.16)$$

where the three thermal parameters in the model are

$$g_0 = k\Delta f\ G_{0f}\ G_{0t}\ ; \quad g'_f = \frac{G'_f}{G_{0f}}\ ; \quad g'_t = \frac{G'_t}{G_{0t}} \quad (3.17)$$

The temperatures at the focus and inside the trailer are monitored using thermistors glued to the outside of the amplifier boxes. Replacing the feed with a 50 Ω termination at the input to the LNA on all four channels, the thermal parameters are estimated by fitting the power in the autocorrelations to the thermal model at each frequency.

Data were collected with terminated inputs for approximately 35 days. The temperature at the focus of the east dish and in the trailer during this time are shown in Figure 3.15.

The temperatures are measured outside the amplifier shielding boxes, but the temperature of interest is on the circuit inside the box. There is some thermal delay between the thermistor temperature outside the box and the temperature of the circuit inside the box. The delay is particularly important inside the trailer, where a thermostat implements temperature control that leads to fast changing temperatures that are heavily damped by the aluminum boxes. A simple low pass filter implemented with a boxcar average adjusts for the difference between the measured temperatures and

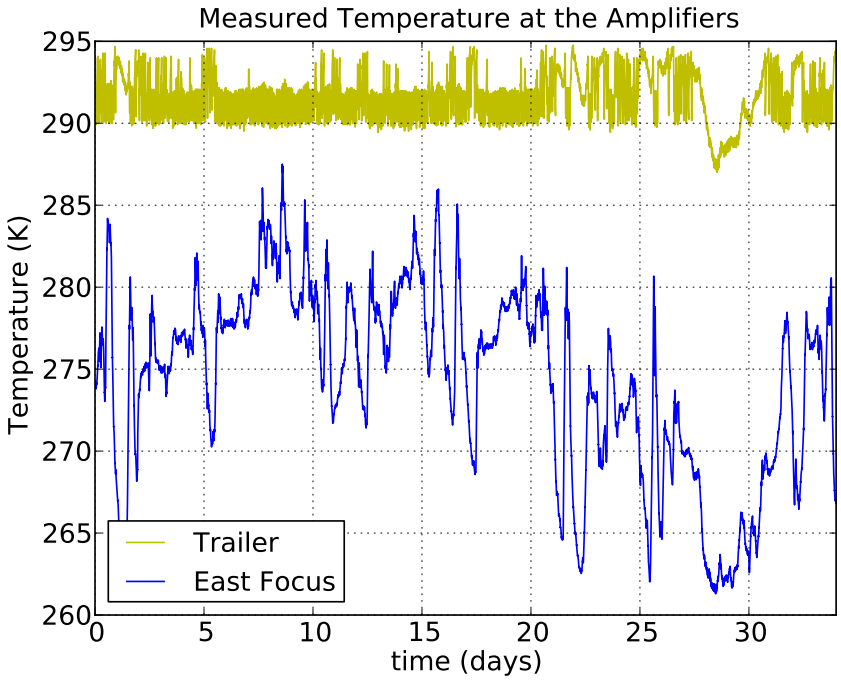

Figure 3.15: Thermistor measured temperatures at the focus of the east dish and inside the trailer. The thermistors are attached to the outside of the metal shielding boxes enclosing the amplifiers.

the circuit temperatures. The number of samples in the boxcar average was adjusted to achieve the best possible fit to the data, resulting in a time constant of approximately 27 minutes. An example of the effect of the filter on the raw temperature measurements inside the trailer is shown in Figure 3.16.

The data collected over 35 days with terminated inputs were fit to the thermal model using a non-linear least squares simplex minimization routine. The centre temperature T_0 is 290 K. An example of the fit for the X polarized channel on the east dish is shown in Figure 3.17. Although the fit produces

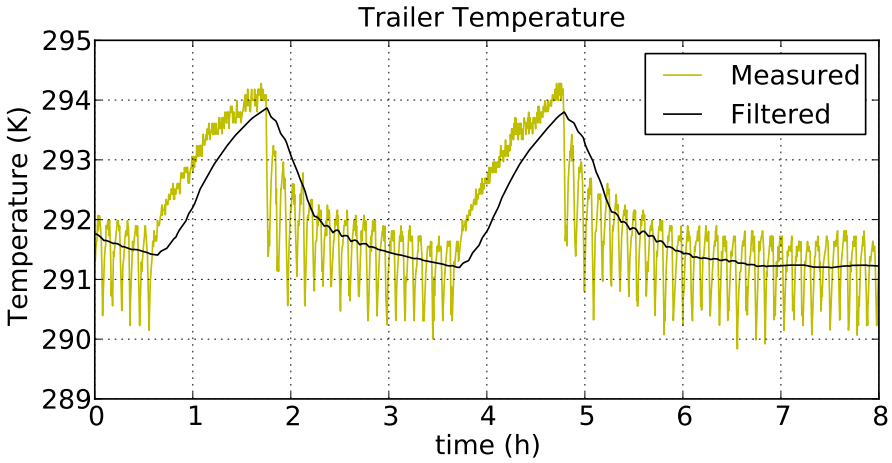

Figure 3.16: The temperature of the amplifier circuit inside the box is estimated by filtering the temperature measured on the outside of the box. The roughly 7 minute oscillations in trailer temperature caused by the switching of the baseboard heater are largely damped out, and the rise and fall times over longer scales are delayed to better fit the data.

output power far closer to the measured power than a constant gain model, it is insufficient for explaining all of the output power variation, as seen by the high χ^2 per degree of freedom. The error σ used in the least squares fit is the standard deviation of each data point, estimated by $\sigma = \sqrt{n}$, where n is the number of samples averaged inside the correlator to generate each data point.

The residual difference between the fit and the data for two channels is shown in Figure 3.18, normalized to the overall average of the full data set. The residuals of the four channels are significantly correlated. This non-thermal common mode variation suggests that the use of an always terminated dark channel may be useful for resolving further gain variation

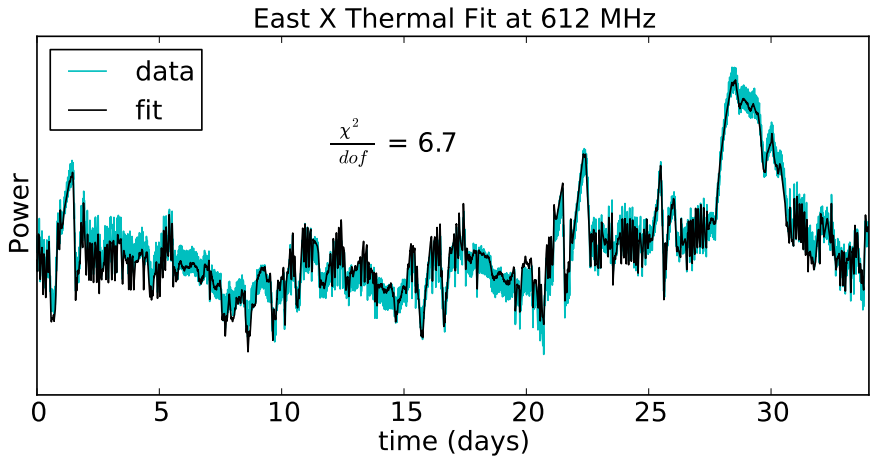

Figure 3.17: Autocorrelation data from the east dish X polarization with the LNA terminated with 50 Ω fit to the thermal model.

not captured by the temperature model.

The full spectra of the gain coefficients g'_f and g'_t for the east polarization X channel are shown in Figure 3.19.

3.3.2 Absolute Gain Value

After removing most of the gain fluctuations using the thermal model, the absolute value of the gain must be fit to the remaining approximately constant gain. With the knowledge of the beam described in Section 3.2, a single well known point source can provide a calibration reference. Using the flux density and spectral index of Cas A, the gain at each frequency for each channel is established in correlator units per Kelvin.

The antenna temperature of Cas A in centre of the telescope beam is

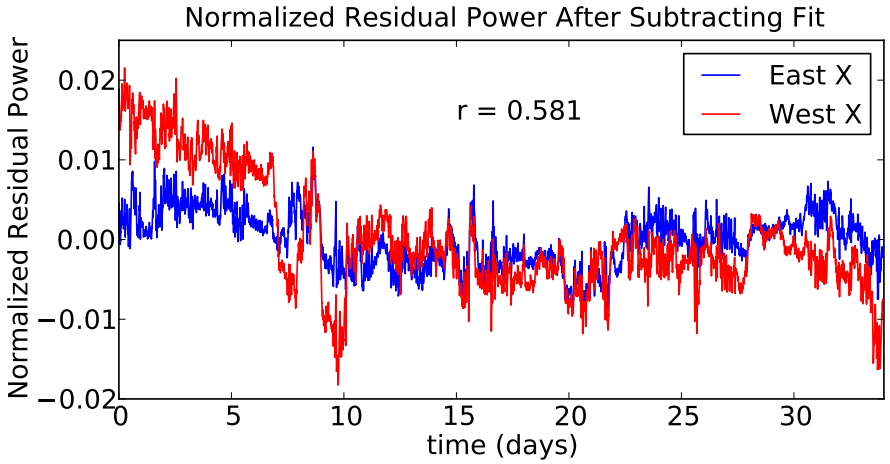

Figure 3.18: The difference between the data and the thermal fit for the east and west X polarization channels normalized to the overall average of each channel, binned into two minute sections. The Pearson correlation coefficient between the channels before binning the data is $r = 0.581$.

calculated as

$$T_a = \frac{1}{2}\frac{A_e \; S \; 10^{-26}}{k} \tag{3.18}$$

where the effective area A_e is given by Equation 3.10 and Equation 3.11, and the factor of $1/2$ accounts for the fact that a linearly polarized antenna collects only half of the available power from the source [44]. The antenna temperature of Cas A in the telescope beam is shown in Figure 3.20, using flux density calculated as [45]:

$$S_{CasA} = (f \text{ [GHz]})^{-0.77} \; (2723 \pm 54) \; \times \frac{1}{100} \times \\ [\; (0.97 \pm 0.04) - (0.3 \pm 0.04) \log (f \text{ [GHz]}) \;]^{year - 1980} \text{ Jy} \tag{3.19}$$

The error in the flux density from 400 to 900 MHz for the year 2012 is

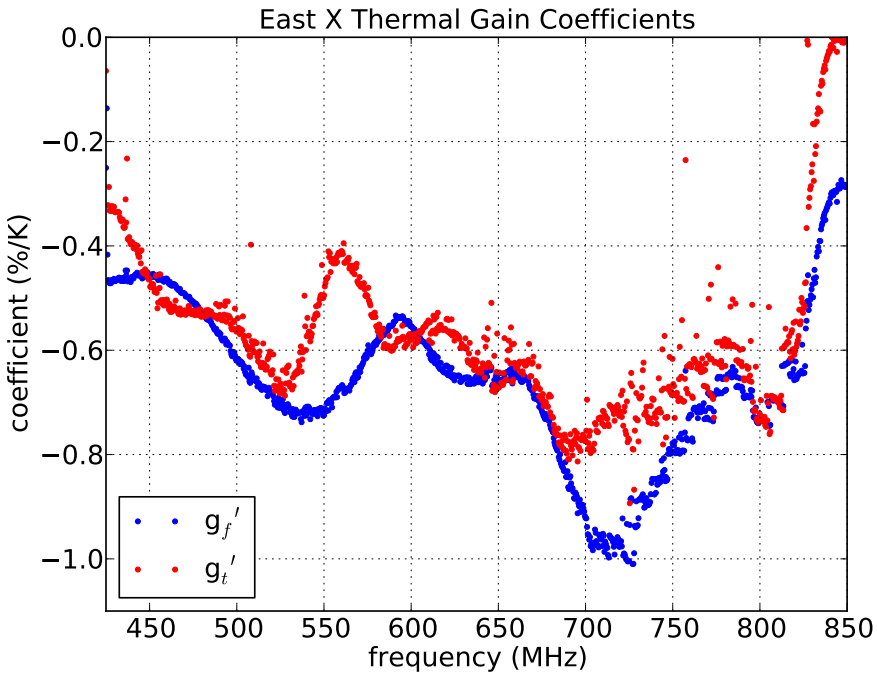

Figure 3.19: The best fit thermal gain coefficients of the east dish amplifiers at the focus, g'_f, and in the trailer, g'_t.

approximately 2.4%.

To compute the gain of the system in output correlator units per input Kelvin, the amplitude of Cas A in output correlator units is required as well as the antenna temperature. This can be estimated from the amplitude parameter of the two dimensional Gaussian beam fit described in Section 3.2.3, or using the one dimensional east west Cas A scans, as shown in Figure 3.9. The calibrated gain using each method is shown in Figure 3.21. In both cases, the error in the gain is dominated by gain fluctuations that are not removed by the thermal model.

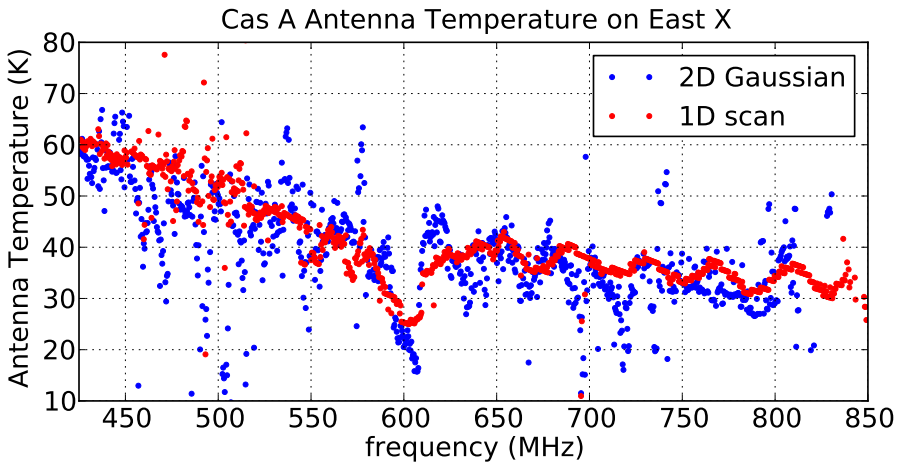

Figure 3.20: The antenna temperature of Cas A in the telescope beam. The 41 MHz baseline ripple described in Section 3.2.2 is evident.

3.4 System Temperature

The system temperature T_{sys} of a radio telescope describes the total noise power received. There are various contributions to the system temperature, including the sky brightness, atmospheric emission, radiation received by the feed from outside the reflector (spillover), and the noise of the receiver itself. In this thesis, the system temperature refers only to the portion of the total noise power that does not depend on the sky location; that is, the sky brightness temperature is not included. All of the data used in the system temperature calculations have been partially filtered for RFI and thermally adjusted as described in Section 3.3.1.

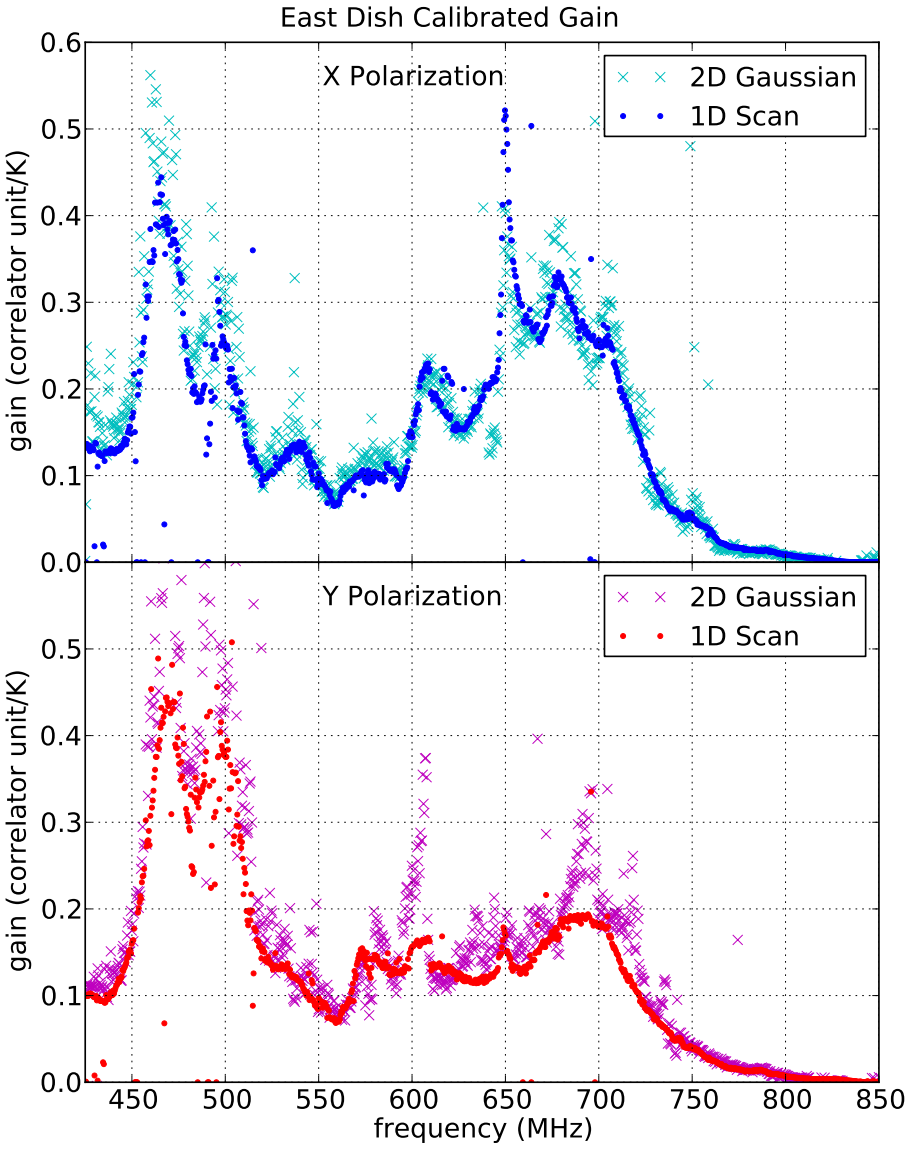

Figure 3.21: The calibrated gain of the full system in output correlator units per input Kelvin at the antenna. The gain is calculated by converting the flux density of Cas A to an input antenna temperature and comparing it to the change in received power while Cas A transits through the beam.

3.4.1 Measuring T_{sys}

The system temperature is measured with two methods: using Cas A as a calibration source, and comparing a sky model to the collected data.

The gain calibration described in Section 3.3.2 uses the flux density of Cas A to convert the measured autocorrelations from output correlator units to input power in Kelvin. This input power is the system temperature plus the sky brightness. The system temperature at the edge of Cas A in the galactic plane, shown in Figure 3.22, is

$$T_{sys} + T_{gal} = \frac{P_{out,\ CasA\ peak}}{g} - T_{ant,\ CasA} \tag{3.20}$$

where g is the gain in correlator units per Kelvin from Figure 3.21, $P_{out,\ CasA\ peak}$ is the measured autocorrelation in correlator units at the peak of Cas A, T_{gal} is the brightness temperature of the galaxy at the edge of Cas A, and $T_{ant,\ CasA}$ is the antenna temperature at the peak of Cas A from Figure 3.20. The 41 MHz baseline ripple (Section 3.2.2) forms a significant part of the variation in system temperature across the band.

The method of calculating T_{sys} using exclusively the amplitude of Cas A requires full knowledge of the beam shape, pointing, and Cas A flux density. It is also difficult to separate the galaxy brightness temperature from the system temperature.

An alternative method is to linearly fit a model of the sky to the data, resulting in a slope and offset, which together yield the system temperature

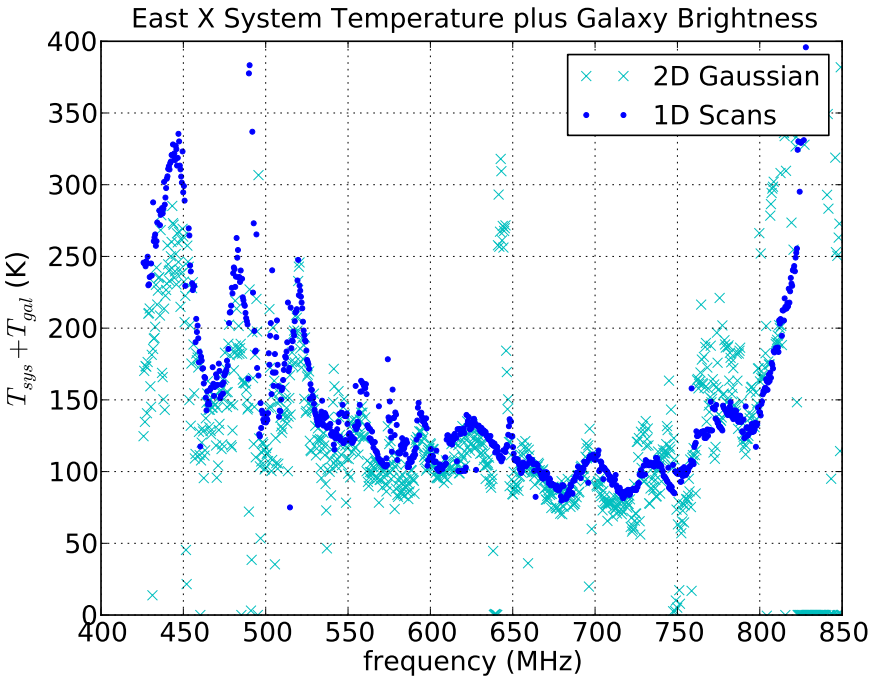

Figure 3.22: The system temperature measured using the amplitude of Cas A, plus the baseline brightness of the galactic plane around Cas A.

directly.

$$P_{out}(\alpha, \delta = 59^\circ) = m\ T_{sky}(\alpha, \delta = 59^\circ) + b \tag{3.21}$$

$$T_{sys} = \frac{b}{m} \tag{3.22}$$

where P_{out} is the measured autocorrelation in correlator units, T_{sky} is the model sky brightness temperature, and m and b are the slope and offset of the linear fit. To reduce the dependence of the result on the estimated beam shape, the fit uses only the region of the sky away from Cas A, $0^\circ \leq \alpha \leq 340^\circ$,

where diffuse emission dominates.

The primary disadvantage of this method is the requirement for an accurate sky model. The 408 MHz all-sky continuum survey published by Haslam et al. is a suitable available model [51]. For comparison to the two dish system data, the Haslam map is convolved with a Gaussian kernel determined by the beam measurements in Section 3.2, and scaled using an estimated spectral index of $\alpha_{est} = -2.5$.

The results of the sky model fit are shown in Figure 3.23. 41 MHz baseline spectral ripple is again present, suggesting that the ripple is not exclusively an artifact of the beam shape. The amount of signal coupling into the feed is modulated by the standing waves between the feed and the reflector, leading to varying apparent receiver noise referenced to the external sky brightness. Reducing the baseline ripple, through use of a scatterer or other means, may improve the system temperature in some parts of the band.

3.4.2 Limitations

The system temperature measurements suffer from various sources of error. The most prevalent and difficult to characterize is the gain fluctuation in the receiver. The thermal model described in Section 3.3.1 is helpful in suppressing gain fluctuation, but not sufficient. The gain error affects the signal levels used in the measurements directly, and affects the beam measurements described in Section 3.2.

The method of measuring system temperature using the brightness temperature of Cas A in the telescope beam has three main sources of error: gain

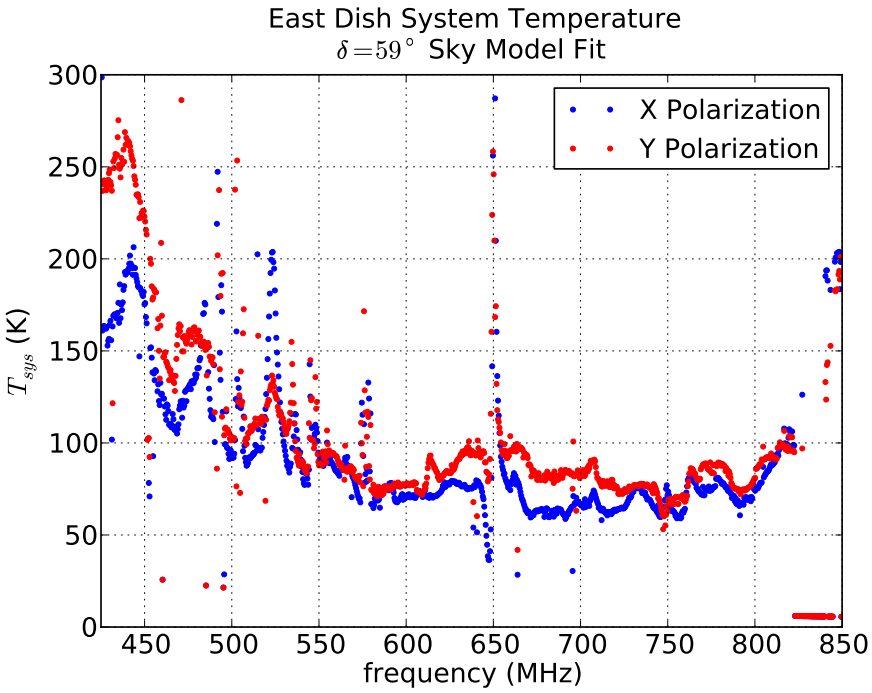

Figure 3.23: The system temperature measured by fitting data collected at $\delta = 59^\circ$ to a sky model derived from the Haslam map.

fluctuation, uncertainty in the measured effective area, and uncertainty in the Cas A flux density. The uncertainty in the effective area results primarily from gain fluctuation and the change in the background sky temperature around Cas A. Telescope pointing uncertainty contributes negligibly in comparison. The 2012 Cas A flux density used to calculate the expected antenna temperature is accurate within 2.4% across the frequency band of interest [45]. This method of measuring system temperature is also packaged with the brightness temperature of the galactic plane around Cas A used as the baseline.

The main sources of error in the system temperature measurement using a sky model are receiver gain fluctuation and the accuracy of the model. The error in effective area is less important in this measurement because the part of the sky measured is dominated by diffuse emission, so the output power is less sensitive to the beam shape. The error in the sky model can be broken into three components: the pointing error of the telescope, the uncertainty in the original sky map used to generate the model, and the uncertainty in the spectral index used to scale the map from 408 MHz. Since the beam full width half maximum is nearly everywhere larger than 3°, the sky is dominated by diffuse emission, and the pointing error is much less than 3°, the contribution of pointing error to the total uncertainty is negligible. The error in the published Haslam map at 408 MHz is less than 10%, with an offset error of less than 3 K [51]. The map is converted into a telescope brightness temperature model by convolving it with a Gaussian beam according to the beam measurements in Section 3.2, and scaling it in frequency with a spectral index of $\alpha_{est} = -2.5$. The excess error introduced into the sky model through the scaling is less than ±14% at 800 MHz if $-2.3 < \alpha < -2.7$ for the true spectral index α, and less than ±8% at 600 MHz. Slow gain variation has a larger effect on the sky model method than the Cas A amplitude method.

A comparison of the system temperatures calculated using the two methods is shown in Figure 3.24. The Cas A amplitude comparison measurement has subtracted the baseline galaxy sky temperature according to the sky model used in the fit.

The day to day variation in measured system temperature provides some

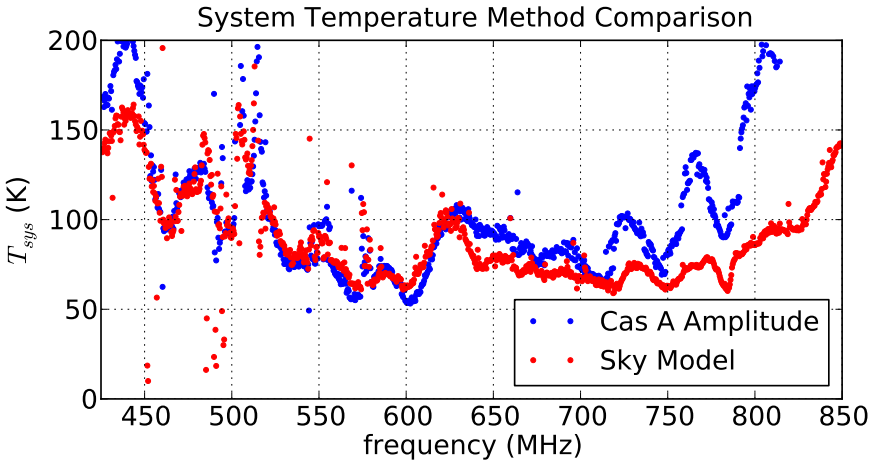

Figure 3.24: The system temperature measured using both the Cas A galaxy comparison and sky model fit. The Cas A galaxy measurement has subtracted the baseline sky temperature according to the sky model. The measurements are based on data from the west dish X polarization.

insight into the error of the measurement. The system temperature was measured for 11 consecutive sidereal days on the west dish. The results for each day are shown in Figure 3.25. The standard deviation at each frequency as a fraction of the median is shown in Figure 3.26.

3.4.3 Noise Budget

In the centre of the frequency band the system temperature is between approximately 60 and 100 K. The expected system temperature can be broken into five components: signal loss in the feed, receiver noise, mismatch between the feed and LNA, antenna spill over, and external signal such as the CMB and atmospheric noise.

At 600 MHz, the total loss in the feed (Table 2.2) accounts for approxi-

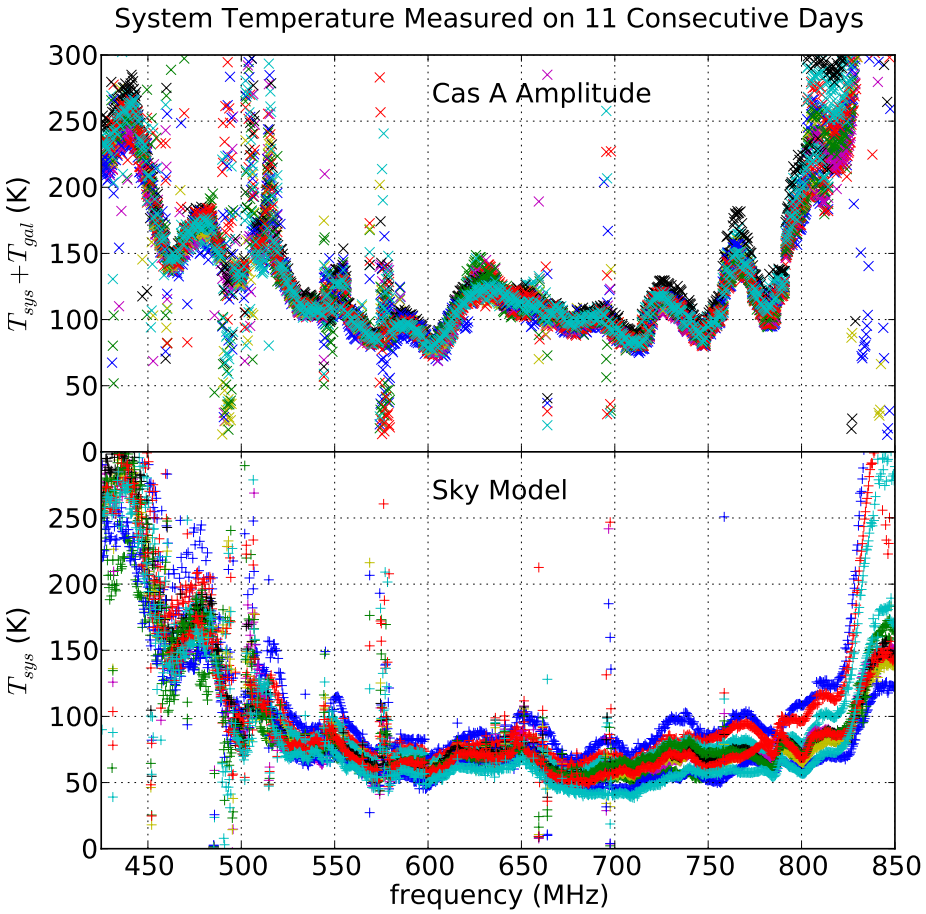

Figure 3.25: Eleven system temperature measurements calculated using the amplitude of Cas A and the sky model fit. Each measurement uses one sidereal day of data collected using the west dish X polarization instrumented with a low loss feed (Section 3.4.4).

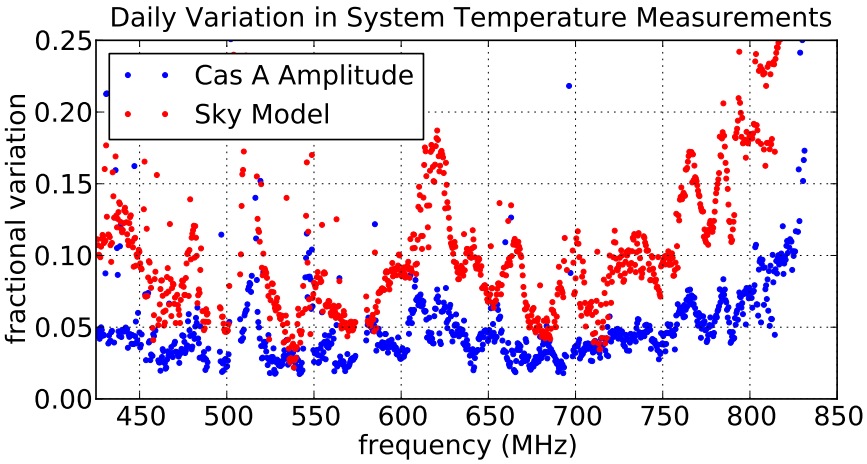

Figure 3.26: The standard deviation as a fraction of the median of eleven daily system temperature measurements calculated using both the amplitude of Cas A and the sky model fit. Each measurement uses one sidereal day of data collected using the west dish X polarization instrumented with a low loss feed (Section 3.4.4).

mately 23 K. The contribution of the feed mismatch to 50 Ω is complicated. Since the LNA noise performance and gain depend on the input impedance it is presented with, the feed mismatch alters the receiver noise from that measured in the lab. To properly calculate the overall noise of the receiver and feed combination, the full noise parameters of the LNA are required. A full noise parameter measurement of the LNA is not available.

Instead, the mismatch is treated by assuming the LNA noise and gain remain constant with input impedance. In this case, the feed mismatch to 50 Ω is used to calculate the amount of reflected input signal power. For a return loss of -12 dB (Figure 2.36), 6.5% of the power is reflected, increasing the apparent receiver noise temperature by about 7%, or 3 K for a receiver

noise temperature of 34 K. The gain of the LNA is sufficient that the later stage amplifiers and ADC contribute less than 1 K midband.

The remaining contributions are external from the receiver: atmospheric noise, the CMB, and spillover. Atmospheric noise in the CHIME band is negligible, and the CMB adds 3 K.

Antenna spill over describes the power received by the feed through the portion of the solid angle of the feed radiation pattern which is not directed at the reflector. This includes the part of the main lobe beyond the edge of the reflector, and the side and back lobes. The dish is 8.53 m in diameter and has a focal length of 3.66 m, so any part of the feed pattern beyond 60° from boresight spills outside reflector.

Ideally, the solid angle of the feed pattern beyond 60° is integrated with the surrounding surface brightness to calculate the exact antenna temperature of the spill over. Practically, it is very difficult to calculate precisely due to the difficulty of establishing the surface brightness seen by the extra-reflector solid angle, and accurately measuring the side and backlobes of the feed on the dish.

A plot of the estimated spillover contribution to the system temperature both with and without the isolating cylinders is shown in Figure 3.27. The calculation convolves the extra-reflector solid angle according to simulated feed radiation patterns with a constant 300 K surface brightness from the horizon to the dish edge, and 0 K above the horizon [52].

The full noise budget at 600 MHz is summarized in Table 3.1. A broadband estimate of the expected noise temperature is shown in Figure 3.28.

Bounding curves indicating the uncertainty are included for the predicted

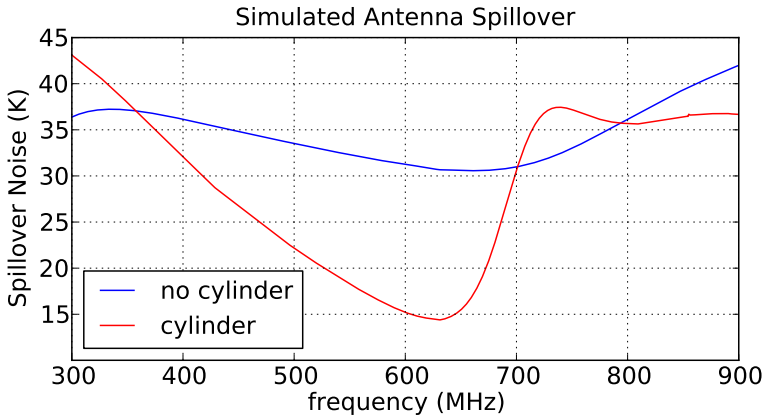

Figure 3.27: The estimated spillover contribution to the system temperature both with and without the isolating cylinders on the ground plane based on simulated feed patterns [52]. The spillover for the full CHIME telescope should be nearly zero because of the low f number of the cylinders.

system temperature based on estimated uncertainty of the individual components. The uncertainty is quantified only in the middle of the band, from approximately 500 to 800 MHz, where the contribution of the later stage amplifiers and feed mismatch uncertainty is negligible. The uncertainty in the LNA noise temperature measurement detailed in Section 2.3.4 makes the largest contribution in the centre of the band. The error in the feed loss is roughly 11% based only on the uncertainty in dielectric constant and loss tangent for FR-4 material at 1 GHz. The spillover uncertainty is difficult to quantify; here, a pessimistic estimate of 50% is used.

At some frequencies the measured noise is considerably higher than anticipated. One candidate for the cause of this discrepancy is the effect of the feed impedance on the performance of the LNA. As shown by Equation 2.16, the noise of a microwave amplifier depends on the impedance

Feed Loss	23 K ± 3 K
Receiver Noise	34 K ± 11 K
Feed Mismatch	3 K ± 1 K
CMB	3 K
Ground Spill	15 K ± 8 K
Total Predicted	**78 K ± 14 K**
Total Measured	**85 K**

Table 3.1: Contributions to the system temperature at 600 MHz.

presented at its input. Since the impedance of the feed varies significantly across the frequency band (Figure 2.35), the amplifier noise may deviate from the measured performance. The 41 MHz baseline ripple also appears to cause significant variation in the system temperature. The effect of baseline ripple is not included in the model used to generate the predicted system temperature. Also, at the band edges where the signal is small, the internal ADC noise contributes to the total noise. At the low edge of the frequency band, the signal includes sub 425 MHz signal that is insufficiently attenuated by the filter, allowing contamination of the aliased samples.

3.4.4 T_{sys} Using Low Loss Feed

The low loss feed described in Section 2.5.4 should reduce the contribution of the feed loss by almost 20 K at 600 MHz. A low loss feed was installed on the west dish, and the system temperature measured by observing at $\delta = 59^{\circ}$ and comparing Cas A to the galactic plane. The resulting system temperature (including the galactic plane brightness) is shown in Figure 3.29 for both polarizations and both feeds. A reduction in system temperature

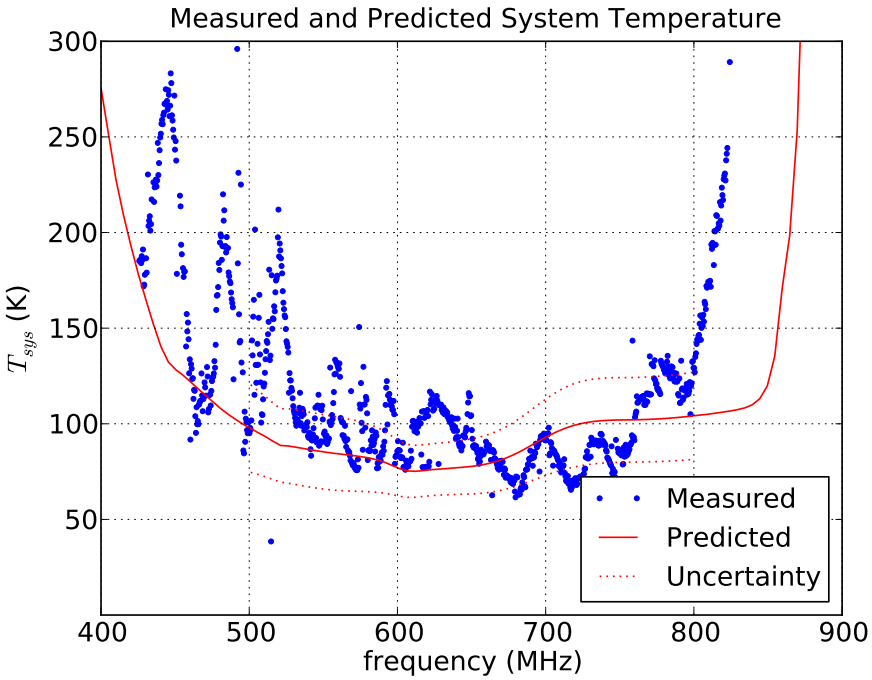

Figure 3.28: The measured and predicted system temperature with the isolating cylinders on the ground plane, not including sky brightness. Bounding uncertainty curves are included for the predicted system temperature midband. The measured system temperature is calculated using the amplitude of Cas A measured on the east dish X polarization, and subtracting the baseline galaxy temperature using a sky model.

is indeed observed across most of the band. The variability with frequency of the observed difference suggests that the change in feed impedance may also impact the measurement.

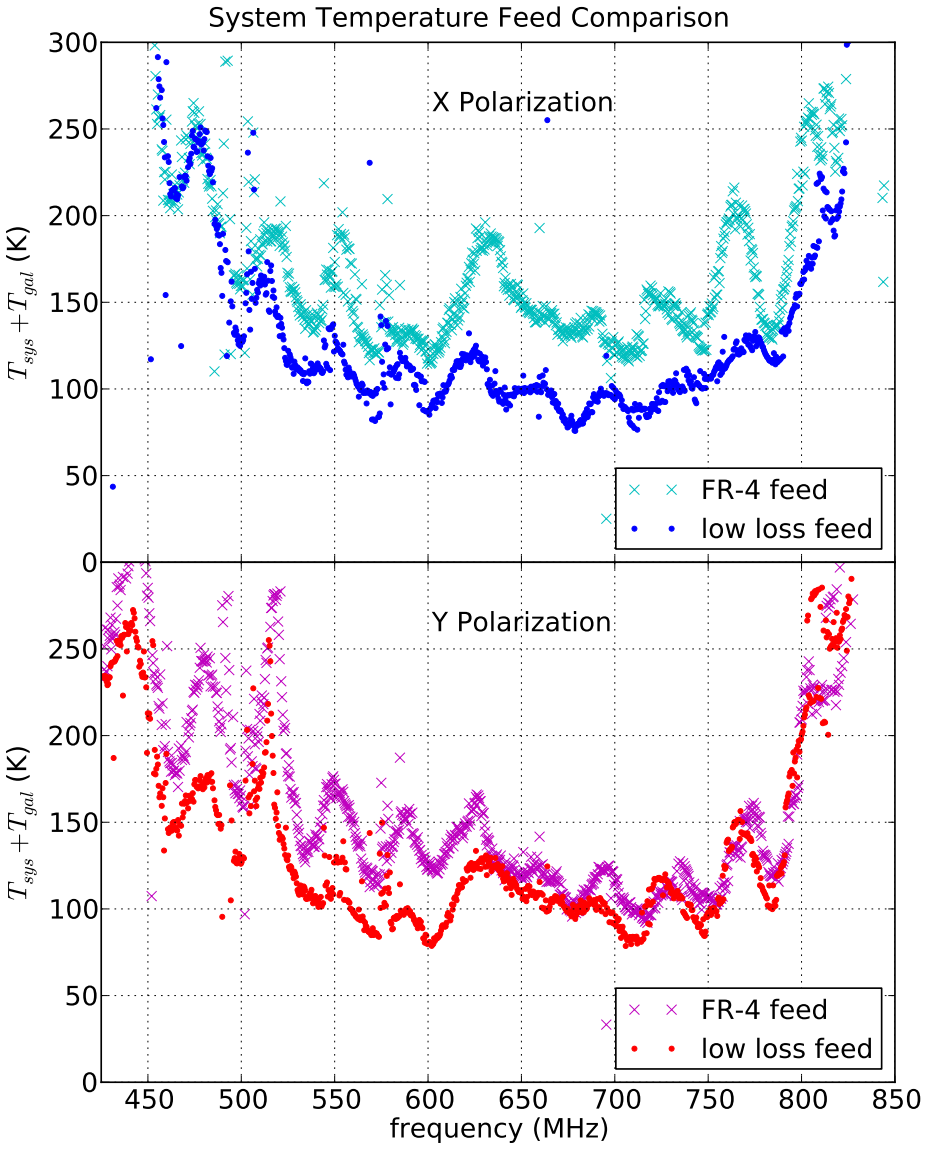

Figure 3.29: The system temperature on the west dish measured using the amplitude of Cas A with the original FR-4 feed and the low loss RO5880 feed. The system temperature includes the baseline galaxy brightness just off of Cas A.

3.5 Radio Frequency Interference

Although DRAO provides a comparatively clean radio frequency environment, some radio frequency interference (RFI) is present in the CHIME frequency band, especially at low frequencies. The sources of RFI include various nearby transmitters and interference generated by operations on site.

Figure 3.30 shows power spectra computed using data collected on the east dish over approximately 39 hours. The power spectra were calculated using snapshots of the raw ADC samples instead of the usual averaged correlator output autocorrelations. During each approximately 1.26 second correlator averaging window, a snapshot of 8192 consecutive raw ADC samples is saved to disk. To compute the power spectra shown in Figure 3.30, each 8192 raw ADC sample snapshot was divided into four 2048 point windows, each of which was Fourier transformed and squared. The mean and maximum per frequency bin of the resulting roughly ∼432,000 individually calculated power spectra are shown.

Assuming that for each frequency bin the power received in a given window follows a Gaussian distribution, the variance σ^2 of each frequency bin can be estimated from the average power spectrum itself. Using this estimate, a 4.8σ fluctuation from the mean is calculated and superimposed. The probability of seeing no 4.8σ fluctuations in 432,000 samples is about 50%. The standard deviation σ may be overestimated, since the data are not strictly Gaussian distributed due to RFI.

Dividing the band between 425 and 850 MHz into 1024 bins, the RFI contamination level of each frequency bin is estimated using the collected

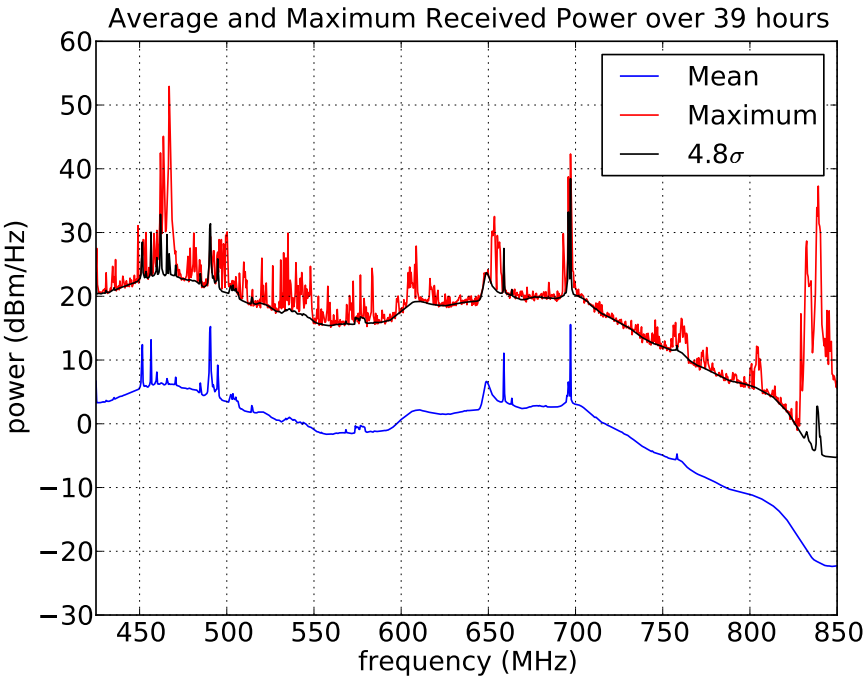

Figure 3.30: The maximum and average received power per frequency bin over a 39 hour (∼432,000 samples) period. The variance of the power spectrum data in each frequency bin is estimated by the average value. The probability of seeing a 4.8σ fluctuation in this time is about 50%.

autocorrelation data. A spike removal algorithm finds how frequently sharp RFI appears in a given frequency bin. By computing the variance in short sections of data and comparing it to the long term mean of the data, bins which grossly disobey the radiometer equation, and thus must be heavily affected by RFI, are found. Using these two methods in conjunction, approximately 12% of the 1024 frequency bins are estimated to be contaminated beyond use. Of these contaminated bins, nearly two thirds are below 550 MHz.

3.5.1 DRAO Local Oscillator and Fire Department Dispatch Transmissions

There are two important sources of RFI whose sources are well understood. The first is the DRAO Synthesis Telescope Local Oscillator at 694 MHz. The second is a local fire department dispatch communications signal which uses four frequencies between 453 and 466 MHz.

DRAO is aware of the local oscillator leakage, and has dedicated significant effort toward improving it, drastically reducing the overall power received by the two dish system at 694 MHz. That frequency remains unusable for data collection, but the reduction increases the dynamic range available in the receiver for other frequencies. The amount of power received from the local oscillator leakage is heavily dependent on the pointing and spacing of the seven element movable Synthesis Telescope dishes.

The fire department dispatch signals are intermittent, bimodal radio over internet transmissions at four frequencies according to Industry Canada[5]: 452.7125, 457.7125, 461.0125 and 466.0125 MHz. The transmissions occur every day intermittently between 8:30 and 9:30 am and 6:30 and 7:30 pm local time, and less frequently at other times throughout the day and night. Based on several weeks of data collected in February and March of 2012, transmissions occur approximately 0.6% of the time. A histogram showing the time spent transmitting in each hour of the day normalized to the total transmitting time is shown in Figure 3.31.

The power received by the two dish system while the fire dispatch trans-

[5] http://www.ic.gc.ca/eic/site/sd-sd.nsf/eng/h_00025.html

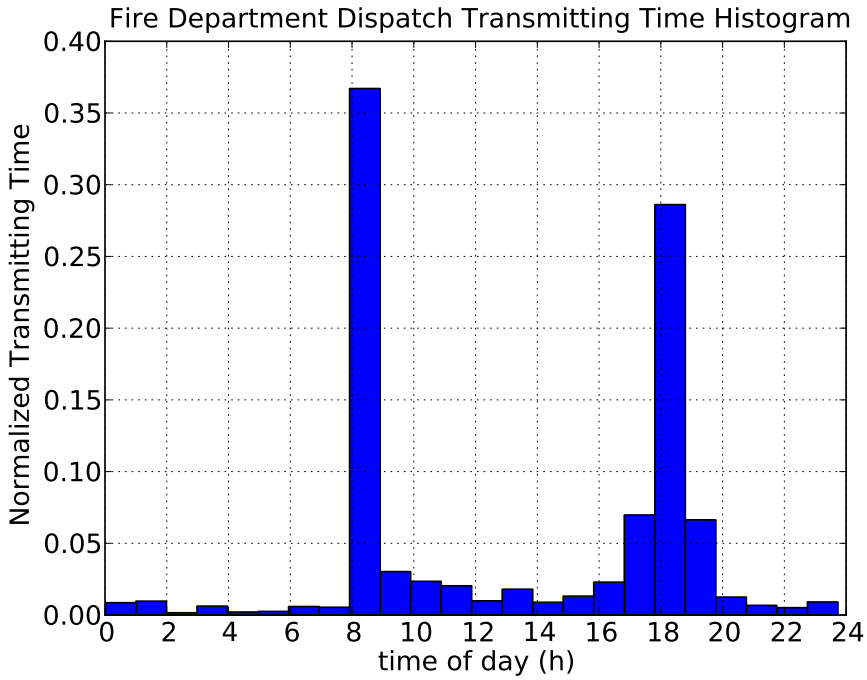

Figure 3.31: Histogram showing the time of day the fire department dispatch interference signal transmits. The y-axis is the time spent transmitting during the given hour, normalized to the total transmitting time.

missions are occurring is so large that it causes non-linear behaviour in the receiver. While the transmitter is broadcasting, the full frequency band is affected, making all data unusable.

3.5.2 Large RFI Causing Non-Linearity

The fire department dispatch signal is one example of a large, narrowband RFI source that affects the full frequency band by driving the receiver into a non-linear region of operation. Other large RFI spikes can have the same effect. In Figure 3.32a, the standard deviation of the voltage at the ADC

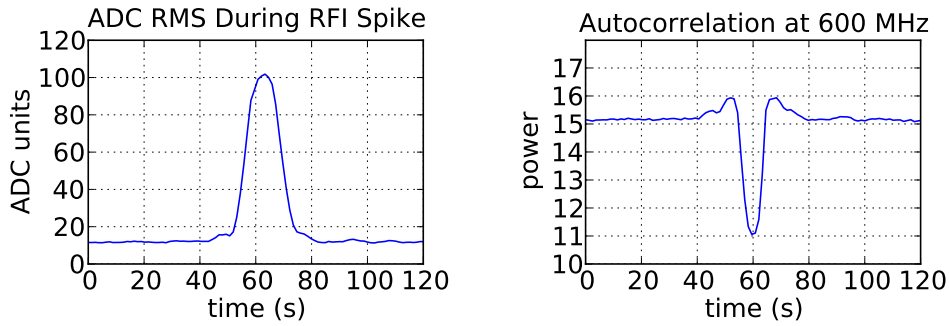

(a) ADC voltage standard deviation

(b) Power in the autocorrelation at 600 MHz

Figure 3.32: The effect on the receiver of a large RFI spike at 467 MHz.

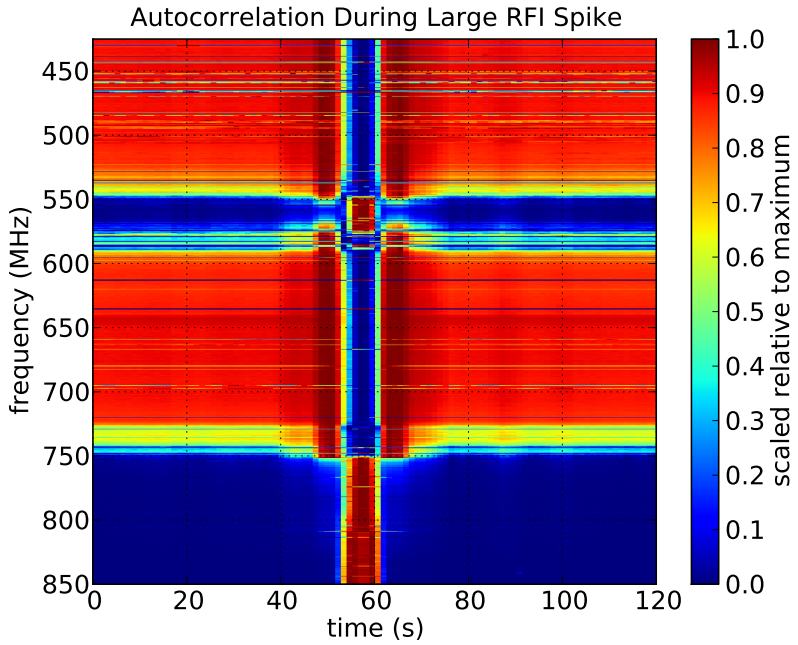

Figure 3.33: The effect on the full frequency band of a large 467 MHz RFI spike is shown. Across most of the band, the inverted Mexican hat shape seen at 600 MHz in Figure 3.32b is seen. At some frequencies, however, the received power uniformly rises and falls with the RFI power.

input is shown over a two minute period during which a large, narrowband RFI spike at approximately 467 MHz comes and goes. Figure 3.32b shows the power measured in the autocorrelation at 600 MHz over the same time.

At 600 MHz, as the RFI power begins to rise shortly after the 40 second mark, the received power at 600 MHz increases. As the RFI power continues to grow, the 600 MHz power falls dramatically, then rises again before returning to the normal level. This inverted Mexican hat shape is a characteristic effect of large RFI seen across much of the frequency band, as shown in Figure 3.33.

The initial rise in power indicates that the RFI is changing the average DC bias point of one or more of the amplifiers in the receiver, which is increasing either the gain, the noise, or both. Eventually, the RFI power increases to a level sufficient to cause traditional gain compression, resulting in the large decrease in received power during the time when the RFI spike is largest around the 60 second mark in Figure 3.32. At some frequencies, particularly at the high end of the band and around 560 MHz, the gain never reaches compression. These frequencies correspond to the places where the receiver has the least gain. This suggests that the compression is occurring in the late stages of the receiver after the signal has been partially amplified.

The initial increase in received power suggests that the receiver is not optimally biased for gain noise. It may be possible to alter the DC bias of the amplifiers such that the slope of the bias curve is 0; ie, bias the amplifier at a local gain maximum. This would reduce the gain fluctuation caused by large RFI. However, changing the bias may adversely affect other areas of receiver performance, most importantly the noise temperature.

The LNA and second stage amplifier immediately before the first filter have a broad frequency response (see Figure 2.18b), and may be susceptible to a similar phenomenon to that shown in Figure 3.32 caused by out of band RFI. The effects of such out of band RFI are more difficult to identify than in band RFI since the primary spike is considerably attenuated by the band defining filter in the receiver. The input power necessary to cause early stage non-linearity is very large.

3.5.3 Other Data Oddities

Various poorly understood unusual features in the autocorrelations appear with some regularity. Three such anomalies are highlighted here.

Small spikes in received power appear in all four channels and in all frequencies synchronously with a period of 60 seconds. The amplitude of the spikes vary by channel and in time. At some times they are below the noise level, and at other times, as in Figure 3.34, they are well above the noise level. The spikes have been present since the two dish system began observing.

Another intermittent but recognizable feature occurs in all channels with a regular period. This feature, resembling a mitten, is shown in Figure 3.35. The power rises from the baseline for about three minutes, then falls back to the baseline level for about a half minute, then rises again for a further half minute, before returning to the baseline level for about one and a half minutes, for a total period of about five and a half minutes. There is also a spike during the first longer high stretch about one minute after the initial rise. The mittens are generally broadband, and occur in all four channels.

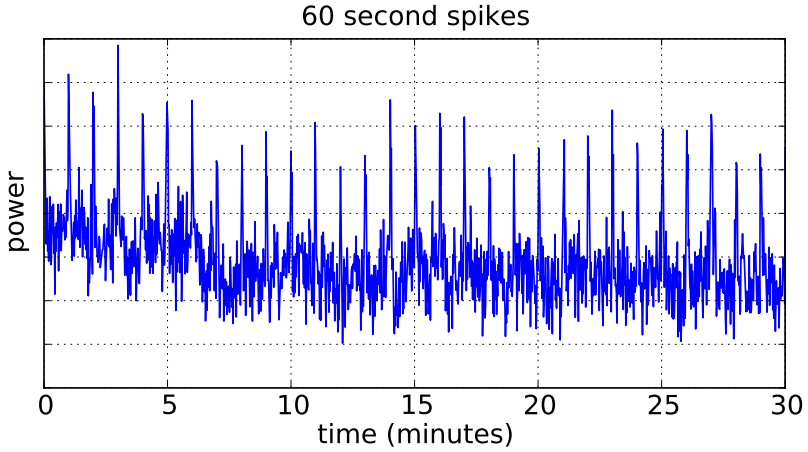

Figure 3.34: Sixty second period spikes shown in an autocorrelation during a time when they are prominent.

A small section of the frequency band over more than an hour is shown in Figure 3.36. The mitten phenomena come and go without an obvious pattern or predictable interval between occurrences, and have been present since the two dish system began observing.

Both the mittens and sixty second spikes appear to be caused by sources external from the instrument. When the feed connection to the LNA is replaced with a resistive termination, the features do not appear.

The third category of data anomaly has a burst noise character. These fast changes in received power come in many forms, some of which appear to be caused by external sources, and others of which are internal to the instrument. All of the burst noise is broadband.

Those that are internal to the instrument appear in only one channel at a time, and the amplitude of the changes and frequency of occurrence

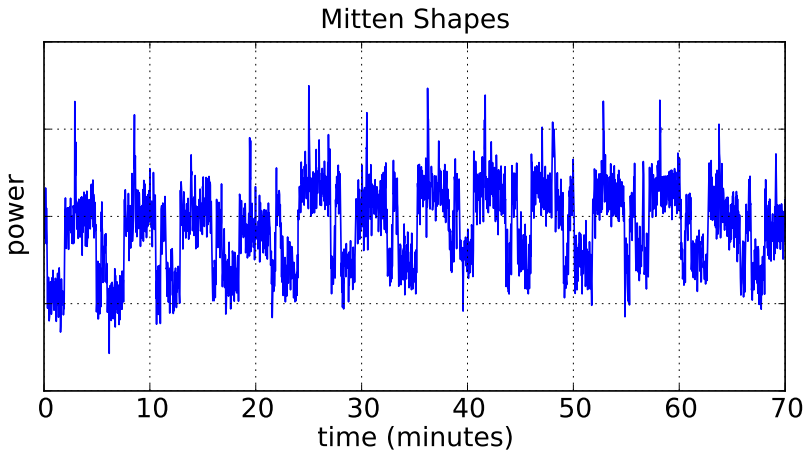

Figure 3.35: Mitten shaped RFI at a single frequency in a single channel.

are highly variable. Tampering with the electronics at the focus and the various cable connections in the receiver often changes the characteristics of the shifts, suggesting a possible mechanical connection issue. The shifts sometimes happen within the approximately 1.25 second duration samples, and other times occur over minutes. The instrumental burst noise is not observed in lab testing with a system using the same receiver and correlator as the two dish system.

Other similar level shifts occur which are common to multiple channels, suggesting an external source. A few typical examples of both external and instrumental level shifts are shown in Figure 3.37.

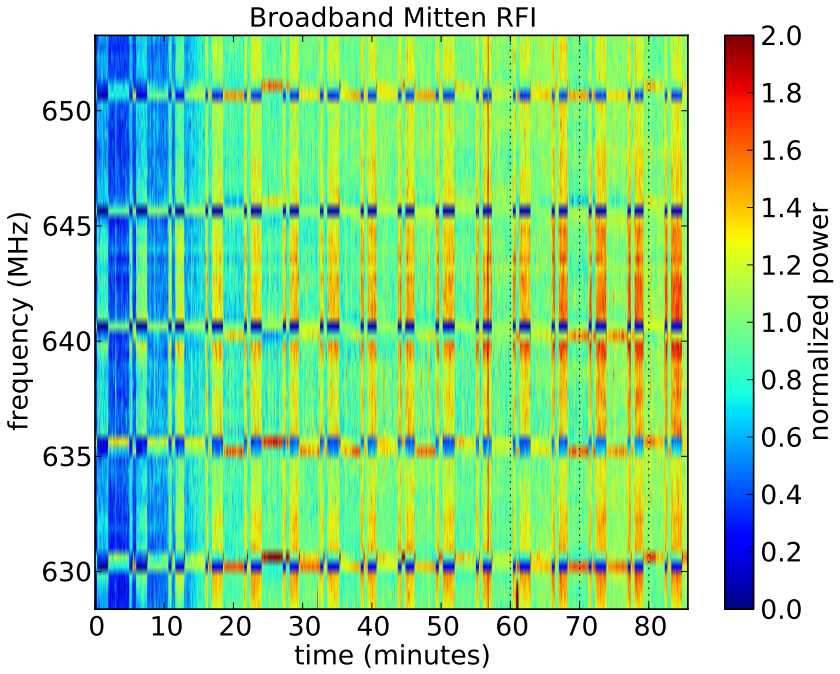

Figure 3.36: Mitten shaped RFI across the middle of the band for a single channel. At each frequency, the minimum power is subtracted and the overall power is scaled by its median.

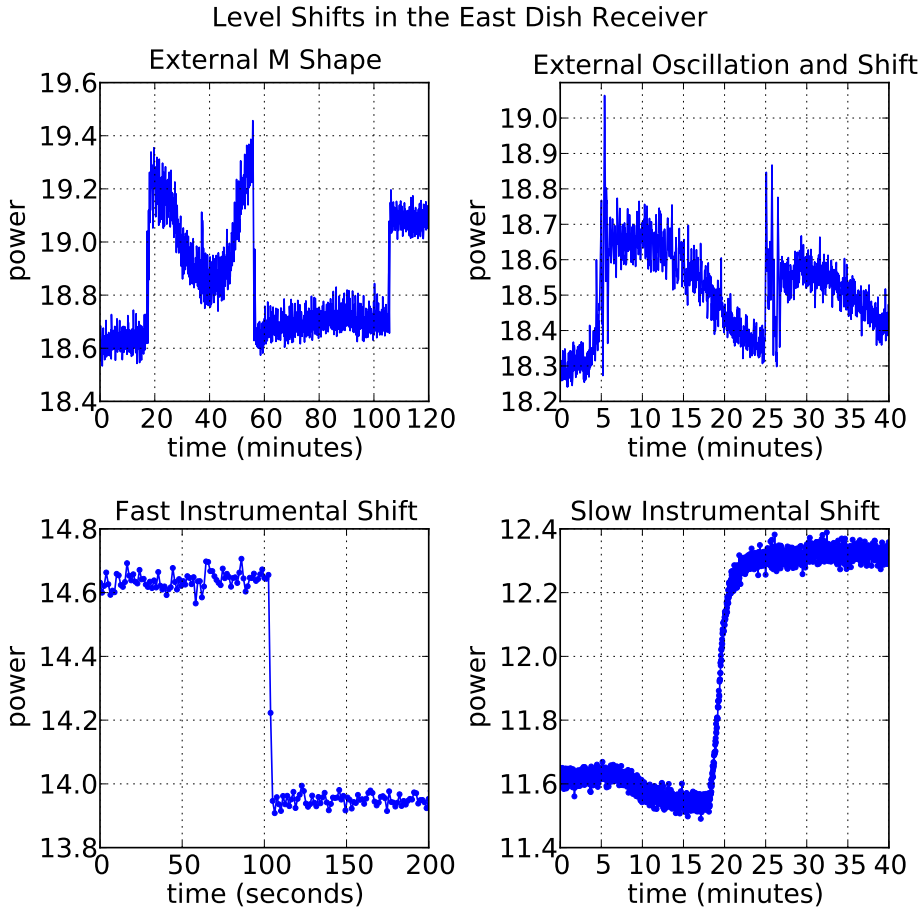

Figure 3.37: Several examples of burst noise. The shapes in the top left and top right are caused by external signals. Both are characteristic shapes seen at irregular intervals. Each incident exhibits similar timing and variable amplitude. The bottom left and bottom right are examples of fast and slow level shifts occurring within the instrument.

Chapter 4

Sky Maps

Data were collected using the east dish X polarization over seven weeks to produce maps of the sky between declinations $52^\circ \leq \delta \leq 73^\circ$. Approximately once per day, the dish was tilted 1° north to a new declination, beginning from $\delta = 52^\circ$ and ending at $\delta = 73^\circ$. The resulting data were binned by right ascension and declination into pixels of equal area using the HEALPix architecture [53]. The maps use HEALPix nside = 64, resulting in 49,152 pixels covering the full sphere of the sky. Of these, approximately 4500 pixels are included in the declination range covered by this mapping experiment.

The mapping data collection took place between February 1st and March 23rd 2012, in two sections. First, the dish was tilted between declinations 52° and 63° over the course of two weeks. For logistical reasons, the dish remained at $\delta = 63^\circ$ for nearly three weeks, before continuing from $\delta = 63^\circ$ to $\delta = 73^\circ$ over another two weeks. A plot of the number of data points collected at each sky pixel location is shown in Figure 4.1. All maps in this chapter use a Mollweide projection in celestial coordinates.

Prior to binning the data into sky pixels, the time series data are filtered for RFI and thermally adjusted using the gain model described in Section 3.3.1. The data points contaminated by RFI are not included in

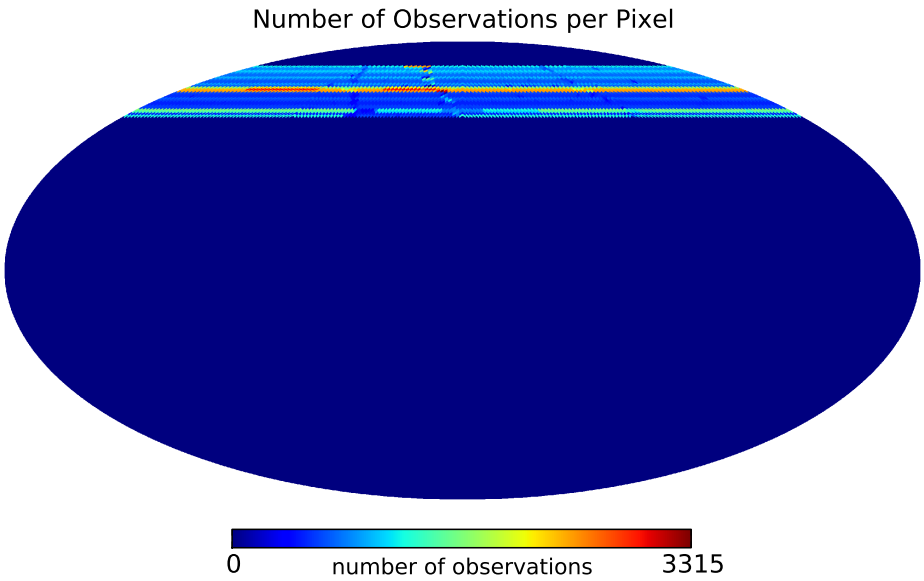

Figure 4.1: The number of raw data points collected at each pixel on the sky.

the maps, so each pixel at each frequency contains a unique number of observations that may differ from Figure 4.1. Some heavily contaminated frequencies include empty pixels within the range of observed declinations.

After binning the data into sky pixels, the maps are converted into units of Kelvin by dividing out the gain in Figure 3.21. The resulting intensity maps represent the total system temperature as a function of the pointing direction of the telescope. The baseline intensity at each frequency is subtracted from the overall map, yielding the sky surface brightness convolved with the telescope beam relative to the minimum; ie, a map of the sky brightness temperature up to an offset. Several examples of such maps at different frequencies across the band are shown in Figure 4.2.

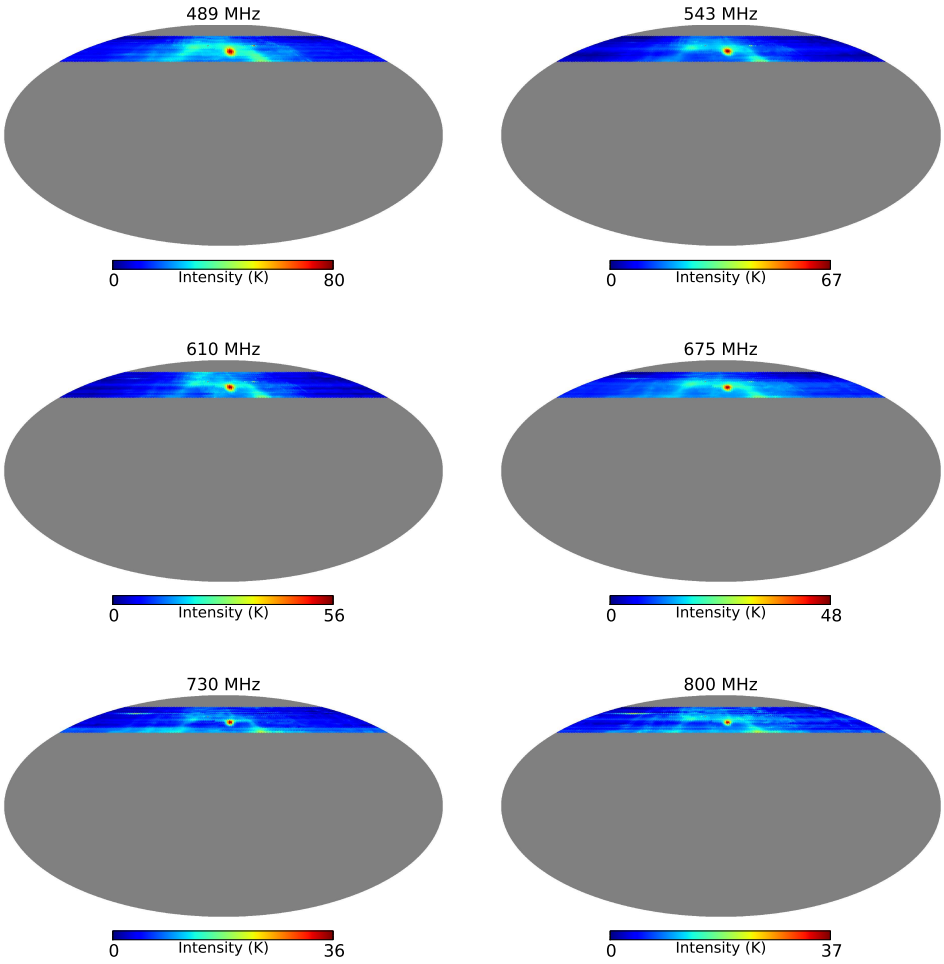

Figure 4.2: Sky maps at 6 of 1024 frequencies across the 425-850 MHz band. The minimum of each map has been subtracted.

The maps suffer from significant variation in the receiver gain and non-sky system temperature, distorting the sky brightness temperature. To demonstrate the effect, the maps at the low end of the frequency band can be compared almost directly to the 408 MHz Haslam all sky map [51]. As seen in Figure 4.3, the shape of the map made using the east dish wanders considerably compared to the scaled Haslam map. Cassiopeia A is dimmer in the current map because its flux density is decreasing with age.

4.1 Principal Component Analysis

One of the primary technical challenges facing CHIME is detecting the small cosmic signal in the midst of much brighter galactic foreground emission. In the CHIME frequency band, synchrotron emission is the dominant source of both galactic and extra-galactic foregrounds. Foreground subtraction is possible because synchrotron emission is spectrally smooth. The BAO in a particular frequency range is uncorrelated with adjacent frequencies, while the brightness temperature of foreground emission is given by a power law in frequency, $T \propto f^{\alpha}$.

Many methods of foreground removal have been proposed for 21 cm experiments [54–56]. One such method employs principal component analysis (PCA) as a tool to re-organize a stack of independent frequency maps into orthogonal modes according to the co-variance between frequencies. Each mode contains a fraction of the total variance of the data set. Since spectrally smooth frequency correlated foreground emission dominates the overall variance of the sky, the foregrounds will be largely contained in the modes

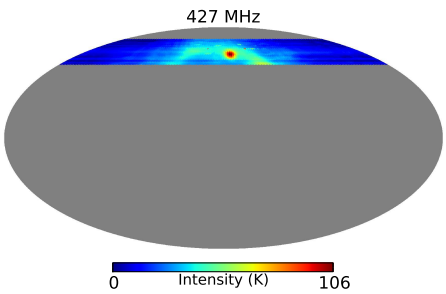

(a) 427 MHz map

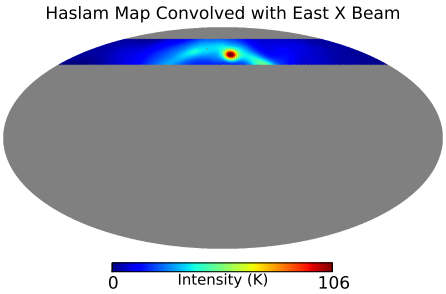

(b) Haslam map

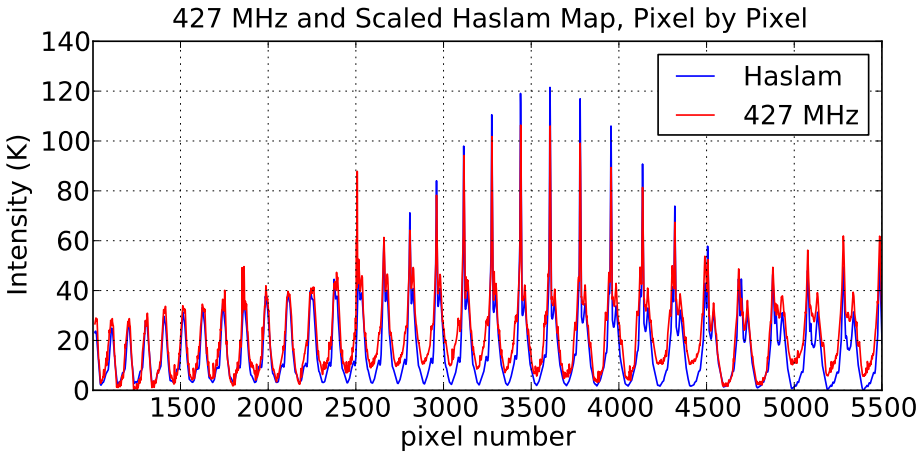

(c) Unravelled pixel by pixel

Figure 4.3: Comparison of a 427 MHz map to the Haslam 408 MHz all sky map convolved with the telescope beam, scaled using a spectral index of -2.5, and shifted to minimum brightness 0. The lower plot shows the maps plotted by pixel number, beginning from the north and moving south along each iso-latitude ring in order of decreasing right ascension.

of highest variance. Frequency maps are reconstructed using the remaining modes, with the foreground emission removed.

PCA consists of decomposing the covariance matrix of the full data set of n pixels by m frequencies into its eigenmodes. The eigenvalues represent the variance contained in the associated mode. Orthogonal maps corresponding to each mode are made by multiplying a matrix of eigenvector rows by the original data. Frequency maps are recovered by selecting which modes to throw away, and multiplying the matrix of remaining eigenvector columns by the matrix of mode maps.

PCA is useful for removing not only foreground emission, but also gain variation. The gain fluctuations in the receiver often have smooth broadband characteristics, so they are largely contained in particular PCA modes.

An analysis of the gain calibrated mapping data was performed using the approximately 700 frequencies that are the least contaminated by RFI. The largest variance mode map, dominated by galactic foregrounds, is shown in Figure 4.4. The eigenvalues are plotted in Figure 4.5. 76% of the total variance of the input map data set is contained in the first mode, 94% in the first 5 modes, 99% in the first 20 modes, and 99.97% in the first 100 modes.

The next several modes after the principal mode contain variance caused recognizably by gain variation. The second mode map shows two distinct halves divided at $\delta = 63^\circ$; this corresponds to the declination at which data collection paused for three weeks. The following few mode maps show features which are apparent in many of the frequency maps as times at which significant gain fluctuations occurred. Several mode maps are shown in Figure 4.6.

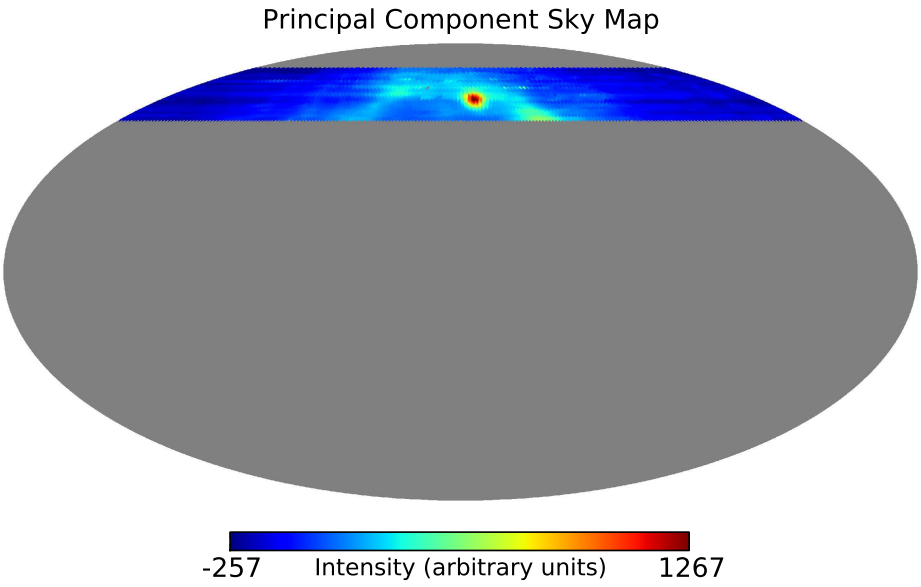

Figure 4.4: The largest variance mode map resulting from PCA on the set of maps at the 700 cleanest RFI frequencies. The galaxy is almost completely contained in the first mode.

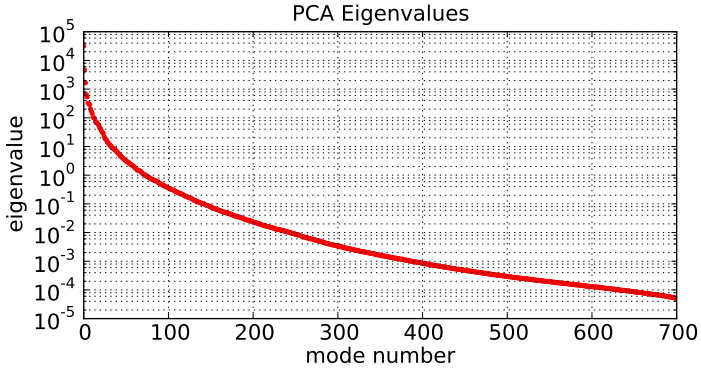

Figure 4.5: The eigenvalues associated with each PCA mode. 76% of the total variance is contained in the first mode, and 99% in the first 20 modes.

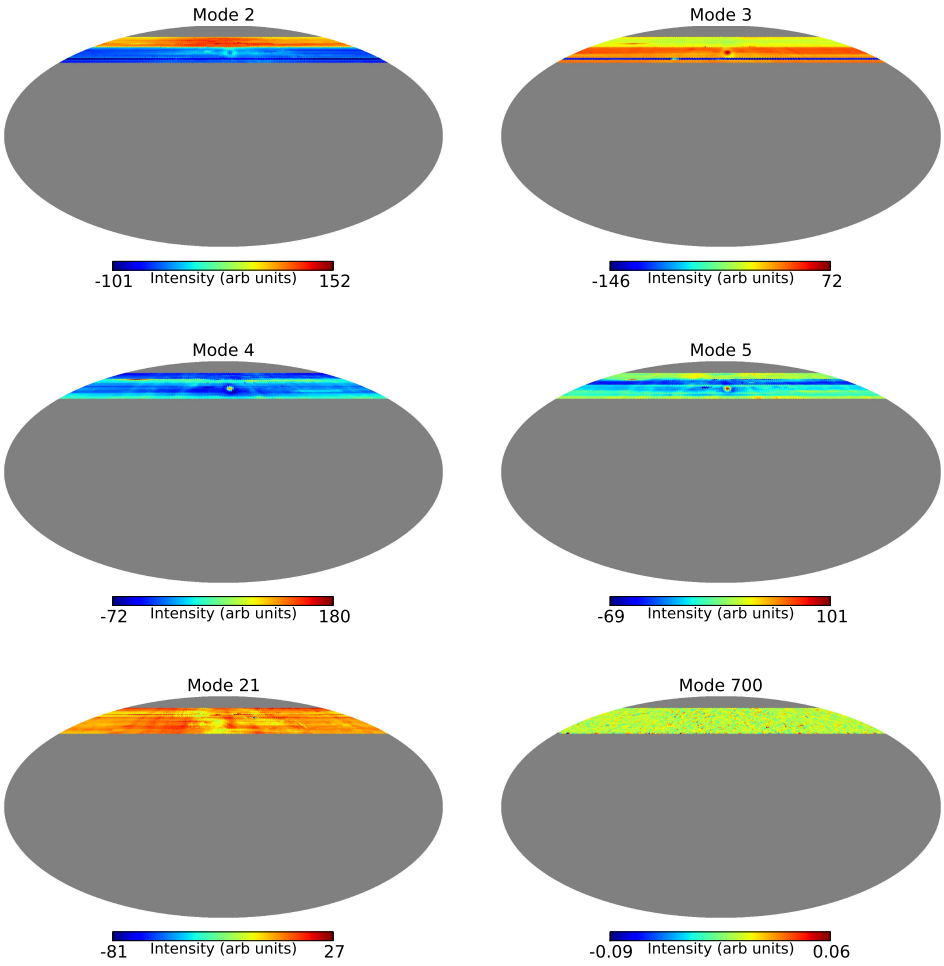

Figure 4.6: PCA mode maps. Some of the high variance modes after the principal mode show features that are recognizable as gain fluctuations in the frequency maps.

4.2 Pulsar Detection

During the mapping, the dish crossed $\delta = 54°$, permitting observation of the pulsar B0329+54 at declination $\delta = 54.5°$ and right ascension $\alpha = 52.5°$. The flux density of B0329+54 is over 100 Jy at 610 MHz, and it has a period of 714.5 ms [57].

To facilitate detection of the pulsar, the number of samples averaged to produce each data point was reduced to ensure a data collection period significantly shorter than the pulsar period. The ROACH correlator program was altered to reduce the averaging from 524,288 to 6400, corresponding to a reduction in the sample period from roughly 1.26 s to 15 ms. The average power spectrum of the autocorrelations between 590 and 675 MHz using 24 minutes of data as the pulsar crossed the beam is shown in Figure 4.7. The measured period is 714 ms.

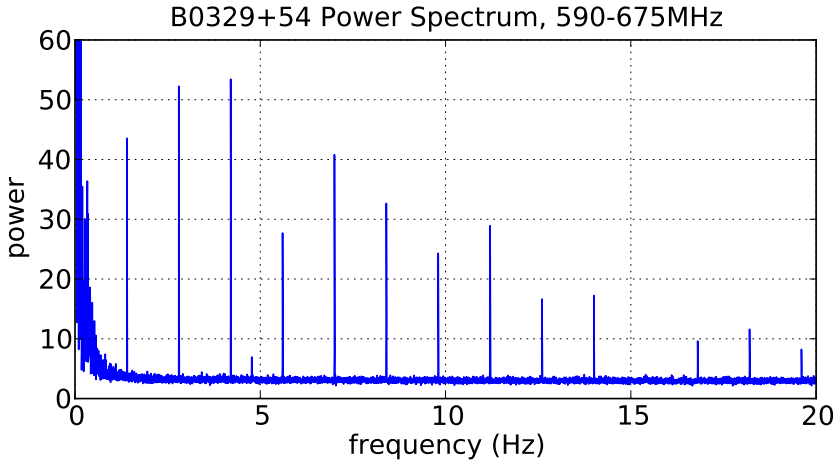

Figure 4.7: The average power spectrum between 590 and 675 MHz of the east dish X polarization while the pulsar B0329+54 is in the beam. The pulsar period is measured as 714 ms.

Chapter 5

Conclusion

A two element interferometer operating between 425 and 850 MHz was built at DRAO as a prototype and technology testbed for CHIME. The system temperature is approximately 80 K midband (not including sky brightness), of which about 40 K is attributable to ground spill and loss in the feed. A commercial band defining filter used in the receiver allows the signal to be alias sampled at 850 MHz and unfolded to 425-850 MHz. A digital correlator based on ROACH hardware acquires and processes the data.

Using the autocorrelations of a single polarization on the east dish, maps of the sky brightness temperature, up to an offset, between declination $52^\circ < \delta < 73^\circ$ across the full frequency band were made. Cassiopeia A was used to calibrate the data and measure the frequency dependent beam shape.

A crude demonstration of foreground removal using principal component analysis showed promising results; nearly all of the the galactic emission and 76% of the overall variance in the maps is contained in the first mode. Receiver gain variation and baseline spectral ripple also partially falls into the high variance modes.

The period of the pulsar B0329+54 was measured as 714 ms, agreeing with the previously published result of 714.5 ms [57].

5.1 Future Work

Crosstalk between the receiver channels originating from leakage at the last stage amplifiers and ADC inputs causes spectral ripple with a period of approximately 3.8 MHz. The spectral ripple is especially prominent in the cross correlations. A shielded room will be installed at the site to reduce the crosstalk and allow the two dish system to be employed as an interferometer as intended. With the last stage electronics inside the shielded room, RF leakage back to the antennas will be substantially reduced.

The second source of spectral baseline ripple, with a period of about 41 MHz, is standing waves between the ground plane and the reflector. Adding a scattering device at the bottom of the reflector in the shadow of the ground plane should reduce the ripple. This should improve the system temperature at many frequencies across the band.

The primary source of uncertainty in all measurements with the two dish system is receiver gain variation. Installing a stable, well known calibration source to inject a chopped white noise signal into the receivers will allow continuous gain calibration. Point sources in the sky such as Cas A can be used for absolute calibration, and the chopped source will provide relative gain measurements.

The analog receiver can be improved in several ways. Most importantly, the LNA should be squeezed to improve the noise temperature as much as possible. A 5-10 K improvement may be easily achievable, especially at the low end of the band. The improvement may come at the expense of the match to 50 Ω. The amplifier and feed could be integrated and designed

as a single unit. The feed baluns could be replaced by a differential LNA topology, reducing loss in the feed.

CHIME collaborators at McGill University have developed an RF over fibre system that could potentially replace the LMR-400 coaxial cables that carry the signal from the focus of each dish to the back end digitizer and correlator. RF over fibre may save cost for full CHIME, and allow easier entry of the signals into the shielded room containing the back end electronics. The system will be tested on the two dish system. The linearity and resulting dynamic range is the crucial performance parameter.

Investigating improved receiver linearity may also prove useful. Some receiver gain fluctuation results from intermittent RFI slightly altering the bias of the amplifiers, thereby changing the gain. Simply reducing the overall gain may also help to alleviate this problem.

Currently, the receiver contains two commercial filters to define the pass band of the system. One may be sufficient, reducing the cost for the full CHIME instrument. Other filters should also be explored. The second stage amplifier circuit should be re-designed more carefully, biased for minimum gain noise with robust stability and linearity as the primary performance goals. Because the power in the last stage amplifier is largest, its linearity is most important.

The two dish system successfully demonstrates many of the technologies required to build CHIME. Most importantly, the receiver is promising and the site is viable.

Bibliography

[1] Adam G. Riess, Alexei V. Filippenko, Peter Challis, Alejandro Clocchiatti, Alan Diercks, Peter M. Garnavich, Ron L. Gilliland, Craig J. Hogan, Saurabh Jha, Robert P. Kirshner, B. Leibundgut, M. M. Phillips, David Reiss, Brian P. Schmidt, Robert A. Schommer, R. Chris Smith, J. Spyromilio, Christopher Stubbs, Nicholas B. Suntzeff, and John Tonry. Observational evidence from supernovae for an accelerating universe and a cosmological constant. *The Astronomical Journal*, 116(3):1009, September 1998.

[2] S. Perlmutter, G. Aldering, G. Goldhaber, R. A. Knop, P. Nugent, P. G. Castro, S. Deustua, S. Fabbro, A. Goobar, D. E. Groom, I. M. Hook, A. G. Kim, M. Y. Kim, J. C. Lee, N. J. Nunes, R. Pain, C. R. Pennypacker, R. Quimby, C. Lidman, R. S. Ellis, M. Irwin, R. G. McMahon, P. Ruiz-Lapuente, N. Walton, B. Schaefer, B. J. Boyle, A. V. Filippenko, T. Matheson, A. S. Fruchter, N. Panagia, H. J. M. Newberg, W. J. Couch, and The Supernova Cosmology Project. Measurements of Ω and Λ from 42 high-redshift supernovae. *The Astrophysical Journal*, 517(2):565, June 1999.

[3] N. Jarosik, C.L. Bennett, J. Dunkley, B. Gold, M.R. Greason, M. Halpern, R.S. Hill, G. Hinshaw, A. Kogut, E. Komatsu, D. Larson, M. Limon, S.S. Meyer, M.R. Nolta, N. Odegard, L. Page, K.M. Smith, D.N. Spergel, G.S. Tucker, J.L. Weiland, E. Wollack, and E.L. Wright. Seven-year Wilkinson Microwave Anisotropy Probe (WMAP) Observations: Sky Maps, Systematic Errors, and Basic Results. *The Astrophysical Journal Supplement Series*, 192:14, 2011.

[4] S. Dodelson. *Modern Cosmology.* Academic Press, 2003.

[5] E.J. Eisenstein. Dark energy and cosmic sound. *New Astronomy Reviews*, 2005.

[6] E. Komatsu, K. M. Smith, J. Dunkley, C. L. Bennett, B. Gold, G. Hinshaw, N. Jarosik, D. Larson, M. R. Nolta, L. Page, D. N. Spergel,

M. Halpern, R. S. Hill, A. Kogut, M. Limon, S. S. Meyer, N. Odegard, G. S. Tucker, J. L. Weiland, E. Wollack, and E. L. Wright. Seven-year Wilkinson Microwave Anisotropy Probe (WMAP) Observations: Cosmological Interpretation. *The Astrophysical Journal Supplement Series*, 192(2):18, 2011.

[7] T. Chang, U. Pen, J.B. Peterson, and P. McDonald. Baryon acoustic oscillations intensity mapping of dark energy. *Physical Review Letters*, 100:091303, 2008.

[8] A. Loeb and J.S.B. Wyithe. Possibility of precise measurement of the cosmological power spectrum with a dedicated survey of 21 cm emission after reionization. *Physical Review Letters*, 100:161301, 2008.

[9] T. Chang, U. Pen, K. Bandura, and J.B. Peterson. An intensity map of hydrogen 21-cm emission at redshift $z \approx 0.8$. *Nature*, 466:463–465, 2010.

[10] U. Pen, L. Staveley-Smith, J.B. Peterson, and T. Chang. First detection of cosmic structure in the 21-cm intensity field. *Monthly Notices of the Royal Astronomical Society: Letters*, 2009.

[11] Y. Mao, M. Tegmark, M. McQuinn, M. Zaldarriaga, and O. Zahn. How accurately can 21-cm tomography constrain cosmology? *Physical Review D*, 78:023529, 2008.

[12] A. Albrecht, G. Bernstein, R. Cahn, W. L. Freedman, J. Hewitt, W. Hu, J. Huth, M. Kamionkowski, E. W. Kolb, L. Knox, J. C. Mather, S. Staggs, and N. B. Suntzeff. Report of the Dark Energy Task Force. *ArXiv Astrophysics e-prints*, 2006.

[13] T.L. Landecker, P.E. Dewdney, T.A. Burgess, A.D. Gray, L.A. Higgs, A.P. Hoffmann, G.J. Hovey, D.R. Karpa, J.D. Lacey, N. Prowse, C.R. Purton, R.S. Roger, A.G. Willis, W. Wyslouzil, D. Routledge, and J.F. Vaneldik. The Synthesis Telescope at the Dominion Radio Astrophysical Observatory. *Astronomy and Astrophysics*, 145(3):509–524, September 2000.

[14] David M. Pozar. *Microwave Engineering*. John Wiley & Sons, Inc., New York, third edition, 2005.

[15] H.T. Friis. Noise figures of radio receivers. *Proceedings of the IRE*, 32(7):419–422, July 1944.

[16] T.H. Lee. *The Design of CMOS Radio-Frequency Integrated Circuits*. Cambridge University Press, 2004.

[17] A.V. Ziel. *Noise in Solid State Devices and Circuits*. Wiley, 1986.

[18] J.W. Haslett and F.N. Trofimenkoff. Thermal noise in field-effect devices. *Proceedings of the IEE*, 116(11):1863–1868, November 1969.

[19] L. Belostotski. *Wide-band CMOS low noise amplifier for the Square Kilometer Array radio telescope*. PhD thesis, University of Calgary, Canada, 2007.

[20] A.S. Roy and C.C. Enz. Compact modeling of thermal noise in the MOS transistor. *IEEE Transactions on Electron Devices*, 52(4):611–614, April 2005.

[21] B. Razavi. *Design of Analog CMOS Integrated Circuits*. McGraw-Hill, 2002.

[22] D. Johns and K.W. Martin. *Analog Integrated Circuit Design*. John Wiley & Sons, 1997.

[23] H.A. Haus, W.R. Atkinson, W.B. Davenport, Jr. G.M. Branch, W.H. Fonger, W.A. Harris, S.W. Harrison, W.W. McLeod, E.K. Stodola, and T.E. Talpey. Representation of noise in linear two-ports. *Proceedings of the Institution of Radio Engineers*, 48(1):66–74, January 1960.

[24] Guillermo Gonzalez. *Microwave Transistor Amplifiers*. Prentice-Hall, Upper Saddle River, NJ, second edition, 1997.

[25] Alain Cappy. Noise modeling and measurement techniques [HEMTs]. *IEEE Transactions on Microwave Theory and Techniques*, 36(1):1–10, January 1988.

[26] H. Statz, H.A. Haus, and R.A. Pucel. Noise characteristics of gallium arsenide field-effect transistors. *IEEE Transactions on Electron Devices*, 21(9):549–562, September 1974.

[27] Sander Weinreb. Low-noise cooled GASFET amplifiers. *IEEE Transactions on Microwave Theory and Techniques*, 33(10):1041–1054, October 1980.

[28] Tom M. Brookes. The noise properties of high electron mobility transistors. *IEEE Transactions on Electron Devices*, 33(1):52–57, January 1986.

[29] J. Rollett. Stability and power-gain invariants of linear twoports. *IRE Transactions on Circuit Theory*, 9(1):29–32, March 1962.

[30] M.L. Edwards and J.H. Sinksy. A new criterion for linear 2-port stability using a single geometrically derived parameter. *IEEE Transactions on Microwave Theory and Techniques*, 40(12):2303–2311, December 1992.

[31] Using the ATF-10236 in low noise amplifier applications in the UHF through 1.7 GHz frequency range. Application Note 1076 5966-0166E, Hewlett-Packard.

[32] Dale D. Henkes. LNA design uses series feedback to achieve simultaneous low input VSWR and low noise. *Applied Microwave & Wireless*, pages 26–32, October 1998.

[33] P.J. Fish. *Electronic Noise and Low Noise Design*. McGraw-Hill, 1994.

[34] A low noise high intercept point amplifier for 900 MHz applications using ATF-54143 PHEMT. Application Note 1299 5988-6670EN, Avago Technologies, July 2010.

[35] A 100 MHz to 500 MHz low noise feedback amplifier using ATF-54143. Application Note 5057 5989-0852EN, Avago Technologies, May 2010.

[36] Roland H. Haitz and Fred W. Voltmer. Noise studies in uniform avalanche diodes. *Applied Physics Letters*, 9(10):381–383, November 1966.

[37] D.R. Chambers. A noise source for noise figure measurements. *Hewlett-Packard Journal*, 34(4):26–27, April 1983.

[38] Fundamentals of RF and microwave noise figure measurements. Application Note 57-1 5952-8255E, Agilent, August 2010.

[39] Noise figure measurement accuracy — the Y-factor method. Application Note 57-2 5952-3706E, Agilent, October 2009.

[40] Duncan Boyd. Calculate the uncertainty of NF measurements. *Microwaves & RF*, pages 93–102, October 1999.

[41] M. Leung. *A Wideband Feed for a Cylindrical Radio Telescope*. PhD thesis, University of Sydney, Australia, 2008.

[42] B.Y. Mills. The Molonglo Observatory Synthesis Telescope. *Proceedings of the Astronomical Society of Australia*, 4(2):156–159, 1981.

[43] A.R. Djordjevic, R.M. Biljie, V.D. Likar-Smiljanic, and T.K. Sarkar. Wideband frequency-domain characterization of FR-4 and time-domain causality. *IEEE Transactions on Electromagnetic Compatibility*, 43(4):662–667, 2001.

[44] A.R. Thompson, J.M. Moran, and G.W. Swenson. *Interferometry and Synthesis in Radio Astronomy*. Wiley, 2001.

[45] J.W.W. Baars, R. Genzel, I.I.K. Pauliny-Toth, and A. Witzel. The absolute spectrum of Cas A; an accurate flux density scale and a set of secondary calibrators. *AAPS*, 61, 1977.

[46] D.R. Williams and B.M. Thomas. The use of a surface polarizer on the parkes telescope to reduce spectral baseline ripple. *Proceedings of the Astronomical Society of Australia*, 4:33, 1980.

[47] D.R. Williams. A harmonic analysis solution to the parkes spectrometer baseline ripple. *Proceedings of the Astronomical Society of Australia*, 4, 1981.

[48] D. Morris. Chromatism in radio telescopes due to blocking and feed scattering. *Astronomy and Astrophysics*, 67:221–228, 1978.

[49] D.G. Barnes, F.H. Briggs, and M.R. Calabretta. Postcorrelation ripple removal and radio frequency interference rejection for Parkes Telescope survey data. *Radio Science*, 40:RS5S13, May 2005.

[50] R.E. Anholt and S.E. Swirhun. Experimental investigation of the temperature dependence of GaAs FET equivalent circuits. *IEEE Transactions on Electron Devices*, 39(9), 1992.

[51] C.G.T. Haslam, C.J. Salter, H. Stoffel, and W.E. Wilson. A 408 MHz all-sky continuum survey. II - The atlas of contour maps. *AAPS*, 47, 1982.

[52] Ivan Padilla. Personal communication, 2012.

[53] K.M. Górski, E. Hivon, A.J. Banday, B.D. Wandelt, F.K. Hansen, M. Reinecke, and M. Bartelmann. HEALPix: A framework for high-resolution discretization and fast analysis of data distributed on the sphere. *The Astrophysical Journal*, 622:759–771, 2005.

[54] S.R. Furlanetto, S.P. Oh, and F.H. Briggs. Cosmology at low frequencies: the 21-cm transistion and the high-redshift universe. *Physics Reports*, 2006.

[55] A. Liu, M. Tegmark, J. Bowman, J. Hewitt, and M. Zaldarriaga. An improved method for 21-cm foreground removal. *Monthly Notices of the Royal Astronomical Society*, 2009.

[56] A. Liu and M. Tegmark. A method for 21 cm power spectrum estimation in the presence of foregrounds. *Physical Review D*, 83:103006, May 2011.

[57] D. M. Gould and A. G. Lyne. Multifrequency polarimetry of 300 radio pulsars. *Monthly Notices of the Royal Astronomical Society*, 301(1):235–260, 1998.